

Phase behaviour of colloidal molecules with anisotropic interactions

Cover: the simulated gas phase of a mixture of the different particles we studied in this thesis namely, spheres, dumbbells, Mickey Mouse particles, tetramers, icosahedra. The colour code refers to the orientation of one particle axis.

PhD thesis, Utrecht University, the Netherlands, March 2017.

ISBN: 978-90-393-6741-4

Printed by Gildeprint.

A digital version of this thesis is available at <https://colloid.nl/publications/theses/>

Phase behaviour of colloidal molecules with anisotropic interactions

Fasegedrag van colloïdale moleculen met een anisotrope interactie

(met een samenvatting in het Nederlands)

Proefschrift

ter verkrijging van de graad van doctor aan de Universiteit Utrecht op gezag van de rector magnificus, prof. dr. G. J. van der Zwaan, ingevolge het besluit van het college voor promoties in het openbaar te verdedigen op maandag 21 maart 2017 des middags te 2.30 uur

door

Guido Avvisati

geboren op 28 oktober 1987 te Avellino, Italië

Promotor: Prof. dr. ir. M. Dijkstra

This work is part of the research programme of the Foundation for Fundamental Research on Matter (FOM), which is part of the Netherlands Organisation for Scientific Research (NWO).

Contents

1	Introduction	1
1.1	Soft matter, colloidal suspensions and self-assembly	2
1.2	Thermodynamics, geometry and energy	5
1.2.1	Hard particles	5
1.2.2	Interacting particles	6
1.2.3	Patchy particles	7
1.3	Computational techniques	9
1.3.1	Monte Carlo simulations	9
1.3.2	Free-energy calculations	11
1.3.3	Common tangent construction for binary mixtures	12
1.4	Scope of this thesis	13
I	Particles with anisotropic shape and interactions	15
2	Self-assembly of patchy colloidal dumbbells	17
2.1	Introduction	18
2.2	Model and methods	19
2.2.1	Geometry and interaction potential	19
2.2.2	Monte Carlo simulations	20
2.2.3	Structure classification via cluster analysis and order parameters	21
2.3	Results	26
2.4	Conclusions	32
3	Self-assembly of “Mickey Mouse” shaped colloids into tube-like structures	35
3.1	Introduction	36
3.2	Model and methods	37
3.3	Results and discussion	38
3.3.1	Self-assembly of clusters and tubes	38
3.3.2	Tube morphology	42
3.4	Comparison with experiments	43
3.4.1	Self-assembly behaviour	45
3.4.2	Cluster structure and free particle concentration	49
3.5	Conclusions	51

4	Phase separation and self-assembly in a fluid of “Mickey Mouse” particles	53
4.1	Introduction	54
4.2	Model and methods	55
4.2.1	Geometry and pair interaction	55
4.2.2	Simulation methods	57
4.3	Results	59
4.3.1	Shift of the binodal line with the particle shape	59
4.3.2	Interaction range-driven transition to self-assembly	62
4.4	Conclusions	67
II	Anisotropic particles with excluded-volume interactions	69
5	Fabrication of colloidal Laves phases for photonic crystals via hard tetramers and hard spheres: bulk phase diagram and stacking diagram for sedimentation	71
5.1	Introduction	72
5.2	Model and methods	73
5.2.1	Monte Carlo simulations	73
5.2.2	Crystalline structures	74
5.2.3	Free-energy calculations	76
5.2.4	Stacking sequences and stacking diagram	77
5.3	Bulk phase behaviour	79
5.3.1	Equations of state	79
5.3.2	Stability of LP1 and phase diagrams	80
5.4	Sedimentation behaviour and stacking diagram	84
5.5	Conclusions	86
6	Phase behaviour of a binary mixture of colloidal spheres and icosahedral clusters	89
6.1	Introduction	90
6.2	Model and methods	91
6.2.1	Monte Carlo simulations	91
6.2.2	Crystalline structures	92
6.2.3	Free-energy calculations	93
6.3	Bulk phase behaviour	95
6.3.1	EOS of pure hard icosahedra, $x=0$	95
6.3.2	EOS of the equimolar mixture of hard icosahedra and hard spheres, $x=0.5$	97
6.3.3	EOS of pure hard spheres, $x=1$	99
6.3.4	Bulk phase diagram	99
6.4	Conclusions	99
	References	103
	Summary	118
	Samenvatting	121

Acknowledgements	123
List of Publications	126
Oral and Poster Presentations	127
About the author	128

1

Introduction

In this chapter we lay out at a general level the subject, the questions, the ideas and the motivation behind this thesis. We introduce terms like “soft matter”, “colloidal suspensions”, “self-assembly”, and discuss how they are related to words like “mayonnaise”, “blood”, and “gems”. After a brief historical introduction, we explain what is interesting about colloids and why and how we can use them to form ordered structures. We then discuss in more detail the role of the anisotropy in the particle shape and the interparticle interaction on these structures.

1.1 Soft matter, colloidal suspensions and self-assembly

The word *soft matter* has recently come to identify a field of research where physics, chemistry and biology meet and address – from different perspectives – questions related to polymers, colloidal particles, surfactants and liquid crystals. Being a field with such diversity, it is challenging to give an “operational” definition of soft matter. Pierre-Gilles de Gennes [1], regarded as the father of this particular field of science, spoke about *complexity* and *flexibility* as main features of soft matter: complex because every single building block in soft matter is already the combination of several thousands of atoms, flexible because the soft matter systems can be transformed by weak external forces.

Many of us remember playing as a kid with clay, that can be moulded by pressing it with our fingers, and for this reason belongs to the soft matter area. Butter and jam are also good examples, since they are somewhat solid but nevertheless can be easily smeared with a knife. The list continues with ketchup, mayonnaise, and whipped cream, toothpaste and shaving cream, paints and nail polish. It is impressive to realise how many of these soft matter systems are present in our everyday life. However, reading through the long list of things we use everyday which fall under the realm of soft matter still does not help grasping what soft matter really is. What are the links among these apparently different systems? It turns out there are two main features shared among all of them:

- **Length scales in between atomic and macroscopic sizes.** Soft matter length scales range in between tens of nanometres for polymer chains, up to a maximum of 1 micrometer for colloidal particles. To put this in perspective, the diameter of a human hair ($\sim 80\mu\text{m}$) is ten thousand to a hundred times bigger than the typical building blocks used in soft matter. For a synopsis of the relevant length scales as compared to more familiar ones, we refer to Fig. 1.1.

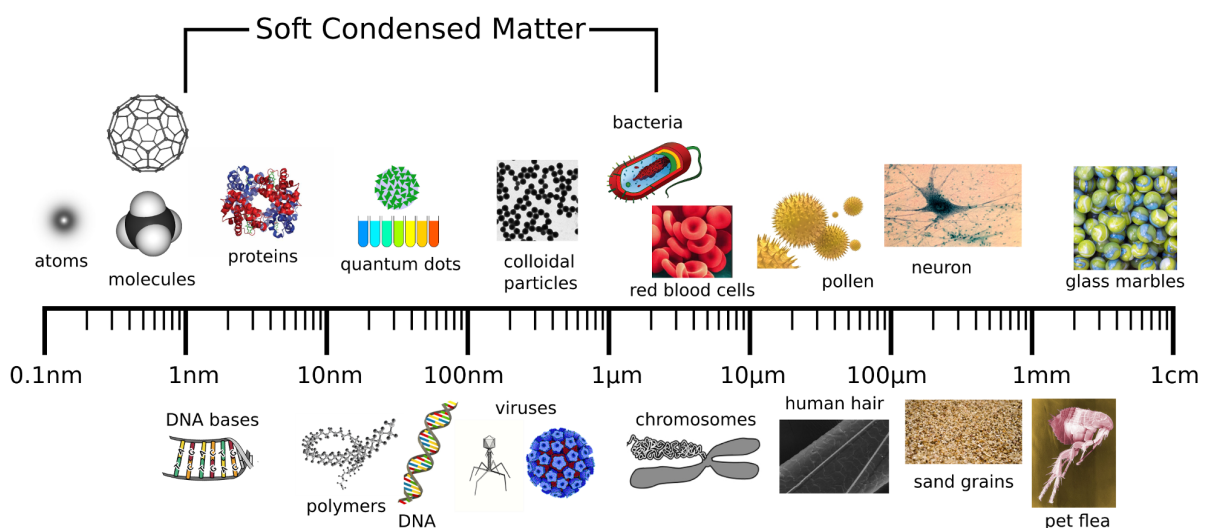


Figure 1.1: Graphical comparison of the soft matter length scales with atomic and macroscopic ones.

- **Brownian motion driven by temperature fluctuations.** The building blocks of a soft matter system undergo a continuous random motion due to the kicks they receive from the molecules of the surrounding medium in which they are immersed.

Together with these two, there is another important characteristic of soft matter systems, which is their ability to spontaneously form ordered structures, also known as **self-assembly**. These three features are intertwined so that none of them accounts, on its own, for the marvellous phase behaviour seen in soft matter systems.

In this thesis we investigate the phase behaviour and the self-assembly of colloidal suspensions. Thus, in this context we expand our discussion on the features of soft matter. By colloidal suspension we mean a system of (insoluble) particles, with a diameter between 1nm and $1\mu\text{m}$, dispersed in a continuous phase [2]. It is also common to refer to the particles themselves as “colloids”. The two phases – dispersed and continuous – of a colloidal suspension can be either gas, liquid or solid. If the dispersed phase is a gas and the continuous phase is a liquid, the suspension is called a foam, like shaving cream and whipped cream. If dispersed and continuous phase are both liquid, we call it an emulsion, like mayonnaise and milk. Finally, if the dispersed phase is solid and the continuous phase is liquid, the suspension is named a sol. The blood flowing in our body is a good example of a sol.

The term *colloid* was introduced by the Scottish chemist Thomas Graham during his studies on diffusion through membranes in 1861 [3]. He found a sticky substance, accumulated at the membranes, which he named after the ancient Greek word for glue $\kappa\acute{o}\lambda\lambda\alpha$. Somewhat earlier than Graham’s experiments, precisely in 1827, the botanist Robert Brown was studying the behaviour of pollen dispersed in water [4]. Via an optical microscope, he observed that minute particles ejected from the pollen grains – now known as amyoplasts and spherosomes – were moving chaotically. At the time he could probably not imagine the importance of his discovery. Nevertheless, this erratic motion was named “Brownian motion” after its discoverer, and it is one of the milestones in establishing the atomic structure of matter. The theoretical explanation of Brown’s observations came, however, almost 80 years later, by Albert Einstein in 1905 [5] and William Sutherland in 1904 [6]. With the hypothesis that the grains experienced random kicks by the much smaller solvent molecules, they derived an expression for the mean square displacement of spherical particles dispersed in a liquid. A few years later Jean Perrin proved this expression by measuring Avogadro’s number via the mean square displacement of colloidal particles observed with optical microscopy, among other ways. His experimental findings settled the question of whether matter is made of atoms and molecules – a question which dates to the Greek Democritus (~ 400 BC) and Roman Lucretius (~ 60 BC) [7–9] – and for this he received a Nobel prize in Physics in 1926.

There is one profound consequence of the constant Brownian motion that colloidal particles experience due to the solvent molecules, which is the system ability of reaching thermal equilibrium states. This means that we can apply the formalism of statistical mechanics, developed and refined, among others, by Boltzmann, Gibbs, and Planck in the second half of the 19th century, to understand the phase behaviour of colloidal suspensions. Isolated colloids move through the solvent and enjoy the entropy available to them. When more and more particles are added to the suspension, eventually they also start to energetically interact – either repel or attract – with each other. This gives rise to collective behaviour, and ultimately leads, under the proper thermodynamic conditions (density, temperature), to the formation of liquid-like states and solid-like ordered structures, as well as glassy states, plastic and liquid crystal, i.e. the

colloidal particles self-assemble. The most prominent example of such a behaviour, predicted by Kirkwood [10], observed in computer simulations [11–13], and later confirmed by experimental work [14], is the formation of a face-centered-cubic crystal from colloidal particles which behave as hard spheres.

Why are colloids so interesting? We have seen that they display a peculiar phase behaviour which is somewhat similar to the one observed in atomic and molecular systems, i.e. the formation of different phases of matter. However, the length and the time scales at which these phenomena happen are much larger than the ones involved in atomic systems. For this reason colloidal suspensions are the perfect playground to investigate condensed matter problems, like phase transitions, crystallisation kinetics, structural defects and quasicrystals, at the single particle level [15–17]. In other words colloids serve as model systems for several outstanding physics topics.

What can we do with colloids? By exploiting their self-assembly, colloids can be employed to make useful structures like, for instance, photonic crystals. A photonic crystal is a structure with periodically varying dielectric constant (refractive index), where the spatial modulation is of the order of the wavelength of the visible light (400-700 *nm*). A colloidal photonic crystal therefore allows one to interact and control light in the visible range, leading to all sorts of applications, including optical fibres, displays and switches, (bio-)sensing and bio-medical engineering, and finally energy storage and security [18–29]. A classic example of a macroscopic photonic crystal is the precious opal, the gem with the beautiful iridescences which are due to the interaction of light with the particular substrate of the gem [30]. Nature also provides us with several examples of photonic crystals, such as the ones found in the wings of some butterflies and scales of beetles, and in some birds' feathers [31–35].

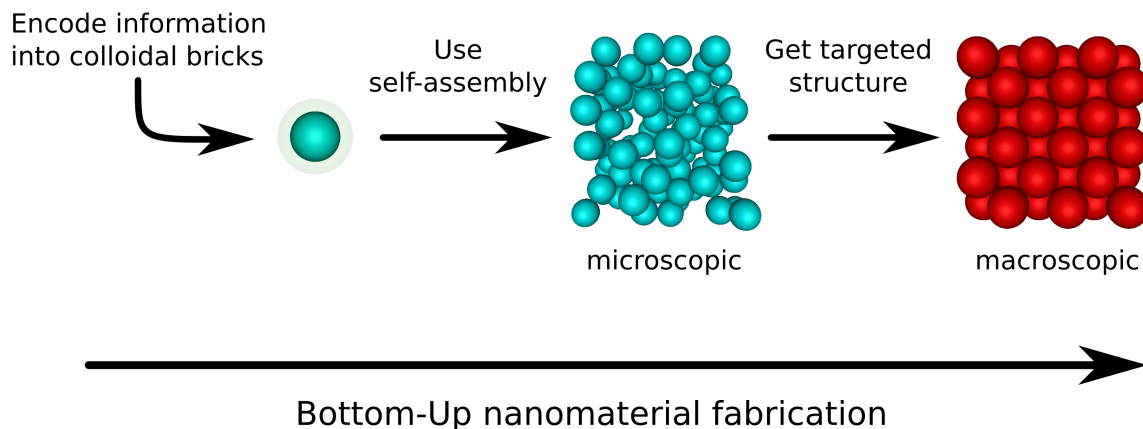


Figure 1.2: Illustration of the colloidal LEGO paradigm. Note that the information to be encoded is in general unknown beforehand.

In more general terms, colloids provide a mean to investigate the link between the macroscopic properties of a structure and its microscopic constituents. When we think of colloids as basic building blocks of a certain structure, it is then natural to ask what the properties of that structure will be if we change the building block and/or the mutual interactions between these building blocks. Once we understand these links, then we can use colloidal self-assembly as a

simple and inexpensive route to fabricate the structure of interest bottom-up. This approach is nowadays known as colloidal LEGO [36], for obvious reasons, and it is exemplified in Fig. 1.2. There is a huge potential in this strategy, however it is also a non trivial way to go, since we do not know, a priori, which ingredients are needed to target a certain structure. This is the reason why computer simulations are so useful in this field, because they allow for a simple and (sometimes) fast way to scan the range of possible LEGO bricks and their interactions. This thesis represents yet one more step in this direction, as we will show in the next chapters. However, computer simulations are just one node of the colloidal science triangle, the other two being represented by experiments and theory. Experiments serve both as final and fundamental confirmation of the predictions made by theory and simulations, and to provide evidence of novel phenomena. Theoretical predictions can have a further reach than computer simulations, but still need to be tested and refined by numerical experiments. The fertile interaction between these different nodes is what makes colloidal science a rather unique field of research.

1.2 Thermodynamics, geometry and energy

We have seen that, by encoding an amount of information into colloidal building blocks, it is possible to fabricate a target structure via self-assembly. The phase resulting from the self-assembly is, for the particular thermodynamic conditions imposed on the system (density and temperature), the one minimising the (Helmholtz) free energy

$$F = U - TS \quad (1.1)$$

where U , S and T are the system internal energy, entropy and temperature, respectively. The entropy is related to the number of microscopic realisations W that yield a particular macroscopic configuration of the system via

$$S = k_B \ln W \quad (1.2)$$

with k_B Boltzmann's constant. What kind of information can be encoded into a colloidal particle? In general, we can change its shape and the way it interacts with other particles. In the following, we briefly introduce both approaches, also in view of the presented equations. For a more systematic discussion on the possible features of colloidal particles, see Refs. [17, 37–43].

1.2.1 Hard particles

A system is called entropy-driven if its phase behaviour is dictated only by entropy. In entropy driven systems, the phases that can be observed depend only on the particle shape, and on the density of the system, whereas the temperature does not play any role. This is the case of hard particle models, in which particles do not interact with each other except for instantaneous elastic collisions. For two arbitrary objects O_1 and O_2 the hard-core interaction energy u is given by

$$u^{\text{HC}}(O_1, O_2) = \begin{cases} \infty & \text{if } O_1 \text{ and } O_2 \text{ overlap} \\ 0 & \text{otherwise} \end{cases} \quad (1.3)$$

Classical examples of such systems are colloidal hard spheres which display the conventional FCC crystal phase, but also rods, and discs, which additionally form plastic and liquid crystal phases [14, 44–48]. In more recent years many other shapes have become available thanks

to the advances in chemical synthesis: cubes [49], tetrahedra [50], truncated cubes [51], tetrapods [52], stars [53, 54], and superballs [55] are just a few examples of a steadily increasing variety. The particle shape is among the most basic information that can be encoded into colloidal particles, however studying the self-assembly of different particle shapes is far from trivial. We investigate the phase behaviour of two different mixtures of hard particles in Ch. 5 and Ch. 6.

1.2.2 Interacting particles

In the case of particles interacting with one another, the balance between internal energy and entropy determines the corresponding stable phases for a given density and temperature. Often, an isotropic attraction between colloidal particles can be well described by a simple hard-core square-well potential of a given range

$$u^{\text{SW}}(r_{ij}) = \begin{cases} \infty & \text{if } r_{ij} \leq \sigma \\ -\varepsilon & \text{if } \sigma \leq r_{ij} < \sigma + \Delta \\ 0 & \text{if } r_{ij} \geq \sigma + \Delta \end{cases} \quad (1.4)$$

where $r_{ij} = |\mathbf{r}_j - \mathbf{r}_i|$ is the center-to-center distance between particle i and particle j , σ is the particle diameter, ε is the absolute attraction strength, and Δ is the attraction range. The phase behaviour induced by such a potential is well-known, and we sketch it in Fig. 1.3 for sake of completeness. The main differences with respect to hard particles is that, for low enough temperatures, the interparticle attraction induces first a phase separation of the fluid phase into gas and liquid, and then a phase separation between gas and crystal phases. The limit of hard particles is recovered for high temperatures.

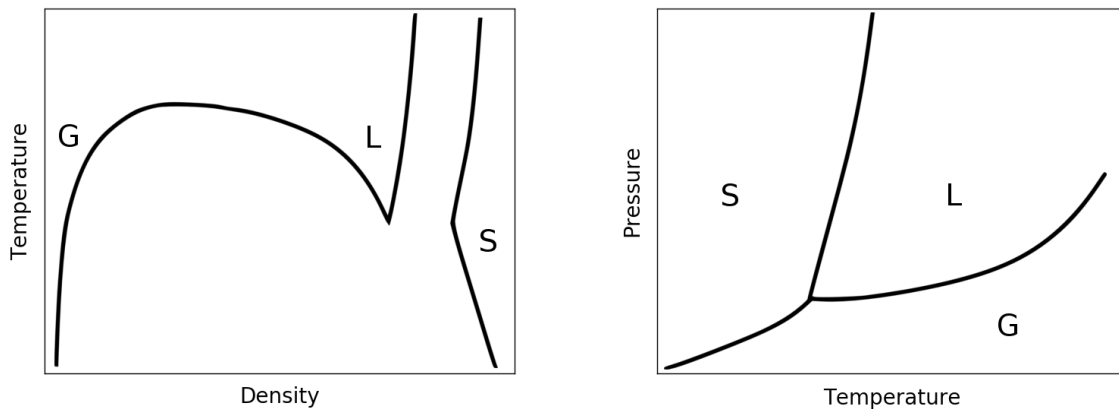


Figure 1.3: Phase diagrams of a system consisting of particles that interact with a sufficiently long-ranged isotropic attraction as the one defined in Eq. 1.4. The labels G, L, and S stand for Gas, Liquid and Solid phases, respectively. (left) Temperature–density plane. (right) Pressure–Temperature plane.

1.2.3 Patchy particles

Isotropic interactions can usually target compact crystalline structures. However, in order to self-assemble more open structures, it is advantageous to use anisotropic interactions. In this framework, particles will interact with one another only at specific sites on their surfaces, which are covered by interacting patches. These particles are often referred to as “patchy” particles. A simple model for patchy particles is the so-called Kern-Frenkel (KF) model [56], named after the scientists who investigated it first. It consists of a square-well attraction which is located only at some specific spots of a particle. More details on this model can be found in Ref. [56]. In order to interact, two patchy particles must not only be close enough to one another, but they must also have a specific orientation with respect to each other, i.e. some patches on the respective particles have to face. A realisation of a tetrahedral patchy particle model is shown for reference in Fig. 1.4.

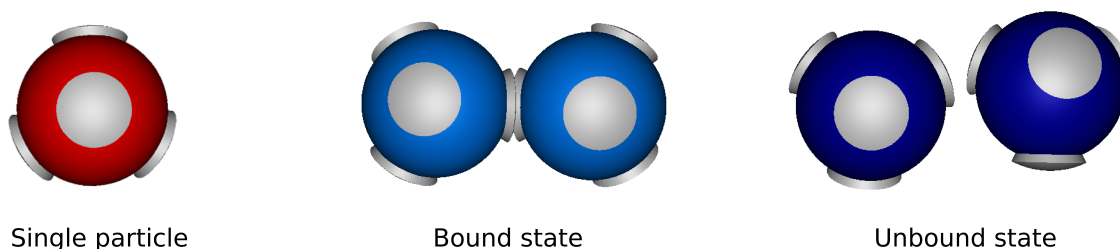


Figure 1.4: Tetrahedral patchy particles in the Kern-Frenkel model. (left) Top view of a single patchy particle. (middle) Bound state of two patchy particles. (right) Unbound state of two patchy particles.

Patchy particles can be used to stabilise, for instance, a diamond crystal structure (DC) over an FCC or a fluid [57, 58]. This is interesting for applications because the DC is a very promising photonic crystal [59, 60]. However, the experimental synthesis and control of patchy particles of the KF kind are not as advanced as the theoretical studies yet, despite the stunning progress that has recently been made [38, 40, 61–71].

A perhaps easier approach to give colloids directional interactions is to combine isotropic attractions and geometrical constraints. For example, fusing together one attractive bead and one non-interacting bead results in a particle which has already a directional interaction, since nothing can attach from one specific side. So we can gain a directional attraction, but we have to give up on the spherical particle shape. Note that this is hardly a compromise because, as we have seen earlier in the section, the anisotropy in particle shape only widens the range of possible target structures.

How can we make such colloidal particles? In the computer simulations this is rather easy, as we only need to correctly model the particle geometry and then place a square-well attraction on a specific bead in the particle. In experiments, usually two ingredients are needed: the depletion attraction, and a difference in surface roughness of the different beads. The depletion attraction is an entropic force that arises between colloidal particles when they are mixed in a solvent together with non-adsorbing polymers (also called depletants). Because the polymers gain a huge amount of entropy if colloidal particles get close to one another, this will be the preferred system configuration, thus the colloidal particles will have an effective isotropic at-

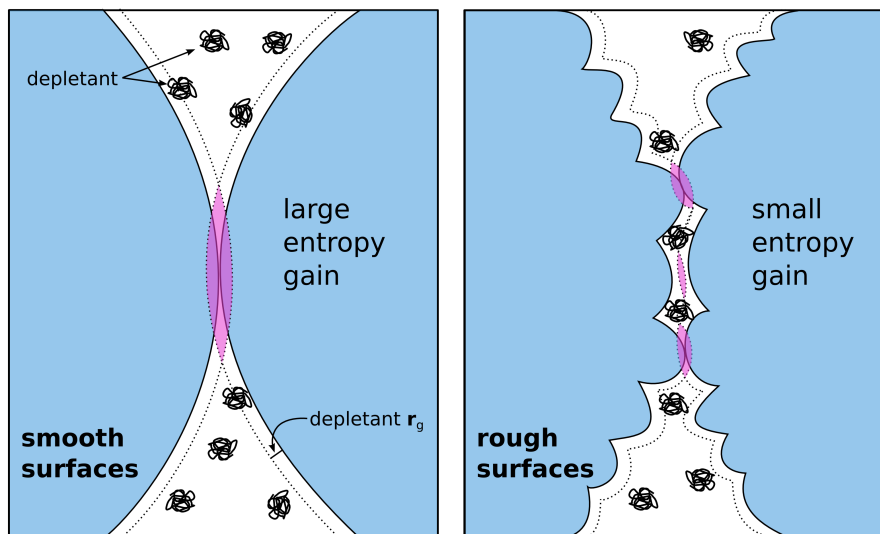


Figure 1.5: Depletion attraction between particles with smooth surfaces and particles with rough surfaces.

traction with each other [72, 73]. The key to make this attraction site-specific is the surface roughness difference. It has been recently demonstrated that the depletion attraction between colloidal beads with a rough surface is much smaller than the one between colloidal beads with a smooth surface [74–76]. Hence, by making a colloidal particle with beads that differ in surface roughness and by adding depletants to the suspension, we create a system of particles with anisotropic shape and with site-specific, patchy, interactions [77–79]. This concept is illustrated in Fig. 1.5. We study the phase behaviour of patchy particles and particles with site-specific attractions in Ch. 2,3, and 4.

Another route to experimental patchy particles is to covalently coat colloidal particles with complementary DNA strands [80–82]. The complementary DNA strands will provide the binding affinity, which is of the order of few $k_B T$ per base pair. Inert DNA strands usually provide steric stabilisation. The challenge here is to coat only specific areas of the colloids, so that their interaction can be effectively considered directional [69]. Beautiful examples of self-assembly of patchy DNA-coated colloids, displaying colloidal molecules in different configurations resembling molecular orbitals, have been given in Ref. [67]. Although DNA-coated colloidal particles are also a very appealing topic, in this thesis we did not study them, hence we refer the interested reader to other works, such as Refs. [83, 84].

1.3 Computational techniques

In this section we briefly discuss the main methods used in this thesis. In particular, we discuss the Monte Carlo simulations in different ensembles, the calculation of the free energy of a system via the thermodynamic integration method, and the calculation of the phase coexistence in binary mixtures.

1.3.1 Monte Carlo simulations

Monte Carlo (MC) simulations allow one to sample the phase space of a many-particle system and calculate its equilibrium properties. Let us consider a system in the canonical ensemble, where the number of particles N , the volume V , and the temperature T are fixed. The Hamiltonian of the system depends on the particle positions \mathbf{r}^N and momenta \mathbf{p}^N , and can be written as

$$H(\mathbf{r}^N, \mathbf{p}^N) = \sum_{i=1}^N \frac{\mathbf{p}_i^2}{2m} + U(\mathbf{r}^N) \quad (1.5)$$

where $U(\mathbf{r}^N)$ is the system potential energy. The partition function in the canonical ensemble reads

$$Z(N, V, T) = \frac{1}{N!h^{3N}} \int d\mathbf{r}^N d\mathbf{p}^N \exp(-\beta H(\mathbf{r}^N, \mathbf{p}^N)) \quad (1.6)$$

where $\beta = 1/k_B T$, k_B is the Boltzmann's constant, and h is Planck's constant. In this formalism, the average of any observable \mathcal{O} is given by

$$\langle \mathcal{O} \rangle = \frac{1/(N!h^{3N}) \int d\mathbf{r}^N d\mathbf{p}^N \mathcal{O}(\mathbf{r}^N, \mathbf{p}^N) \exp(-\beta H(\mathbf{r}^N, \mathbf{p}^N))}{Z} \quad (1.7)$$

If the observable is a static quantity, it depends on the particle positions, but not on the particle momenta. In this case – carrying out the integration over the momenta – the average simplifies to

$$\langle \mathcal{O} \rangle = \frac{\int d\mathbf{r}^N \mathcal{O}(\mathbf{r}^N) \exp(-\beta U(\mathbf{r}^N))}{\int d\mathbf{r}^N \exp(-\beta U(\mathbf{r}^N))} \quad (1.8)$$

However, even this simpler expression cannot be integrated directly due to the large number of configurations that has to be sampled. The solution to this problem is to recognise that Eq. 1.8 is equivalent to a weighted average of $\mathcal{O}(\mathbf{r}^N)$ according to a Boltzmann distribution. Hence, by sampling system configurations that are Boltzmann-distributed, we can estimate $\langle \mathcal{O} \rangle$ as

$$\langle \mathcal{O} \rangle = \frac{1}{M} \sum_k^M \mathcal{O}(\mathbf{r}_k^N) \quad (1.9)$$

where M is the total number of sampled configurations and \mathbf{r}_k^N denotes the particle coordinates in the k -th configuration. This is known as the Metropolis method, after the scientist who first devised it [85, 86].

In practice, an MC simulation generates a Markov chain of random system configurations. Starting with a given particle configuration \mathbf{r}_{old}^N , a new configuration is \mathbf{r}_{new}^N obtained by randomly displacing or rotating by a small amount a single random particle at once. This new

configuration is accepted or rejected according to the Metropolis rule

$$\text{acc}(\mathbf{r}_{old}^N \rightarrow \mathbf{r}_{new}^N) = \min(1, \exp\{-\beta [U(\mathbf{r}_{new}^N) - U(\mathbf{r}_{old}^N)]\}) \quad (1.10)$$

If the move is rejected, the old configuration is restored and counted again, if instead the move is accepted, the new configuration becomes the start for a new iteration. A schematic of this process, for a system of hard disks, is given in Fig. 1.6.

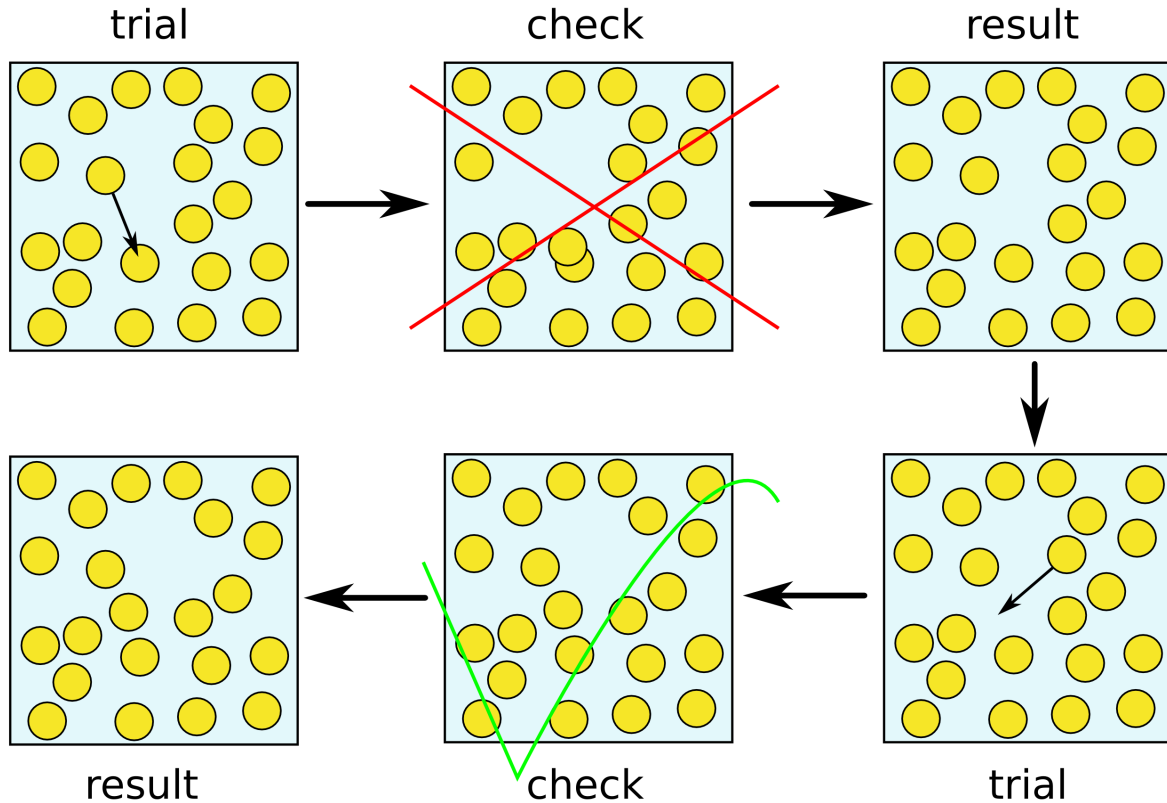


Figure 1.6: Illustration of a Monte Carlo translation move. Starting with a given configuration, a change in the position of one particle is attempted, and tested against the Metropolis condition. If the change is rejected, the old state is restored, else the simulation continues with a new iteration.

Different MC moves and acceptance rules can be devised to simulate different statistical ensembles. For instance, in the isobaric-isothermal ensemble – where the number of particles N , the pressure P , and the temperature T are fixed – one can change the volume V of the box containing the particles and accept this move with probability

$$\text{acc}(V_{old} \rightarrow V_{new}) = \min(1, \exp\{-\beta [\Delta U + P\Delta V - k_B T N \log(V_{new}/V_{old})]\}) \quad (1.11)$$

The box in an NPT simulation can either have a fixed or a fluctuating shape. In the latter case we talk about “floppy-box” Monte Carlo, or FBMC. The FBMC is used to simulate particles in a stress-free environment, and additionally deals with crystal structures whose unit cell is non cubic [87, 88]. In this case, moves that randomly change the three vectors spanning the

simulation box need to be implemented, but the acceptance rule is the same as for an ordinary NPT simulation. To simulate a system in the grand canonical ensemble, with fixed chemical potential μ , volume V , and temperature T , one needs to try and insert or remove a single particle from the simulation box. For an exhaustive description of these and other simulation methods, see Refs. [89, 90].

1.3.2 Free-energy calculations

In order to draw the phase diagram of a particular system, we need to calculate the free energy for different phases at different thermodynamic conditions and pick the phase with minimal free energy. In the following we discuss the case of a system of hard particles. To calculate free energies, we use the thermodynamic integration method, which relates the system equation of state (EOS) $P = P(\rho)$ to a free energy difference via

$$\frac{\beta F(\rho)}{N} = \frac{\beta F(\rho_0)}{N} + \int_{\rho_0}^{\rho} d\rho' \frac{\beta P(\rho')}{\rho'^2} \quad (1.12)$$

which trivially follows from the the derivative of the free energy per particle with respect to the density of the system

$$\left(\frac{\partial F/N}{\partial \rho} \right) = \frac{P(\rho)}{\rho^2} \quad (1.13)$$

Therefore, all one needs to know in order to calculate the free energy of the system at a certain density ρ is the free energy at a reference point ρ_0 and the EOS of the system. Thus, the main focus is shifted to the calculation of the free energy at the specific reference point.

For the fluid phase, we can always start from a very low density, such that the particles behave like an ideal gas, for which the free energy is analytically known.

For a crystal phase, the reference point cannot be set to the ideal gas, as the path would cross the fluid-solid phase transition line. Instead, the reference point is set to an Einstein crystal, which is a collection of harmonic oscillators regularly arranged. The free energy of an Einstein crystal is also analytically known. To connect the Einstein crystal with potential energy U_I and the crystal of interest with potential energy U_{II} one uses a fictitious potential which depends on a switching parameter λ

$$U(\lambda) = (1 - \lambda)U_I + \lambda U_{II} \quad (1.14)$$

Here, the parameter λ varies between 0 and 1 in such a way that when $\lambda = 0$ we recover the reference system with potential energy U_I , while when $\lambda = 1$ we recover the system of interest with potential energy U_{II} . The free-energy difference along such a λ -path is given by [90]

$$F(\lambda = 1) - F(\lambda = 0) = \int_{\lambda=0}^{\lambda=1} d\lambda \left\langle \frac{\partial U(\lambda)}{\partial \lambda} \right\rangle_{\lambda} \quad (1.15)$$

where $\langle \partial U(\lambda)/\partial \lambda \rangle_{\lambda}$ can be obtained by an MC simulation. Once the free-energy curves as function of the density are known for two phases, one can use the so called common tangent construction to locate the phase coexistence boundaries. The common tangent construction, in the context of binary mixtures, is discussed in the next section.

1.3.3 Common tangent construction for binary mixtures

In the following, we briefly introduce the theory behind the common tangent construction method to locate coexistence regions. We follow closely the derivation of Ref. [91]. Let us consider a binary system of N_1 particles of type 1 and N_2 particles of type 2 at a pressure P and temperature T , with $N = N_1 + N_2$. The system's Gibbs free energy $G = (F + PV)$, is related to the chemical potential of the two species via

$$G = G(N_1, N_2, P, T) = N_1\mu_1 + N_2\mu_2 \quad (1.16)$$

so that a differential change in dG can be written as

$$dG = -SdT + VdP + \mu_1dN_1 + \mu_2dN_2 \quad (1.17)$$

It is useful to define the Gibbs free energy per particle as $g = G/N$ and rewrite the above equations as

$$g = x\mu_1 + (1-x)\mu_2 \quad (1.18)$$

$$dg = -sdT + vdP + (\mu_1 - \mu_2)dx \quad (1.19)$$

from which we see that g depends on the pressure P , the temperature T , and the composition of the system $x = N_1/N$, meaning $g = g(x, P, T)$. Thus, $G(N_1, N_2, P, T) = Ng(x, P, T)$, which is also what we expect since the Gibbs free energy is an extensive quantity. In the single component case, we see that the Gibbs free energy per particle coincides with the chemical potential of the system.

Finally, we can rewrite the chemical potentials of both species as

$$\mu_1 = \left(\frac{\partial G}{\partial N_1} \right)_{N_2, P, T} = g + (1-x) \left(\frac{\partial g}{\partial x} \right)_{P, T} \quad (1.20)$$

$$\mu_2 = \left(\frac{\partial G}{\partial N_2} \right)_{N_1, P, T} = g - x \left(\frac{\partial g}{\partial x} \right)_{P, T} \quad (1.21)$$

Now we turn to the conditions of thermodynamic equilibrium for two binary phases, say α and β . The pressure, the temperature, and the chemical potential of each species must be equal in both phases for the system to be at equilibrium, namely

$$P^\alpha = P^\beta \quad (1.22)$$

$$\mu_1^\alpha = \mu_1^\beta \quad (1.23)$$

$$\mu_2^\alpha = \mu_2^\beta \quad (1.24)$$

The chemical equilibrium conditions Eq. 1.23 and 1.24 help us locating the coexistence curve. In view of Eq. 1.20 and 1.21 we can rewrite them as

$$\left(\frac{\partial g}{\partial x} \right)_{P, T}^\alpha = \left(\frac{\partial g}{\partial x} \right)_{P, T}^\beta \quad (1.25)$$

$$(x^\alpha - x^\beta) \left(\frac{\partial g}{\partial x} \right)_{P, T}^\alpha = g^\alpha - g^\beta \quad (1.26)$$

which means that the coexistence points in the (g, x) plane have the same slope and they have a common tangent. Graphically, this is shown in Fig. 1.7 for an arbitrary Gibbs free energy curve.

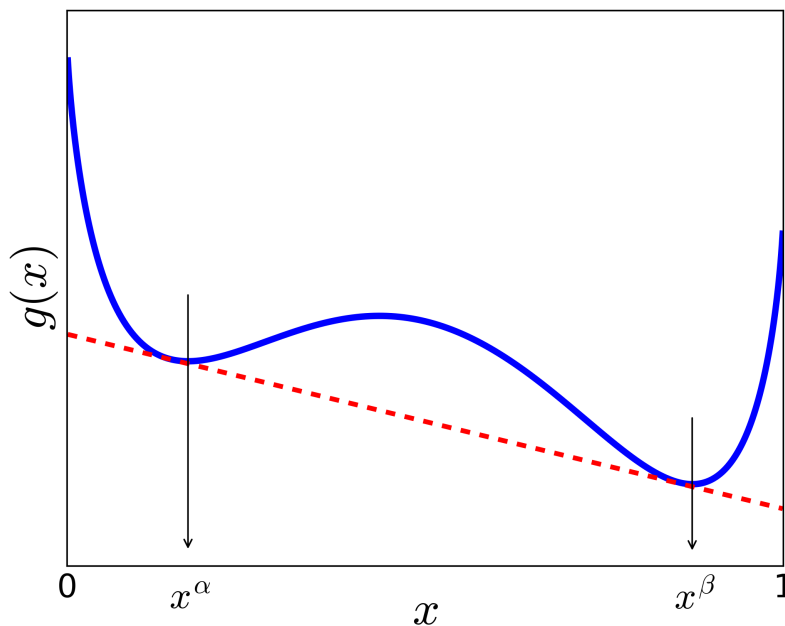


Figure 1.7: Schematics of the common tangent construction between two phases α and β : phase α is stable for $x < x^\alpha$, phase β is stable for $x > x^\beta$ and for $x^\alpha < x < x^\beta$ there is a phase coexistence region.

1.4 Scope of this thesis

The purpose of this thesis is to study the phase behaviour and the self-assembly of colloids with anisotropic shape and anisotropic interactions using Monte Carlo simulations and the other computational methods described in the previous sections. This thesis can be divided into two parts.

Part I, consisting of Chapters 2, 3, and 4, deals with the self-assembly and fluid phase behaviour of “patchy” particles and particles with site-specific attractions. Also, all the self-assembly phenomena depicted in part I take place in a low density regime. In **Chapter 2**, we study the structures that can be self-assembled by patchy colloidal dumbbells, dimers with anisotropic interactions. In **Chapter 3**, we study the self-assembly products of the so-called “Mickey Mouse” particles, which are trimers with an attractive inner bead and two repulsive outer beads. We additionally compare our results to experiments performed on a colloidal realisation of this system by Wolters and coworkers [79], and find a reasonable agreement, given our simple simulation model. In **Chapter 4**, we study the gas-liquid phase separation of “Mickey Mouse” particles and its interplay with the self-assembly behaviour observed in Chapter 3.

Part II, consisting of Chapters 5 and 6, deals with the phase behaviour of two different binary mixtures of hard particles. In **Chapter 5**, we study a mixture of hard spheres and hard tetrahedral clusters of spheres. In particular, we show that this system could be used to target a structural analogue of the MgCu_2 Laves phase, which can be turned into the Diamond crystal, well-known as the “photonic champion”. In **Chapter 6**, we study a mixture of hard spheres and hard icosahedral clusters of spheres. Specifically, we study the stability of the AB_{13} crystal

phase with respect to the fluid phase. All the structures studied in part II lie in the high density regime.

The work presented in this thesis represents yet another step towards the understanding of how complex shape and interaction influence the self-assembly of colloidal particles and how this can be exploited to fabricate new functional materials.

Part I

Particles with anisotropic shape and interactions

Self-assembly of patchy colloidal dumbbells

We employ Monte Carlo simulations to investigate the self-assembly of patchy colloidal dumbbells interacting via a modified Kern-Frenkel potential by probing the system concentration and dumbbell shape. We consider dumbbells consisting of one attractive sphere with diameter σ_1 and one repulsive sphere with diameter σ_2 and center-to-center distance d between the spheres. For three different size ratios $q = \sigma_2/\sigma_1$, we study the self-assembled structures for different separations $l = 2d/(\sigma_1 + \sigma_2)$ between the two spheres. In particular, we focus on structures that can be assembled from the homogeneous fluid, as these might be of interest in experiments. We use cluster order parameters to classify the shape of the formed structures. When the sizes of the two spheres are almost equal, $q = 1.035$, we find that, upon increasing l , spherical micelles are transformed to elongated micelles and finally to vesicles and bilayers. For size ratio $q = 1.25$ we observe a continuously tunable transition from spherical to elongated micelles upon increasing the sphere separation l . For size ratio $q = 0.95$ we find bilayers and vesicles, plus faceted polyhedra and liquid droplets. Our results identify key parameters to create colloidal vesicles with attractive dumbbells in experiments.

2.1 Introduction

Colloidal self-assembly refers to the self-organisation process of nano- to micrometer-sized colloidal particles into larger structures [92]. This process can be used for the fabrication of novel materials [65, 67, 93] and has potential applications in e.g. photonics [26, 59, 94, 95], food industry [96, 97], and medicine [98–100]. The ability to guide the self-assembly allows for a bottom-up approach to design and create specific materials. One way to achieve such guidance, is to engineer colloidal particles with discrete, attractive patches at well-defined locations on the surface of the particles [37]. As several tuning parameters can in principle affect the self-assembly process, computer simulations provide an invaluable tool to explore the self-assembly of patchy particle models.

One of the simplest patchy particle model is a sphere where one half is covered with an attractive patch that can interact with a similar patch on another sphere. The self-assembly of these so-called “Janus” particles has been investigated in computer simulations [43, 101] and revealed the spontaneous formation of micelles and vesicles together with wrinkled sheets and different crystal structures [102–105]. In addition to Janus particles, past computer simulation studies have also investigated the effects of the number of patches and their surface distribution [106–108], as well as the patch coverage fraction, patch shape and interaction range [57, 58, 109, 110] on the structure and the phase behaviour of patchy particles. On the experimental side, patchy particles can be synthesised in a large variety of shapes and with different patchy properties [42, 70, 111]. In some cases, the particles are already used to form complex ordered structures, e.g. clusters [103, 112, 113] and Kagome lattices [66, 114].

While many patchy particle models have been investigated, most systematic studies have focused on spherical colloids. Some studies have been performed on dumbbells with a selective attraction on one of the spheres. Experimentally, patchy dumbbells can be realised by creating a variation in the surface roughness between the two spheres [78]. By introducing a specific amount of depletant to the system, a selective attraction between the smooth spheres of the dumbbells can be created, whereas the rough spheres remain repulsive. As a result, dumbbells can self-assemble into small clusters to form a micellar fluid. Previous theoretical works on attractive dumbbells have confirmed the existence of a micellar fluid and also reported bilayer formation [115]. Bilayer formation has also been observed in simulations of tangential hard dumbbells with tunable attraction strength [116, 117]. However, spontaneous vesicles formation, which is found in molecular surfactants [118], remains unobserved at the level of computer simulations of patchy colloidal dumbbells.

In this chapter, we use computer simulations to address the self-assembly of non-overlapping patchy dumbbells with an interaction range of half the diameter of the attractive sphere. This is considerably longer than the interaction range in most of the experiments with depletion interactions [78, 79], but it is still realistic for e.g. nanoparticles or other types of interactions. We show that there are regions in our parameter space where we observe vesicle formation. Furthermore, we also observe structures which were previously reported, such as bilayers and micelles. The formation of the different structures is achieved by varying the size ratio and the sphere separation of the dumbbells, as well as the volume fraction of the system.

2.2 Model and methods

In this section, we introduce the model definition and the method used to address the self-assembly of dumbbell-shaped particles. The dumbbells are understood to interact with one another and hereafter are referred to as “attractive” dumbbells. The details on how a single dumbbell particle is built and how the attractive potential is defined are found in subsection 2.2.1, while the details on the simulation and analysis methods follow in subsections 2.2.2 and 2.2.3, respectively.

2.2.1 Geometry and interaction potential

Each dumbbell is assembled as follows: one attractive hard sphere of diameter σ_1 (red sphere in Fig. 2.1) is placed at distance d from another non-interacting hard sphere of diameter σ_2 (blue sphere in Fig. 2.1) which acts as a steric constraint. Thus, the geometrical parameters are the size ratio, $q = \sigma_2/\sigma_1$, and the dimensionless sphere separation, $l = 2d/(\sigma_1 + \sigma_2)$. When the attractive hard sphere is completely buried within the hard sphere at $l = |\sigma_2 - \sigma_1|/(\sigma_1 + \sigma_2)$ we simulate a Janus hard dumbbell, while for $l = 1$ we obtain a dumbbell consisting of tangent hard spheres. Furthermore, each dumbbell carries a normalised orientation vector, $\hat{\mathbf{e}}$, pointing

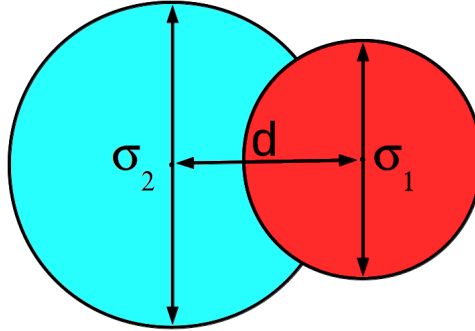


Figure 2.1: Graphical representation of the geometry of one patchy dumbbell particle consisting of an attractive sphere of type 1 (red) and a non-interacting hard sphere of type 2 (blue).

from the centre of the non-interacting hard sphere towards the attractive sphere. The interaction between a pair of dumbbells i and j is the sum of an attractive and a repulsive contribution,

$$u_{ij} = u_{ij}^{\text{att}} + u_{ij}^{\text{rep}} \quad (2.1)$$

The attractive contribution, u_{att} , is based on the Kern-Frenkel potential [56], but here we also take into account the non spherical particle shape. The final form of the attractive patchy interaction reads,

$$u_{ij}^{\text{att}} = u^{\text{SW}}(r_{ij}^{11}) f(\hat{r}_{ij}^{11}, \hat{\mathbf{e}}_i, \hat{\mathbf{e}}_j) \quad (2.2)$$

where \hat{r}_{ij}^{11} is the normalised vector connecting the attractive spheres of dumbbells i and j , $r_{ij}^{11} = |\mathbf{r}_{j,1} - \mathbf{r}_{i,1}|$ denotes the absolute centre-of-mass distance between the attractive spheres of dumbbells i and j . The square-well interaction in Eq. 2.2 is defined as:

$$\beta u^{\text{SW}}(r_{ij}^{11}) = \begin{cases} \beta \varepsilon & \text{for } \sigma_1 \leq r_{ij}^{11} < \sigma_1 + \Delta \\ 0 & \text{for } r_{ij}^{11} \geq \sigma_1 + \Delta \end{cases} \quad (2.3)$$

where $\beta = 1/k_B T$ is the inverse temperature, k_B the Boltzmann's constant, $\varepsilon < 0$ and Δ are the square-well (SW) parameters representing, respectively, the interaction strength and range. The orientational part gives directionality to the attractive potential and reads:

$$f(\hat{r}_{ij}^{11}, \hat{\varepsilon}_i, \hat{\varepsilon}_j) = \begin{cases} 1 & \text{if } \left\{ \begin{array}{l} \hat{\varepsilon}_i \cdot \hat{r}_{ij}^{11} \geq \cos \delta \\ \text{and } \hat{\varepsilon}_j \cdot \hat{r}_{ji}^{11} \geq \cos \delta \end{array} \right. \\ 0 & \text{otherwise} \end{cases} \quad (2.4)$$

The opening angle δ depends on the geometry of the particle via the relation:

$$\cos \delta = \frac{1}{4d\sigma_1} \cdot (\sigma_2^2 - \sigma_1^2 - 4d^2) \quad (2.5)$$

and follows from trigonometry by connecting the centre of mass of the small attractive sphere to the intersection point between the small attractive sphere and the larger non-interacting hard sphere. As a consequence, the attractive spheres on two different dumbbells cannot interact with each other through the volume of the non-interacting hard spheres.

Finally, the repulsive part assures that two hard dumbbells i and j do not overlap with each other and reads:

$$u_{ij}^{\text{rep}} = \sum_{\alpha, \beta=1,2} u^{\text{HS}}(|\mathbf{r}_{i,\alpha} - \mathbf{r}_{j,\beta}|) \quad (2.6)$$

where each hard-sphere contribution is given by:

$$u^{\text{HS}}(|\mathbf{r}_{i,\alpha} - \mathbf{r}_{j,\beta}|) = \begin{cases} \infty & \text{if } |\mathbf{r}_{i,\alpha} - \mathbf{r}_{j,\beta}| < \sigma_{\alpha,\beta} \\ 0 & \text{otherwise} \end{cases} \quad (2.7)$$

with $\sigma_{\alpha,\beta} = (\sigma_\alpha + \sigma_\beta)/2$ representing the centre of mass distance at which sphere α and β are in contact.

A representation of two interacting dumbbells is given in Fig. 2.2, for two different values of δ . Note that the attractive region (in orange) does not intersect with the non-interacting hard sphere on the same dumbbell.

2.2.2 Monte Carlo simulations

We perform Monte Carlo simulations in the canonical ensemble (MC-NVT) with $N = 1024$ dumbbells in a volume V and temperature T with cubic periodic boundary conditions. We define the volume fraction $\phi = \rho V_{DB}$ inside the simulation box, where $\rho = N/V$ denotes the total number density, and V_{DB} is the volume of a single dumbbell. We employ single particle translation and rotation moves [90] to explore the configurational phase space. The simulations are $2 - 6 \times 10^7$ MC steps long, where a single MC step is defined as N attempted moves (either translations or rotations). During the simulation equilibration time (half of the total simulation length), the maximum displacement and the maximum angular change are periodically adjusted to obtain acceptance ratios of 30% for both translational and rotational moves. After the equilibration, the values are fixed.

Summing up, our model possesses a five-fold parameter space $\{\phi, \beta\varepsilon, \Delta/\sigma_1, l, q\}$, denoting the volume fraction ϕ , the well depth $\beta\varepsilon$, the interaction range Δ/σ_1 , the dimensionless distance

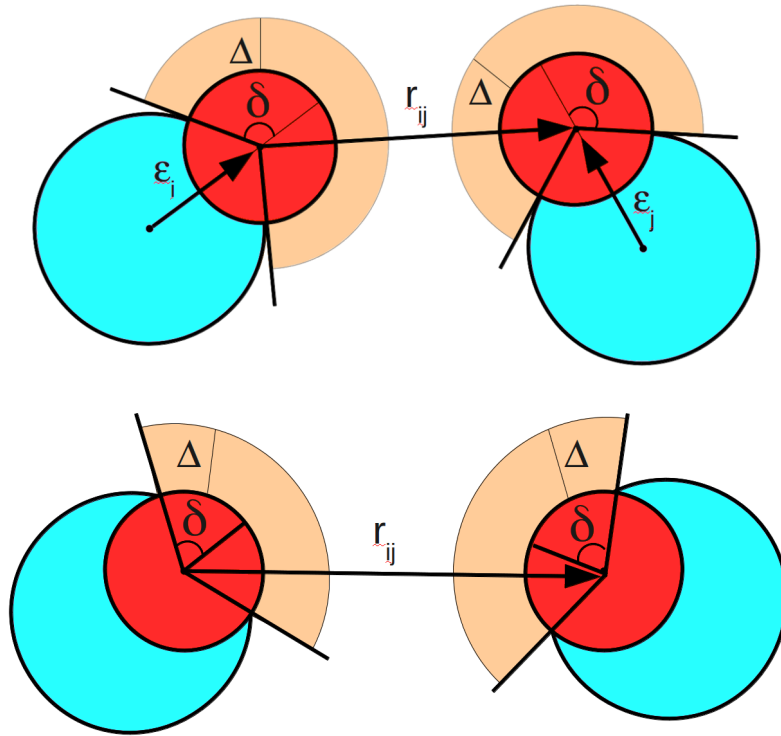


Figure 2.2: Graphical representations of the interaction between a pair of patchy hard dumbbells in two different cases. Top panel: dumbbells with size ratio $q = \sigma_2/\sigma_1 = 1.25$ and dimensionless sphere separation $l = 2d/(\sigma_1 + \sigma_2) > 1/3$, corresponding to $\delta > 90^\circ$. Bottom panel: dumbbells with size ratio $q = \sigma_2/\sigma_1 = 1.25$ and dimensionless sphere separation $l = 2d/(\sigma_1 + \sigma_2) < 1/3$, corresponding to $\delta < 90^\circ$ (bottom panel). The attractive spheres are denoted with red, the non-attractive spheres are denoted with blue. The orange area represents the interaction range.

l between the two spheres in the dumbbell, and the size ratio q between the non-interacting hard sphere and the attractive sphere. Throughout this work, we fix the interaction strength to $\beta\varepsilon = -3.58$, which is sufficient to observe self-assembly [117]. For all our simulations, we set the interaction range $\Delta = 0.5\sigma_1$, to half the diameter of the attractive sphere in the dumbbell, similar to the interaction range used previously to study Janus particles [102] and patchy dumbbells [116, 117].

2.2.3 Structure classification via cluster analysis and order parameters

To compare the outcome of computer simulations for different parameters, we choose a systematic approach to analyse the final configuration of a simulation. To this end, we employ a cluster analysis method and use three order parameters to classify the clusters. This approach is similar to the one used in Ref. [115], except here we introduce an additional order parameter in order to deal with the additional encountered structures. In Fig. 2.3 we show the typically encountered aggregate shapes, found for patchy dumbbells with size ratio $q = 1.035$: a spherical micelle (a), an elongated micelle (b), a vesicle (c,d), and a bilayer (e,f).

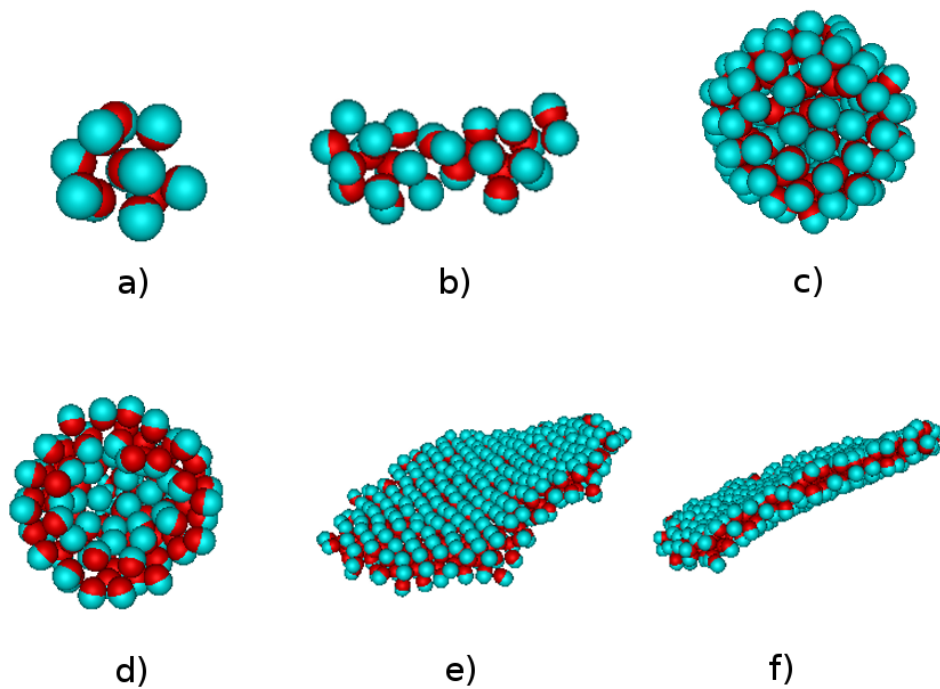


Figure 2.3: Most common self-assembled structures found for patchy dumbbells with size ratio $q = 1.035$ at the end of the simulation runs: a) spherical micelle $l = 0.08$, b) elongated micelle $l = 0.13$, c) vesicle $l = 0.20$, d) cut-through of a vesicle, e) and f) bilayers $l = 0.28$.

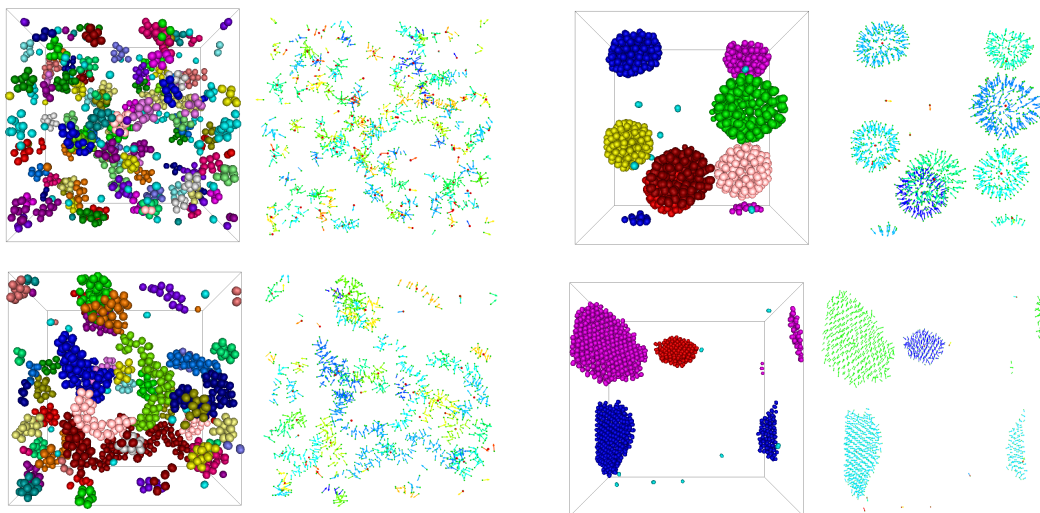


Figure 2.4: Example of the cluster analysis on the final configurations of different runs displaying (top left) spherical micelles, (top right) vesicles, (bottom left) elongated micelles, (bottom right) bilayers. For each panel, the simulation box is shown on the left and the analysis of the scene is shown on the right. The colour code distinguishes different clusters. The analysis on the right shows the centre of mass of each cluster in red, and for each dumbbell a green sphere and the orientation vector, with different colour to distinguish different clusters.

The procedure to identify and classify clusters is the following. First, we identify particles as interacting neighbours if they have a mutual bond, i.e. they attract each other according to Eq. 2.1. Then, a cluster is defined as a contiguous set of neighbouring particles. Examples of clusters identified with this procedure are given in Fig. 2.4. For each cluster found in the final configuration of a simulation run, we compute three cluster order parameters \mathcal{M} , \mathcal{B} and \mathcal{V} defined as

$$\mathcal{M} = \frac{1}{N_c} \sum_{i=1}^{N_c} \cos \theta_i \quad (2.8)$$

$$\mathcal{B} = \frac{2}{N_c(N_c - 1)} \sum_{(ij)} (\hat{\mathbf{e}}_i \cdot \hat{\mathbf{e}}_j)^2 \quad (2.9)$$

$$\mathcal{V} = \frac{1}{N_c} \sum_{i=1}^{N_c} (1 - \sin \theta_i) \quad (2.10)$$

where N_c is the number of dumbbells in the cluster and $\sum_{(ij)}$ denotes the sum over all particle pairs in a cluster. The quantity $\cos \theta_i$ is defined as

$$\cos \theta_i = \hat{\mathbf{e}}_i \cdot \frac{\mathbf{r}_{cm} - \mathbf{r}_i}{|\mathbf{r}_{cm} - \mathbf{r}_i|} \quad (2.11)$$

with \mathbf{r}_{cm} denoting the centre of mass of the cluster, \mathbf{r}_i indicating the centre of mass of dumbbell i and $\hat{\mathbf{e}}_i$ labelling the orientation of dumbbell i .

Label	Symbol	\mathcal{M}	\mathcal{B}	\mathcal{V}
Spherical Micelle		≥ 0.9	–	–
Elongated Micelle		< 0.9	< 0.4	–
Vesicle		< 0.5	–	> 0.5
Bilayer		< 0.5	≥ 0.4	–
Liquid Droplet		< 0.5	–	$\in [0.3, 0.5]$
Other				

Table 2.1: Criteria used to identify and label different clusters. Dash means the corresponding order parameter was not used for that particular label. If the clusters do not match any of the first five criteria, then they are classified as “Other”.

For a perfectly spherical micelle we have $\mathcal{M} = 1$, whereas $\mathcal{B} = 1$ for a bilayer, i.e. a collection of dumbbells that are aligned either perfectly parallel or anti-parallel with respect to each other. To further discriminate the structures, \mathcal{V} detects whether particles are not oriented

perpendicular with respect to the vector connecting them to the centre of mass of the clusters. For infinitely long and flat bilayers, \mathcal{V} would be low as the particles are oriented orthogonally to the vector connecting them to the centre of mass of the cluster.

We found the criteria in Table 2.1 appropriate to classify the shape of the clusters (more details can be found in Sec. 2.2.3.1). According to this classification, clusters cannot fall under multiple categories. Furthermore, when two or more symbols are found together, it means that at least 20% of the clusters belonged to the corresponding category. Although we rely on the automated classification method, we also use direct visual inspection as a consistency check. If we find disagreement between the two methods, visual inspection will be preferred. This case happens rarely and it will be explicitly mentioned in the captions of the following figures.

Using the depicted classification scheme, we can now map out, for varying size ratio q , the self-assembly state diagrams for patchy dumbbells in the sphere separation l –volume fraction ϕ representation.

2.2.3.1 Details on the structure classification

In order to identify and classify the self-assembled structures obtained for patchy dumbbells, we employ the order parameters \mathcal{M} , \mathcal{V} and \mathcal{B} as defined in Eq. 2.8, 2.9 and 2.10. In Fig. 2.5 we show the space of the order parameter values $(\mathcal{M}, \mathcal{V}, \mathcal{B})$ for clusters of patchy dumbbells for all the size ratios q , all the sphere separations l , and all the packing fractions ϕ that we considered in this study. Here, we consider all the results together for classification purposes.

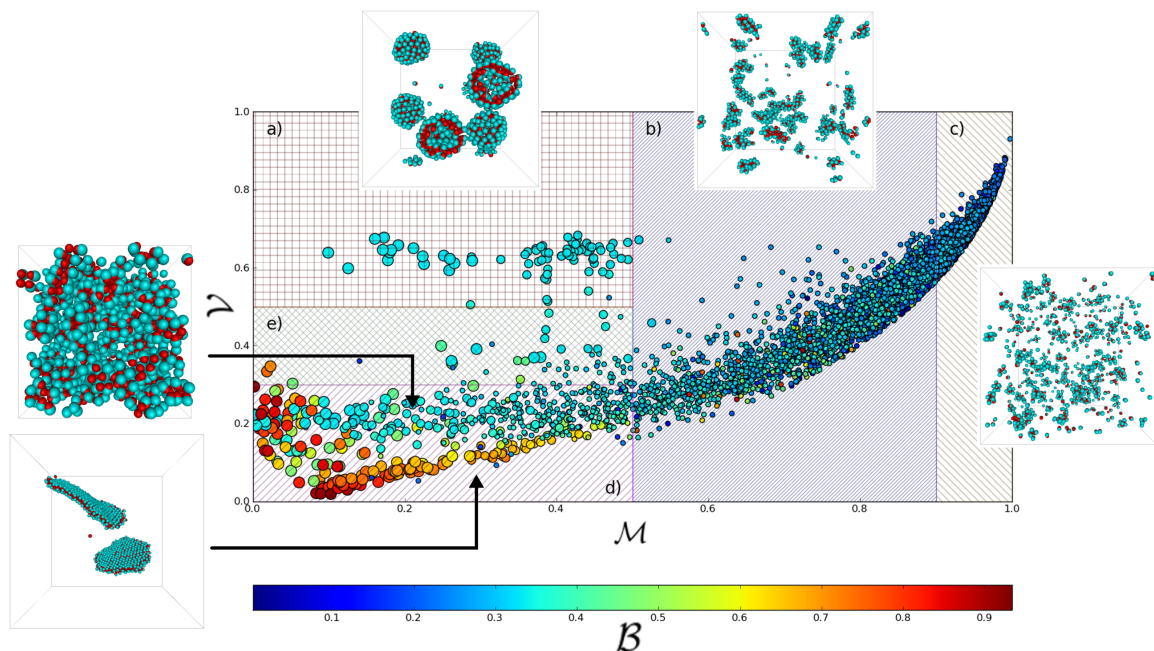


Figure 2.5: Scatter plot of the values of the order parameters in the $(\mathcal{V}, \mathcal{M})$ plane for all the different size ratios considered in this work ($q = 1.035$, $q = 1.25$, $q = 0.95$). Colour code and marker size stand for, respectively, the \mathcal{B} parameter and the size of the cluster (see text). The following main structures can be identified: vesicles (region “a”), elongated micelles (region “b” and “d”), spherical micelles (region “c”), and bilayers (region “d”). Faceted polyhedra and liquid droplets fall both into region “e” of the diagram.

In the $x - y$ plane we have the $(\mathcal{V}, \mathcal{M})$ parameters, while the \mathcal{B} parameter is used to colour code the markers. Additionally, markers of three different sizes have been used to encode the cluster size information in the plot (small dots $N_c \in [0, 75]$, medium dots $N_c \in [76, 260]$, large dots $N_c \in [261, 1024]$), in order to enhance its readability. We complement the plot in Fig. 2.5 with insets containing snapshots of the typical configurations in different regions of the diagram. We partition the diagram in different areas according to the values of the cluster order parameters, and we label them from “a” through “e”. The three main regions in the diagram, form the vesicle (a), the micellar (b, c and partially d) and the bilayer regime (d). The micellar regime transforms continuously from elongated micelles at low \mathcal{M} to more spherical micelles with increasing \mathcal{M} , and is identified by the main sequence in the diagram. Here, we have used a threshold value of $\mathcal{M} \geq 0.9$ to label aggregates as spherical micelles. The low- \mathcal{V} , low- \mathcal{M} area (d) encloses large aggregates with high degree of orientational order (\mathcal{B} parameter) – the bilayer-like aggregates – as well as smaller elongated micelles with a low value of \mathcal{B} . Somewhat in between the vesicles and the bilayer regimes, liquid-like droplets as well as faceted polyhedra are observed (partition e). Note that, as Fig. 2.5 is a cumulative diagram, not all the structures are present in every size ratio considered, but rather each size ratio contributes differently to the areas in the diagram. While we could make as many diagrams as size ratios considered, we prefer to have a global and unique way of detecting different kinds of aggregates.

2.3 Results

We have investigated the self-assembly of patchy dumbbells for three different size ratios, $q = 1.035$, $q = 1.25$ and $q = 0.95$. For each case, we have classified the structures according to the order parameters introduced in Sec. 2.2.3.

For $q = 1.035$, we observe a remarkably rich self-assembly behaviour, including the formation of micellar structures ranging from spherical to non-spherical shape. In addition, we also find vesicles and bilayers (see Fig. 2.6). Note that for the micelles (Fig. 2.6 top panels) the attractive spheres point inwards, whereas for the vesicles and the bilayers the dumbbells form a double-layer where a part of the attractive spheres points inwards and the other part of them outwards.

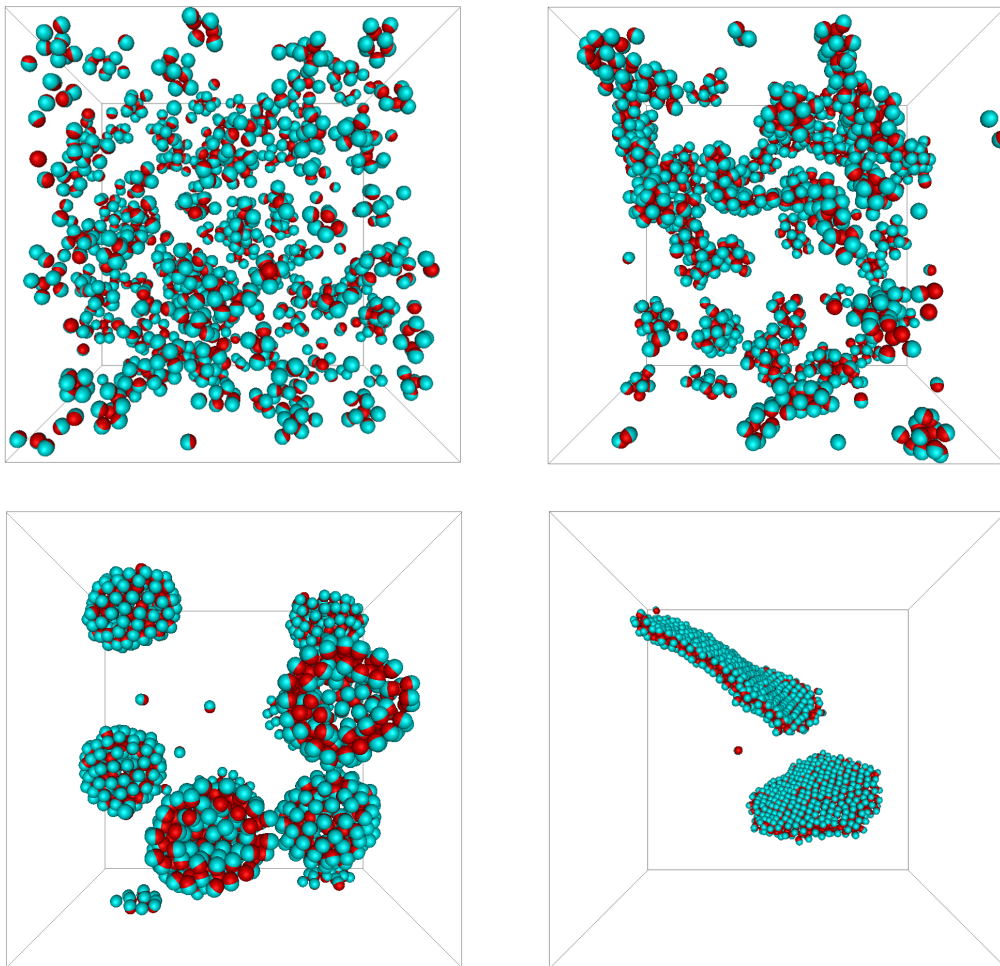


Figure 2.6: Typical simulation snapshots for patchy dumbbells with size ratio $q = 1.035$ for different values of volume fraction ϕ and sphere separation l . Top left: spherical micelles at $(\phi = 0.03, l = 0.05)$. Top right: elongated micelles at $(\phi = 0.03, l = 0.14)$. Bottom left: vesicles at $(\phi = 0.035, l = 0.175)$. Bottom right: bilayers at $(\phi = 0.008, l = 0.34)$.

The self-assembly state diagram for patchy dumbbells with size ratio $q = 1.035$ as a function of volume fraction ϕ and dimensionless sphere separation l is shown in Fig. 2.7. We find that the

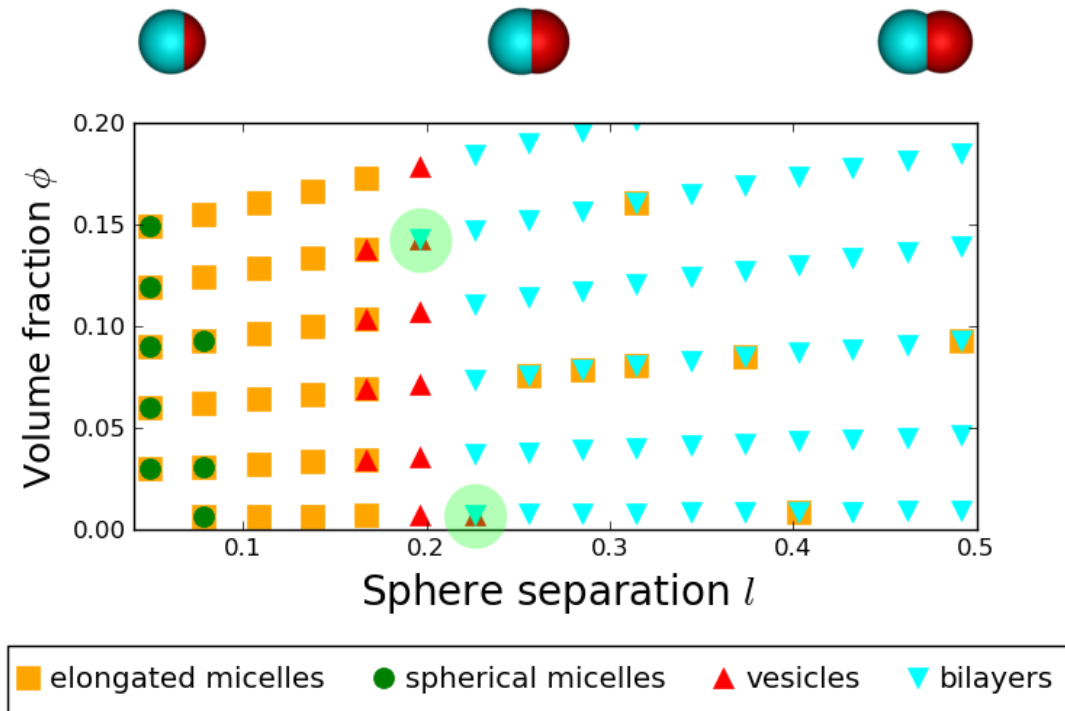


Figure 2.7: State diagram of patchy colloidal dumbbells for size ratio $q = 1.035$, interaction strength $\beta\varepsilon = -3.58$ and interaction range $\Delta = 0.5\sigma_1$ in the sphere separation $l = 2d/(\sigma_1 + \sigma_2)$ -volume fraction ϕ representation. The green-shaded circles indicate the state points chosen to investigate the stability of the vesicles with respect to the bilayers.

transition from one regime to the other is fully determined by the sphere separation l : micelles are observed for small separations l when the attraction is more directional, whereas bilayers are found for large separations l , i.e., when the patchy interaction is less directional and the steric constraint by the non-interacting hard sphere of the dumbbell becomes more apparent. For intermediate separations, we find vesicles which are favoured due to a delicate balance between the directionality of the attraction and the geometric anisotropy of the particle.

For two state points, $[(l = 0.23, \phi = 0.007), (l = 0.19, \phi = 0.14)]$ we find that both bilayers and vesicles form in the simulation box. On increasing simulation time, we observe that the vesicles are not stable when the size of the cluster is well below $N_c = 90$ and that in this case they open up to become small bilayer sheets. On the contrary, if the size of the vesicles is above $N_c = 90$ they do not break up. However, as this behaviour is inferred by analysing configurations in the MC-NVT simulations, it might be interesting to check the observation with explicit free-energy calculations using grand-canonical Monte Carlo simulations of single clusters as used in Refs. [78, 105]. To understand the relevance of the observed structures, it is worth mentioning that vesicles can be employed as drug containers in drug delivery processes [119–121], while the bilayers offer the possibility of building large two-dimensional colloidal structures from very simple building blocks, which can be useful for application in photonics [122].

As we turn to size ratio $q = 1.25$ for which the state diagram is shown in Fig. 2.8, we observe that, with respect to the size ratio $q = 1.035$, the micellar region has grown at the expense of the vesicle and bilayer regime. Additionally, for small sphere separations we observe a regime

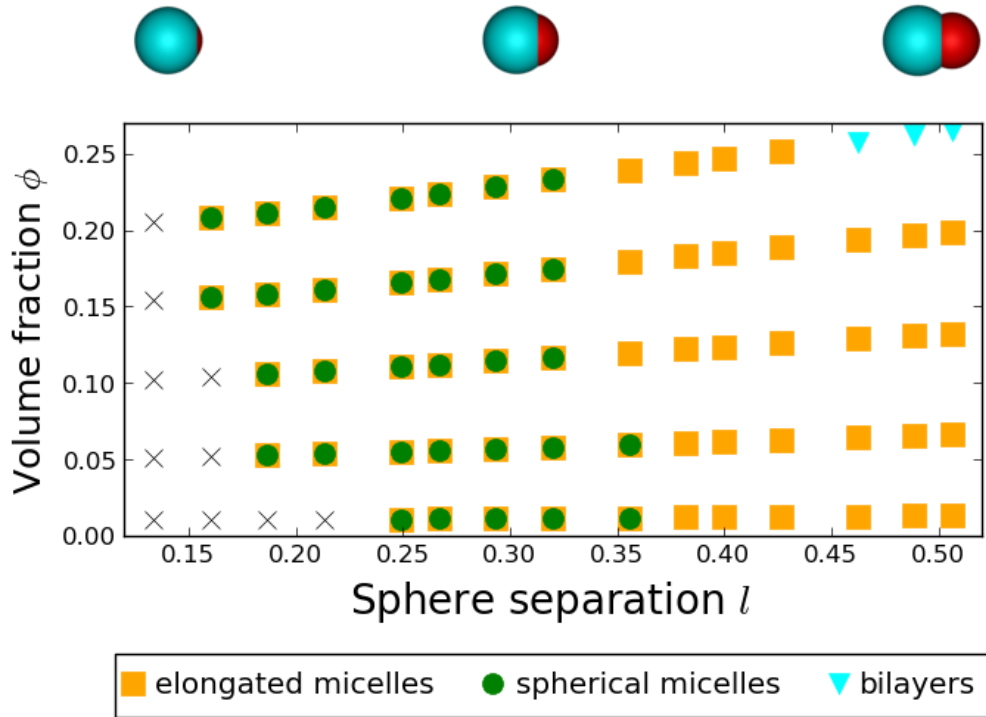


Figure 2.8: State diagram of patchy colloidal dumbbells for size ratio $q = 1.25$, interaction strength $\beta\varepsilon = -3.58$ and interaction range $\Delta = 0.5\sigma_1$ in the sphere separation $l = 2d/(\sigma_1 + \sigma_2)$ -volume fraction ϕ representation. The crosses indicate the regime where aggregation is not relevant.

where the total number of aggregated particles is smaller than the number of free monomers (denoted with crosses in the figure). The size of this regime decreases upon increasing the volume fraction. The bilayers can only be found at high volume fractions and high sphere separations. However, we do observe elongated micelles which have bilayer-like characteristics, close to the points where bilayers are observed. We additionally compute the cluster size distribution for $q = 1.25$ for different values of sphere separation l , but all at the same number density $\rho\sigma_1^3 = 0.1$ (note however that the volume slightly changes as the two spheres of the dumbbell become more separate upon increasing l). This is defined as the number n_{N_c} of clusters consisting of N_c dumbbells, divided by the box volume V . The cluster size distributions as shown in Fig. 2.9 for patchy dumbbells with a size ratio $q = 1.25$ are strongly peaked, with the peak shifting to higher cluster sizes upon increasing the sphere separation l . Indeed, in this regime where micellar clusters form, the radius of curvature of a cluster becomes larger as the particles become more elongated, in turn allowing the clusters to grow larger. It is interesting to compare our results to Ref. [115]. The size ratio here considered, $q = 1.25$, is the closest value we have to the lowest value considered in that work ($q = 1.4$), while their sphere separation in terms of $l = 2d/(\sigma_1 + \sigma_2)$ reads $l = 0.53$. For these conditions, our estimate of the average cluster size $\langle N_c \rangle$ is 30 times higher than the one in Ref. [115]. The reason for this large difference is two-fold: firstly, the size ratio considered in Ref. [115] is already 12% larger than ours, secondly – and more importantly – the interaction range considered in this work ($\Delta = 0.5\sigma_1$) is three times as large as the one considered in Ref. [115]. Indeed, when we performed simulations

with $q = 1.4$ and shorter interaction range ($\Delta = 0.15\sigma_1$) similar values were obtained for the average cluster size, being $\langle N_c \rangle \sim 9$ in this work and $\langle N_c \rangle \sim 7$ in Ref. [115].

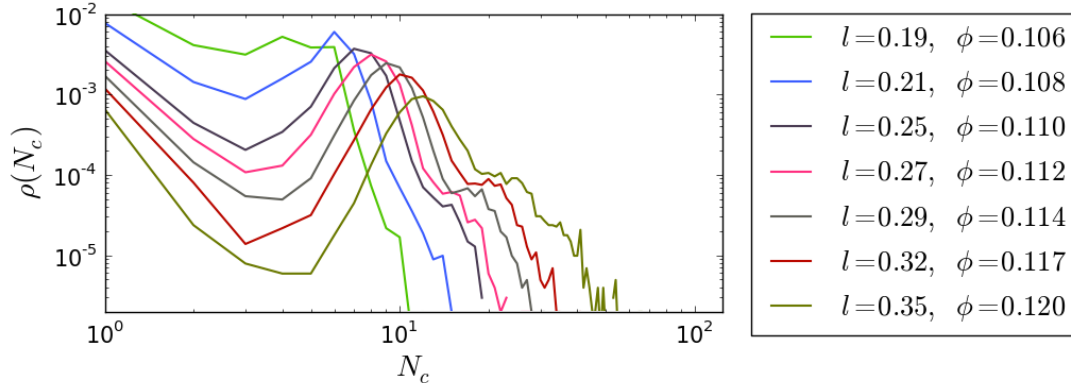


Figure 2.9: Cluster size distribution $\rho(N_c) \equiv n_{N_c}/V$ as a function of the number of particles N_c in a cluster for patchy colloidal dumbbells with size ratio $q = 1.25$, interaction strength $\beta\epsilon = -3.58$, interaction range $\Delta = 0.5\sigma_1$, and varying sphere separation l and volume fraction ϕ as labelled.

For size ratio $q = 1.035$ and $q = 1.25$, and for small values of the sphere separation l , a comparison can be made with the case of spherical patchy particles with low surface coverage [104]. In view of this context, the size ratio $q = 1.035$ and the sphere separation $l < 0.1$ would correspond to a patch surface coverage of $\chi = 0.4$. In this case, our model and the one in Ref. [104] yield the same self-assembled structures, i.e. micelles, on all the volume fractions investigated in this work.

Finally, we have also investigated patchy dumbbells with size ratio $q = \sigma_2/\sigma_1 = 0.95$, where the non-interacting hard sphere is smaller than the attractive sphere. The corresponding state diagram for different values of ϕ and l is given in Fig. 2.10. The formation of bilayers is observed for most sphere separations. For larger separations, the formation of vesicles is observed. Note that this region is located at a different range of separations with respect to the size ratio $q = 1.035$. While the size of the vesicles for size ratio $q = 0.95$ is up to 10 times larger than the one found for $q = 1.035$, both fall into the correct classification category, given by the \mathcal{V} order parameter.

Interestingly, we also observe the formation of faceted polyhedra (see Fig. 2.11), which were also found in Ref. [115, 123]. In addition, we observe the formation of liquid droplets [123] – disordered, liquid-like, aggregates of particles which is to be expected as in the limit $l \rightarrow 0$ and $q \rightarrow 1$, the system reduces to a square-well fluid at a state point that lies well-inside the two-phase gas-liquid coexistence region [124].

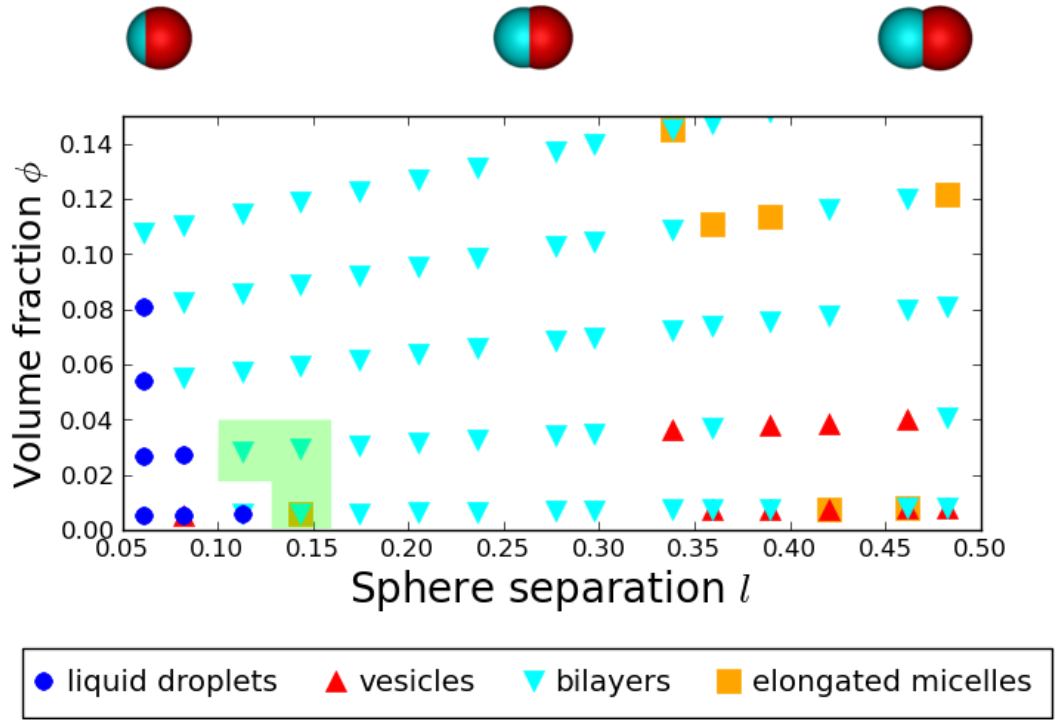


Figure 2.10: State diagram of patchy colloidal dumbbells for size ratio $q = 0.95$, interaction strength $\beta\epsilon = -3.58$ and interaction range $\Delta = 0.5\sigma_1$ in the sphere separation $l = 2d/(\sigma_1 + \sigma_2)$ -volume fraction ϕ representation. The green-shaded region signals, for the state points inside it, the presence of faceted polyhedra in addition to the reported structures. The classification of five state points in the diagram has changed due to visual inspection.

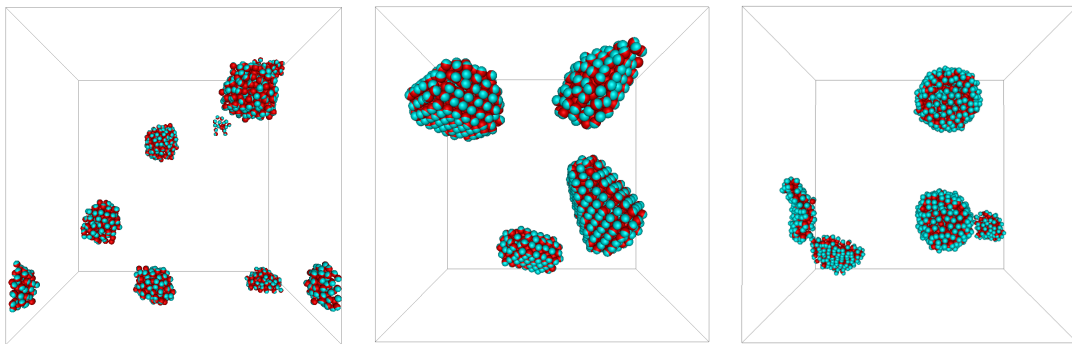


Figure 2.11: Typical final configurations for patchy colloidal dumbbells with a size ratio $q = 0.95$, interaction strength $\beta\epsilon = -3.58$, interaction range $\Delta = 0.5\sigma_1$. Left panel: Liquid droplets at packing fraction $\phi = 0.005$ and sphere separation $l = 0.06$. Middle panel: faceted polyhedra at packing fraction $\phi = 0.028$ and sphere separation $l = 0.08$. Right panel: vesicles at packing fraction $\phi = 0.008$ and sphere separation $l = 0.46$.

From the order parameter analysis, liquid droplets and faceted polyhedra look very similar. To distinguish between them, we calculate the orientation probability distribution function $P(\hat{\epsilon}_i \cdot \hat{\epsilon}_j)$, for a set of neighbouring particles i and j , all belonging to the same cluster (Fig. 2.12). While it is clear that pairs of dumbbells inside faceted polyhedra and vesicles have a strong tendency to be aligned or counter-aligned with respect to each other, the liquid droplets display a more isotropic distribution as the dumbbells are oriented more randomly with respect to each other.

Upon increasing the sphere separation, at low volume fractions, we observe a transition from liquid droplets to faceted polyhedra to bilayers that is similar to what has been reported in a previous work on amphiphilic spherical Janus colloids [123]. For small sphere separations, this comparison is justified, since here in both cases the particles are approximately spherical. However, as the sphere separation increases the shape of our dumbbells becomes very different from spheres, explaining why the vesicles are not found in Ref. [123].

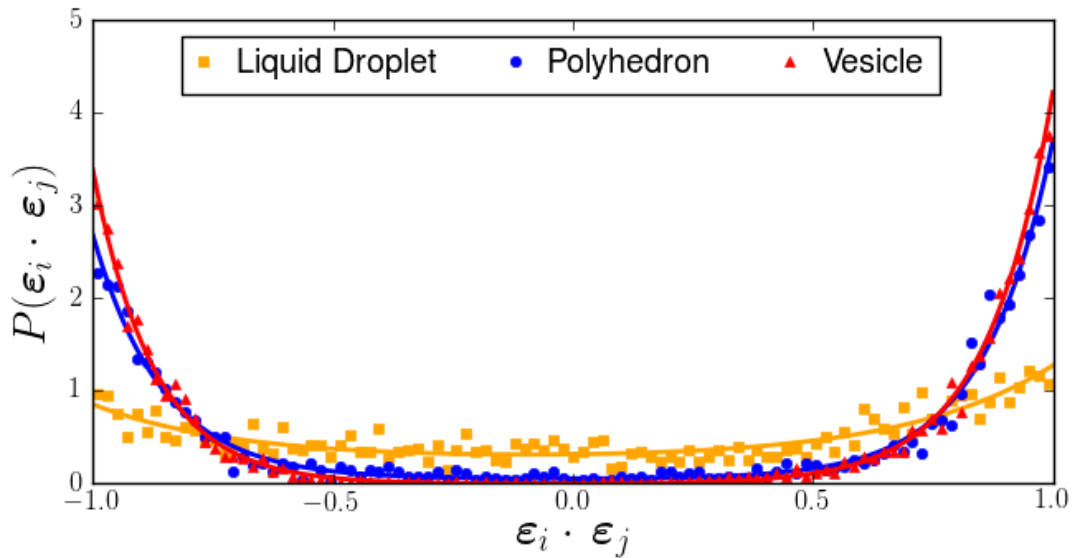


Figure 2.12: Orientation probability distribution function for the representative aggregate type: faceted polyhedron, vesicle and liquid droplet. While faceted polyhedra and vesicles show a similar degree of orientational ordering of the neighbouring particles, the disordered liquid droplets exhibit a more isotropic distribution. The solid lines are least-square fits to a double exponential function.

The comparison with the state diagrams for $q = 1.035$ and $q = 1.25$ suggests that bilayers are the most frequently encountered structures for size ratio $q = 0.95$. For size ratio $q = 1.035$ the bilayers already become less dominant at larger sphere separations, at the cost of other structures such as vesicles and spherical micelles. For size ratio $q = 1.25$ the bilayers are only present in a small range of volume fractions, leaving more room for the formation of elongated and spherical micelles.

2.4 Conclusions

We have performed Monte Carlo simulations on patchy colloidal dumbbells consisting of one hard attractive sphere and one hard non-interacting sphere. To model the patchy interactions between the attractive spheres, we have extended the Kern-Frenkel potential to the case of non-spherical particles. In particular, we have investigated the effect of varying the size ratio $q = \sigma_2/\sigma_1$ between the two hard spheres of the dumbbell, and the distance between them, characterised by the sphere separation l . Starting from a fluid, we have observed the formation of spherical and elongated micelles, vesicles and bilayers. In order to compare the outcome of the simulations for our entire parameter space, we employ order parameters to identify and distinguish the clusters inside the simulation box.

To summarise, we have investigated the effect of changing the sphere separation l for three different size ratios $q = 1.035$, $q = 1.25$ and $q = 0.95$, and for volume fractions ranging between 0 and 0.25.

For size ratio $q = 1.035$ we have observed the largest variety of structures. While micelles form for small sphere separations, and bilayers for high sphere separations, the formation of vesicles is limited to a very limited region of sphere separations. We speculate that this is due to a balance between interaction directionality and particle geometry and it would be interesting to study this further using free-energy calculations.

For size ratio $q = 1.25$, upon increasing the sphere separation l , the structures change from spherical micelles to elongated micelles, and ultimately - at sufficiently high volume fractions - to bilayers. In this case, no vesicle formation was observed, suggesting that the system is sensitive to small changes in particle geometry.

Finally, for the last investigated case, where the size ratio $q = 0.95$, we found bilayer formation on a wide range of sphere separations and volume fractions. We also found hollow structures such as vesicles and faceted polyhedra and occasionally droplet-like structures where the particles are clustered together with random particle orientations. Comparison with the state diagrams for $q = 1.035$ and $q = 1.25$ suggests that the size ratio is an important factor in stabilising the bilayers with respect to vesicles and micelles.

In another paper on patchy Janus particles [123] a transition is reported in simulations from liquid droplets to faceted polyhedra to bilayers, which is similar to what we observe for size ratio $q = 0.95$ and small sphere separations, while Ref. [115] gives an estimate for the average cluster size consistent with ours, once we use similar geometric and interaction parameters.

This chapter illustrates how a variety of different structures, some of them particularly relevant for applications [122, 125–127] such as hollow vesicles and bilayers, can be formed starting from patchy dumbbells with attractive interactions. The work also shows that many of these structures can be well characterised using cluster order parameters. It also suggests that in experiments the structures might be very sensitive to variations in particle geometry, which is the case in for example, polydisperse systems. In particular, this information is useful when designing particles that can form hollow vesicles that can be useful in drug delivery or colloidal surfactants. It would be interesting to perform a more detailed study focusing on this topic, ideally combined with experiments. Finally, in this chapter we have focused on relatively low volume fractions where no crystallisation takes place. The formation of crystals, some of which might have interesting photonic properties, could also be topic of a follow-up study.

Acknowledgements

It is a pleasure to thank Teun Vissers for both the collaboration on this project and the fundamental discussions at the pub.

Self-assembly of “Mickey Mouse” shaped colloids into tube-like structures

The self-assembly of anisotropic patchy particles with triangular shape was studied by computer simulations and compared to experiments. The colloidal particles consist of a central smooth lobe connected to two rough lobes at an angle of $\sim 90^\circ$, resembling the shape of a “Mickey Mouse” head. Due to the difference in overlap volume, adding an appropriate depletant induces an attractive interaction between the smooth lobes of the colloids only, while the two rough lobes act as steric constraints.

The essentially planar geometry of the “Mickey Mouse” particles is a first geometric deviation of dumbbell shaped patchy particles. This new geometry is expected to form one-dimensional tube-like structures rather than spherical, essentially zero-dimensional micelles. At sufficiently strong attractions, we indeed find tube-like structures with the sticky lobes at the core and the non-sticky lobes pointing out as steric constraints that limit the growth to one direction, providing the tubes with a well-defined diameter but variable length both in experiments and simulations. In the simulations, we found that the internal structure of the tubular fragments could either be straight or twisted into so-called Bernal spirals.

3.1 Introduction

The geometry of a self-assembled object is expected to depend on the shape and specific interactions of the individual building blocks [128, 129]. This is seen for instance in systems of surfactants, where the geometry of the surfactant molecules determines the geometry of the micelles they form [130]. Similarly, conical dendrons are found to form spherical supramolecular dendrimers, whereas flat, tapered dendrons form cylindrical dendrimers [131]. By changing the shape-anisotropy of the colloidal building blocks with attractive and non-attractive patches, we can tune the directionality of the interactions for colloidal self-assembly. In this chapter, we investigate the self-assembly of colloidal building blocks consisting of one sticky and two non-sticky lobes in a triangular conformation. Since the second non-sticky lobe provides our particles with a planar rather than conical geometry, we expect these particles to induce the formation of cylindrical aggregates.

There are several ways to introduce specific interactions to colloidal particles. Spherical particles with a single attractive patch, also called Janus particles, can be made by templated surface modification [132, 133] and have been found to form small clusters and chain-like aggregates [132, 134]. This synthesis method can be extended to multiblock particles, introducing additional attractive patches [135], allowing for the formation of for instance Kagome lattices in 2D upon sedimentation [136]. Another way to introduce attractive patches to spherical colloids is by making use of complementary strands of DNA. This method was employed by Pine and co-workers [137] in a multi-step synthesis method to create particles with up to four well-defined sticky patches, mimicking molecular bonds and forming the colloidal equivalent of molecules. Since these systems are based on spherical particles, self-assembly is based on the topology of attractive patches on the particles and not on the particle shape.

In addition to changing the topology of attractive patches on the surface, interaction can also be made directional by altering the shape of the particle such that it becomes non-spherical. A good example of this shape-anisotropy are dumbbell-shaped colloids that can be used as building blocks for colloidal self-assembly. Such particles can be produced in bulk by forming a protrusion on a polymer seed particle using seeded emulsion polymerization [138–143] and if the two sides of such a particle are chemically different [140, 142–144], this difference can be used to induce specific interactions to either lobe of the dumbbell.

Because it is easier to tune the shape and interaction of particles in simulations, a lot of exploratory simulation work on the self-assembly behaviour of patchy dumbbell and Janus particles has already preceded the experiments, finding finite sized micelle-like clusters [145–148] and vesicles, tubular, lamellar and crystalline equilibrium phases [149–154]. However, even if such particles can be synthesized, their specific interactions are usually short-ranged and strong, so not all structures predicted by simulations can be achieved experimentally.

Recently, Kraft *et al.* [155] introduced specific interactions in a system of asymmetric dumbbells by site-specific surface roughness. Upon addition of a depletant, only the smaller smooth lobe of the particle became attractive, which resulted in finite sized, spherical micelle-like clusters.

In this chapter, we present a simulation study on the so-called “Mickey Mouse” (MM). These particles consist of a smooth lobe that becomes attractive in the presence of a depletant and two rough lobes, at an angle close to 90° , that remain non-attractive (Fig. 3.1). These two non-attractive lobes provide the particles with a planar geometry and give directionality to

the attractions between the smooth lobes in such a way that they are expected to form long, one-dimensional tube-like structures that rarely branch.

To investigate the effect of particle concentration and interaction strength on the resulting structures, we use Monte Carlo computer simulations. From this study, it becomes clear that the unique geometry of the particles indeed causes the formation of elongated tube-like structures with a well-defined diameter. Our simulation results agree well with the experimental observations reported in Ref. [79]. However, from the experiments it also becomes clear that the sticky nature of the interaction also seem to prevent the system from converging to its ground state.

3.2 Model and methods

In the computer simulations, only the essential features of the experimental system as studied in Ref. [79] were modelled. This allows us to retain the essential physics, but disregard all the obvious complications of the experimental system. In particular, the particle geometry and the particle-particle interaction are the main features in our computational study. Fig. 3.1 shows the model of an MM particle geometry and interaction, together with an SEM picture of the actual particles used in the experiments of Ref. [79].

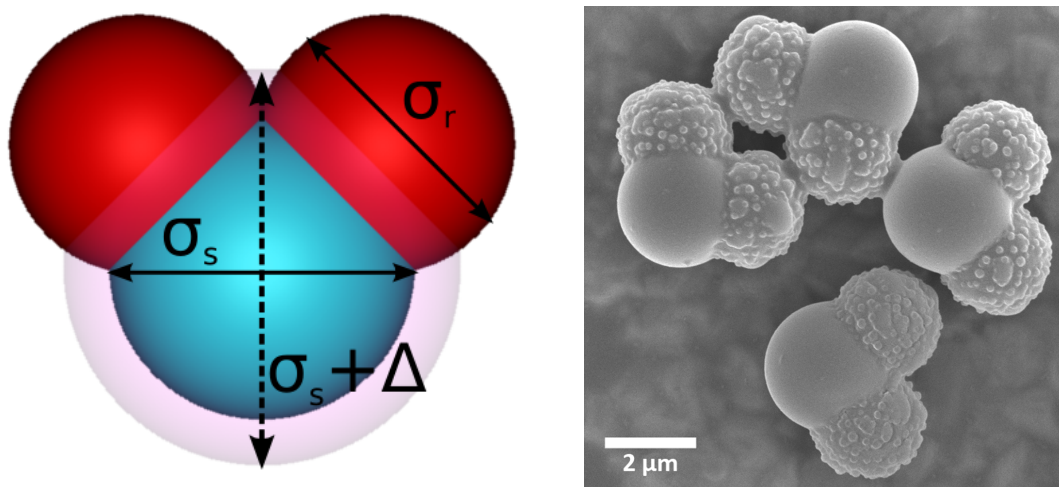


Figure 3.1: (left) Model of an MM particle: the smooth lobe is represented by a hard sphere of diameter σ_s , the two rough lobes are represented by hard spheres of diameter σ_r . The interaction between the smooth lobes of two different MM particles is modelled by a square-well potential of range Δ . (right) SEM micrograph of the isolated MM particles.

In the simulations, an MM particle is represented by an aggregate of three spheres, one central sphere with diameter σ_s which represents the smooth lobe, and on either side of it two smaller spheres with diameter σ_r mimicking the rough lobes. The depletion attraction between two smooth lobes i and j of two different MM particles is described by a square-well interaction,

$$u^{\text{SW}}(r_{ij}) = \begin{cases} \infty & \text{if } r_{ij} < \sigma_s \\ \varepsilon & \text{if } \sigma_s < r_{ij} < \sigma_s + \Delta \\ 0 & \text{if } r_{ij} > \sigma_s + \Delta \end{cases}, \quad (3.1)$$

where $\varepsilon < 0$ denotes the depth of the well, and $\Delta = 0.02\sigma_s$ is the range of the interaction. The rough lobes of the particles were treated as non-overlapping hard bodies, where the interaction between two rough lobes k and m of two different particles is described with a hard-sphere potential,

$$u^{\text{HS}}(r_{km}) = \begin{cases} \infty & \text{if } r_{km} < \sigma_r \\ 0 & \text{if } r_{km} > \sigma_r \end{cases} . \quad (3.2)$$

Note that, in spite of using a spherically symmetric potential for the attractions, the total particle-particle interaction is not invariant under rotations, due to the steric constraint of the rough lobes.

We performed Monte Carlo (MC) simulations in the canonical ensemble (MC-*NVT*) with $N = 256$ or $N = 1024$ MM particles in a volume V and a temperature T , employing single particle translations and rotations [90] to explore the configurational phase space. The simulations were $1 - 7 \times 10^8$ MC steps long, where a single Monte Carlo step is defined as N attempted moves (either translations or rotations). In order to speed up the simulations, we have also devised cluster moves, where a cluster of particles is first identified and then displaced. This cluster move is somewhat simpler than the geometric cluster move discussed in Refs. [156, 157], and it is expected to fail for intermediate to high densities. However, for the purpose of our investigation, we did not encounter such a difficulty.

We investigated the effect of varying the packing fraction $\phi = \rho v_{\text{MM}}$ (where $\rho = N/V$ and v_{MM} is the volume of a single particle) and the interaction energy $\beta\varepsilon$ (here $\beta = 1/k_{\text{B}}T$ denotes the inverse temperature with k_{B} Boltzmann's constant and T the temperature), while the other parameters in the model were fixed to match the experimental system as closely as possible. The simulation results are analysed using a cluster analysis. For this, MM particles are identified as interacting neighbours that have at least one mutual bond, i.e. the distance between their attractive lobes is less than the square-well interaction range. Subsequently, a cluster is defined as a contiguous set of neighbouring particles. The cluster analysis allows us to compute for each interaction strength the concentration of free particles in the system, as well as the number of bonds per particle in the clusters.

3.3 Results and discussion

In the following section, we present the results obtained from simulations which we then compare to the experiments performed in Ref. [79].

3.3.1 Self-assembly of clusters and tubes

The simulations in the *NVT* ensemble run for at least 10^8 MC steps up to seven times as much. Note that the maximum translational and rotational displacements are kept fixed from the beginning, and not adjusted to yield a preset acceptance rate. We fix the square-well width to the short range value of $\Delta = 0.02\sigma_s$, because of the short ranged attraction achieved in the experiments of Ref. [79]. We investigate four different packing fractions, namely $\phi_{\text{particles}} = 0.007, 0.01, 0.014, 0.018$. For each packing fraction, we vary the square-well depth ε between $-3.0k_{\text{B}}T$ and $-12.0k_{\text{B}}T$ in steps of $-0.5k_{\text{B}}T$. During the simulations, we monitor the mean energy per

particle, which immediately gives us information on the degree of self-assembly in the system, while we obtain the probability of observing a cluster with N_c particles during post-processing.

The evolution of the mean energy per particle against the number of Monte Carlo Steps (MCS), shown in Fig. 3.2 a representative packing fraction $\phi_{\text{particles}} = 0.01$, displays a characteristic sigmoidal shape, with a decreasingly marked plateau as the square-well interaction becomes more attractive. Based on the behaviour of the internal energy of the system, as well

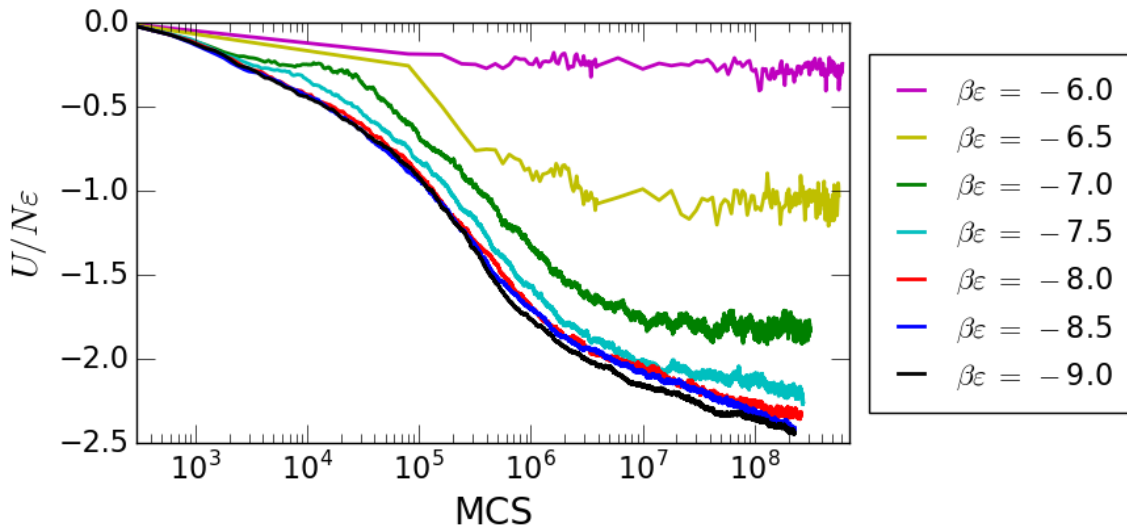


Figure 3.2: Behaviour of the mean energy per particle $U/N\epsilon$ as function of the Monte Carlo Steps (MCS) for packing fraction $\phi_{\text{particles}} = 0.01$.

as on the visual inspection of the final configurations of the system, we can roughly divide the simulation results in three broad categories:

1. **Gas of MM particles.** For interaction strengths $\beta\epsilon \in [-3.5, -6.0]$, the MM particles show no or little self-assembly, and the internal energy of the system is less than $-0.5k_B T$.
2. **Cluster phase.** For interaction strengths $\beta\epsilon = -6.5, -7.0$, and -7.5 the MM particles form a stable cluster phase in equilibrium with a gas of MM particles. In this particular phase, the internal energy of the system gives results between $-1.0k_B T$ and $-2.0k_B T$, depending on the interaction strength.
3. **Formation of tube-like structures.** When the attraction between particles crosses $\beta\epsilon = -8.0$ or lower, we observe the spontaneous self-assembly of elongated, tube-like structures, at which we will look more carefully in the next sections.

In Fig. 3.3, by using the snapshots of the final configurations, we present a visual summary of the behaviour of the system for increasing interparticle attraction. We will see that the experimental realisation of this system shows a similar kind of behaviour.

It is interesting to look at the effects of interaction strength and packing fraction on the probability of finding a cluster with N_c particles, as shown in Fig. 3.4. On the left panel, we see that the cluster size distribution develops a peak around $N_c \sim 10$ upon increasing the attraction strength. We also see that the peak develops starting from $\beta\epsilon = -6.5$ and above this strength,

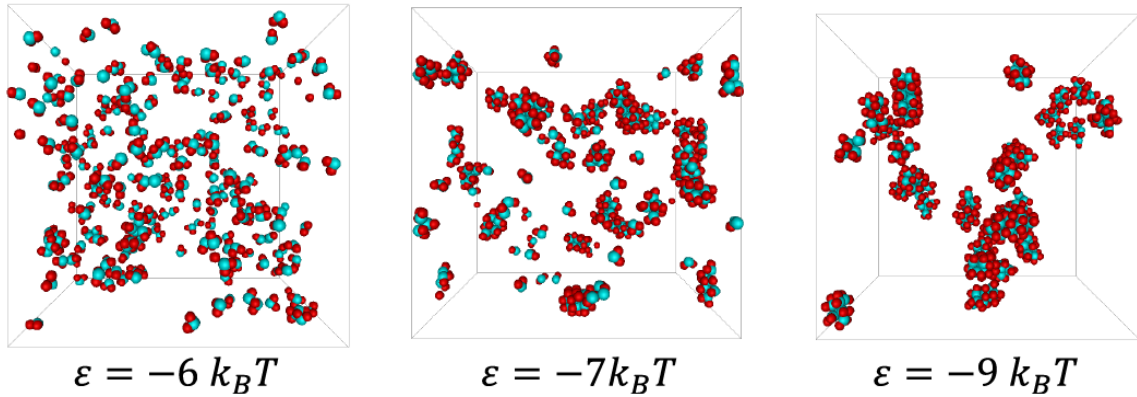


Figure 3.3: Behaviour of the system, for a fixed, representative packing fraction of $\phi_{\text{particles}} = 0.01$, with increasing interaction strength. We observe the self-assembly of clusters around $\beta\varepsilon = -7.0$ and of tube-like structures for $\beta\varepsilon < -8.0$.

the system is in a gas-like state. On the right panel, we observe that the packing fraction does not have a large influence on the self-assembly of the system, as the main peak of the distribution is not shifted towards higher values.

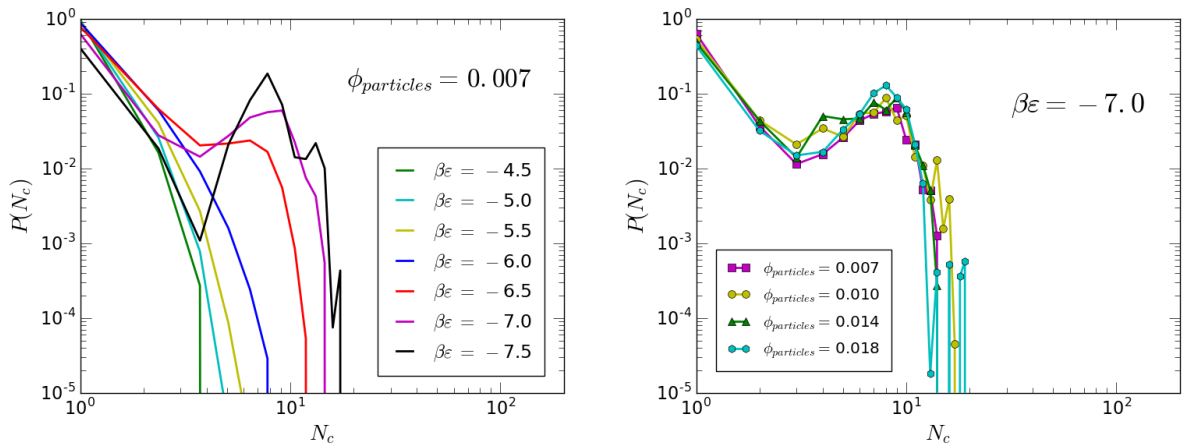


Figure 3.4: Probability distribution function $P(N_c)$ of observing a cluster with N_c MM particles. (left) At a fixed packing fraction $\phi_{\text{particles}} = 0.007$, a peak develops in $P(N_c)$ around $N_c \sim 10$. (right) The position of the main peak in $P(N_c)$ is not affected by the different packing fraction investigated.

The cluster size distribution of the system also undergoes changes when we enter the region where tubes start forming. In particular, from Fig. 3.5, not only the main peak is broader, including sizes up to $N_c \sim 30$, but we also find a significant fraction of clusters as large as $N_c \sim 40$. Moreover, the fraction of free MM particles drastically reduces going from $\beta\varepsilon = -7.0$ (clusters) to $\beta\varepsilon = -9.0$ (tubes).

The average number of bonds per particle $\langle n \rangle$ was also calculated for all the different packing fractions and interaction strengths investigated, and is shown in Fig. 3.6. Two things are particularly interesting here: firstly, we see how sharp is the transition from the gas of MM particles, with less than a bond per particle (for $\beta\varepsilon \in [-3.5, -6.0]$), to tube like structures, starting at $\beta\varepsilon = -8.0$. The self-assembly of the system happens in a narrow window of $\sim 2.0k_B T$. In

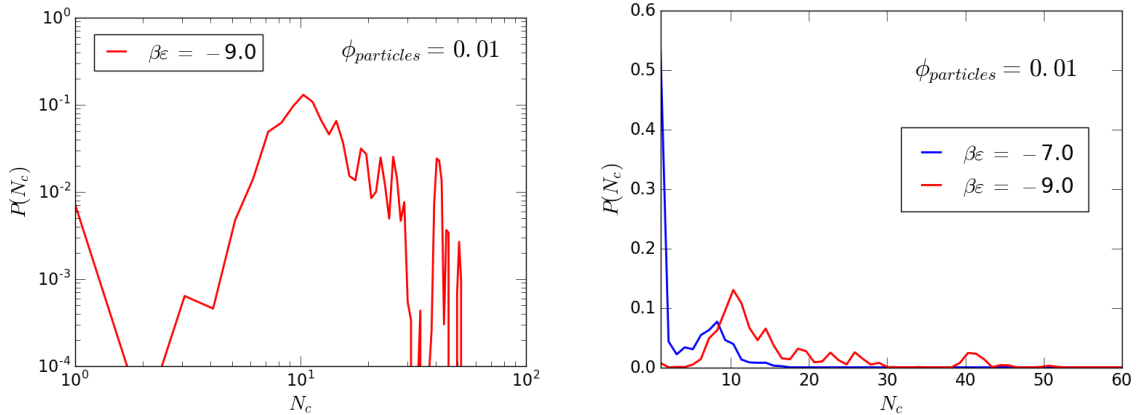


Figure 3.5: Probability distribution function $P(N_c)$ of observing a cluster with N_c MM particles. (left) At a fixed packing fraction $\phi_{\text{particles}} = 0.01$ and for an interaction strength of $\beta\epsilon = -9.0$, the distribution presents a large main peak, including sizes up to $N_c \sim 30$, and a second peak at $N_c \sim 40$. (right) In comparison to the case of cluster formation, significantly larger cluster sizes come into play, and the fraction of free monomers decreases.

between these two cases, we find the stable cluster phase, characterised by intermediate values of the number of bonds per particle. Secondly, once the tube structures are formed, increasing further the attraction between particles does not lead to an increase of number of bonds per particle, which levels off at a value of $\langle n \rangle \sim 5$. Moreover, the behaviour is conserved across the different packing fractions investigated in this work.

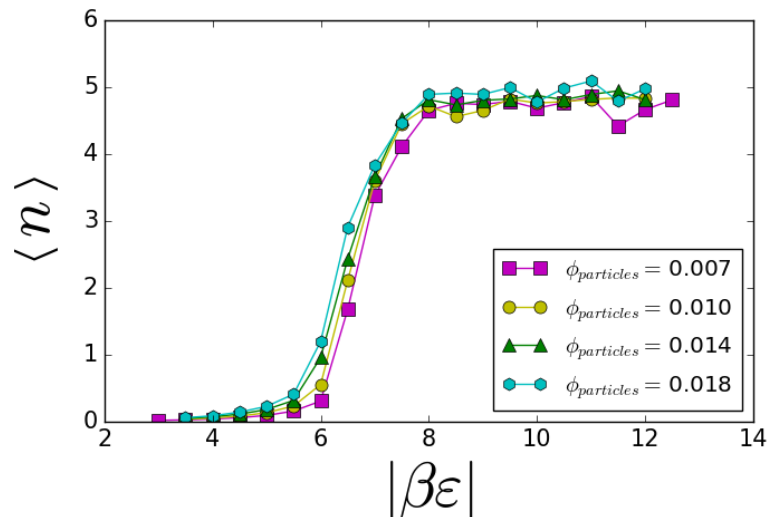


Figure 3.6: Average number of bonds per particle $\langle n \rangle$ as function of the absolute interaction strength $|\beta\epsilon|$. The transition between the gas of MM particles and the tube-like structures is found to be rather sharp, taking place on a range of just $\sim 2.0k_B T$. We find that $\langle n \rangle \sim 5$ for the tube structures.

3.3.2 Tube morphology

From the final configurations in the computer simulations, we analysed the structure of the tube-like clusters in more detail. We found that the particles can be stacked in two different ways, resulting either in straight or spiral-like tube structures. Both of these structures occur next to each other in the simulation box, and we even found tubes that were partially made up of one structure and partially of the other one.

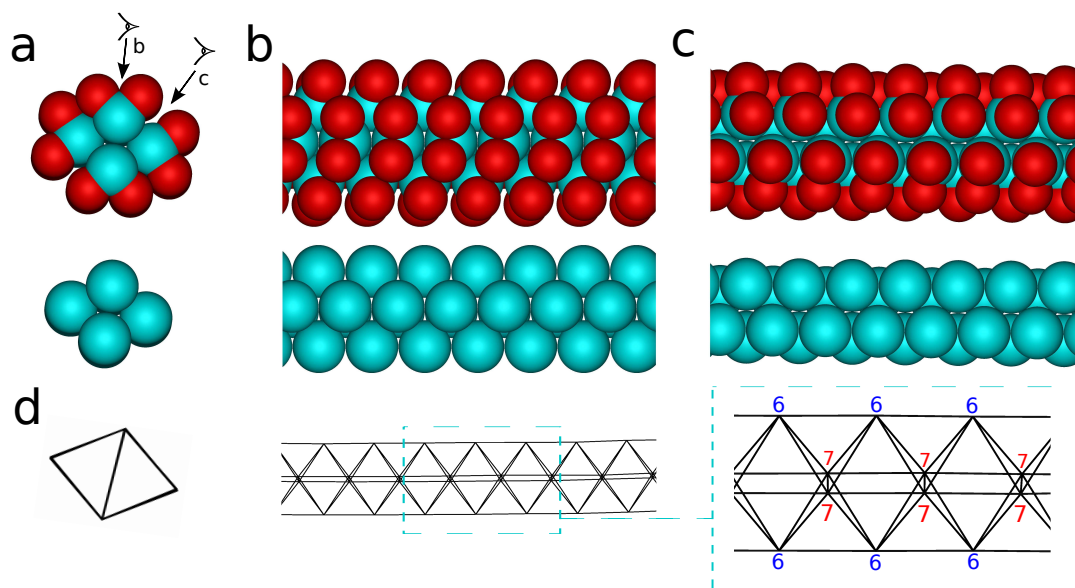


Figure 3.7: Straight tubular structure with the lowest binding energy found in computer simulations. The smooth lobes are shown in blue, the steric ears are shown in red. (a:) top-view showing the Mickey Mouse particles (b-c:) side-views as seen from the directions denoted in (a) (d:) representation of the structure showing the bonds between the MM particles as sticks, for the same viewing angles as in (a) and (b). The mickey mouse particles are located at the vertexes. The numbers denote the number of connections for each vertex.

An example of a straight tube-like structure is shown in Fig. 3.7a-c. For each viewing angle, the entire MM particles or only the smooth lobes are shown. The smooth lobes on the inside form a closely packed backbone, whereas the steric ears are all located on the outside and shield the backbone, thus preventing branching of the structure. In Fig. 3.7d the bonds between the smooth spheres of the MM particles are depicted as sticks. It can be seen that the bonds form a framework of octahedrons with tetrahedrons in between. The MM particles located at the vertexes of the square of the octahedron form 7 bonds with surrounding particles, whereas the particles on the top ends of the octahedrons are connected with 6 bonds, making up for an average of 6.5 bonds per particle. In addition to the *NVT* simulations, we performed Monte Carlo simulations in which a small number of MM particles was compressed in a rectangular box whose 3 lattice vectors were free to change independently. From this, it appeared that the straight tube is the ground state structure with the maximum number of bonds per particle.

In addition to straight tubes, the MM particles can also be stacked in a spiral-like fashion, as is shown in Fig. 3.8. In Fig. 3.8a-b, top and side views of a spiral observed in computer simulations are shown. The framework of bonds making up the structure is shown in Fig. 3.8c,

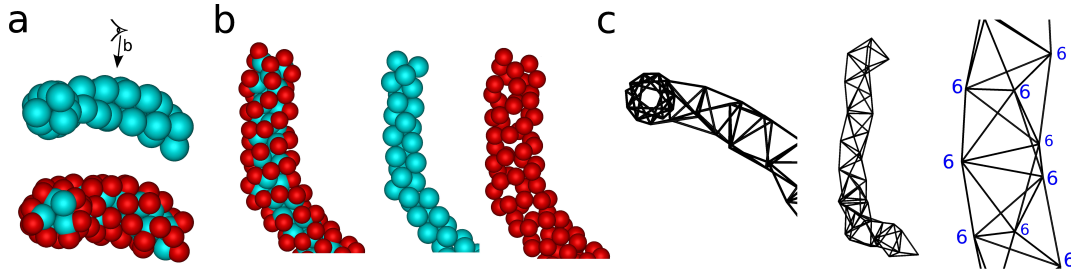


Figure 3.8: Tubes with the structure of a Bernal spiral found in computer simulations. The smooth lobes are shown in blue, the steric ears are shown in red. (a:) top-view showing the Mickey Mouse particles (b:) side-views as seen from the directions denoted in (a) (c:) representation of the structure showing the bonds between the MM particles as sticks, for the same viewing angles as in (a) and (b). The mickey mouse particles are located at the vertexes. The numbers denote the number of connections for each vertex.

revealing a repeated structure of connected face-sharing tetrahedra also known as a Bernal spiral [158] or Boerdijk-Coxeter helix [159, 160]. In a perfect spiral, each particle is bound to six neighbours. Bernal spirals were already found for colloidal systems with short-ranged attractions and screened electrostatic repulsion [161, 162] but recently also for Janus particles that are able to undergo directional interactions [163]. Recent efforts have focused on creating Bernal spirals by design with patchy particles [164, 165]. However, in either case the potential or the positions, size and shape of the patches needs to be carefully tuned. In our case, the spiral forms mainly for geometric reasons, illustrating that the steric ears on the MM particles constitute a robust way of creating functional directional interactions. In addition, the ears also protect the attractive backbone of the spiral from sideways attachments and thus provides a new possible way to produce core-shell tubular structures by self-assembly.

3.4 Comparison with experiments

In the following section, we compare the results obtained from the simulations to the experiments of Ref. [79]. Since a key factor in comparing the results is the evaluation of the interaction strength in the experiments, we first discuss briefly how this is done, then we move to the self-assembly results.

In the experiments, the attractive interactions between the smooth lobes of the particles as function of their center-to-center separation r_{ij} results from an attractive depletion interaction and a repulsive electrostatic interaction:

$$w(r_{ij}) = w_{el}(r_{ij}) + w_{depl}(r_{ij}) \quad (3.3)$$

Here, the electrostatic repulsion (in units of $k_B T$) can be described as [166]:

$$w_{el}(r_{ij})/k_B T = \frac{(\Psi/k_B T)^2 R_s^2}{\lambda_B r_{ij}} e^{-\kappa(r_{ij}-2R_s)} \quad (3.4)$$

where $\Psi = e\zeta$ is the zeta potential times the elementary charge [167], R_s is the radius of the smooth lobe of the particle, λ_B is the Bjerrum length and κ is the inverse Debye length.

The depletion attraction between two spheres, for $2R_s < r_{ij} < 2(R_s + r_g)$ can be written as [168–170]:

$$w_{depl}(r_{ij})/k_B T = -\phi_d \left(\frac{R_s + r_g}{r_g} \right)^3 \left(1 - \frac{3}{4} \frac{r_{ij}}{R_s + r_g} + \frac{1}{16} \left(\frac{r_{ij}}{R_s + r_g} \right)^3 \right) \quad (3.5)$$

where r_g is the radius of gyration of the depletant polymer and ϕ_d is the depletant volume fraction, as fraction of the overlap concentration. Using typical experimental values for R_s ,

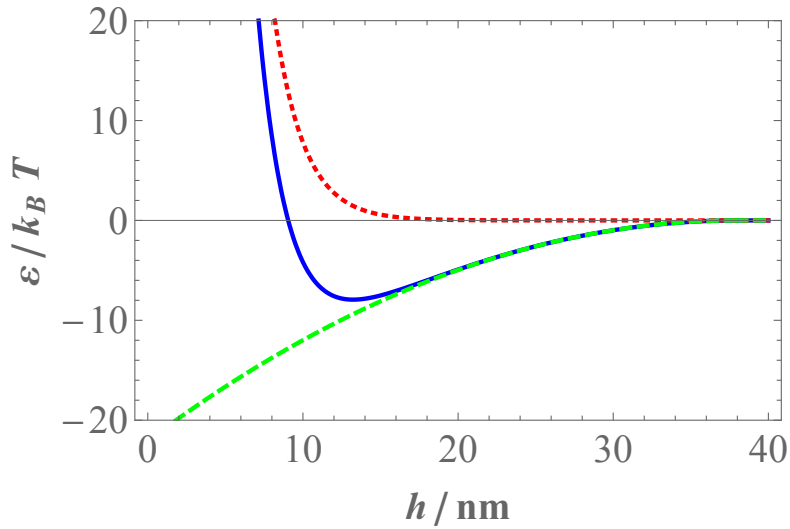


Figure 3.9: Interaction potential in $k_B T$ between the smooth lobes of the particles as function of the inter particle distance $h = r_{ij} - 2R_s$ without considering the presence or orientation of the rough lobes. The net interaction (Eq. 3.3, solid blue line) is the sum of the screened coulomb repulsion (Eq. 3.4, red dotted line) and the depletion attraction (Eq. 3.5, dashed green line). Typical experimental parameters were used to construct this graph, resulting in a depth of the potential well ε of about $-8 k_B T$ and an interaction range of 40 nm.

ϕ_d , r_g , κ , and Ψ , we find that the minimum of the potential in Eq. 3.3 varies in the range of $-7 k_B T$ to $-17 k_B T$ for a depletant volume fraction ϕ_d of 0.20 to 0.40, which is the range of experimentally used values.

The square-well attractions (Eq. 3.1) in the simulations and the experimental potential (Eq. 3.3 and Fig. 3.9), have a different shape, but a comparable range ($\Delta = 0.02\sigma_s$ corresponds to 55 nm in the experimental system) which is small with respect to the particle diameter. According to the Noro-Frenkel law of corresponding states [171, 172], short-ranged potentials give similar phase behaviour if their second virial coefficients are similar. Using Eq. 3.3 for the experimental potential and Eq. 3.1 for the square-well attractions in the simulations gives similar values of $B_2 = -2.3 \cdot 10^{11} \text{ nm}^3$ and $-2.4 \cdot 10^{11} \text{ nm}^3$ for a depletant concentration $\phi_d = 0.20$ and a square-well attraction of $\varepsilon = -7k_B T$ respectively. Therefore, we can approximate the effective pair interaction with a square-well attraction in simulations, even though the shape of the potentials is quite different.

Based on the size of the roughness ($r \approx 70 \text{ nm}$) and the much smaller radius of gyration of the depletant, only a negligible attraction between the rough lobes of the particles is expected [155]. However, at depletant volume fractions above $\phi_d = 0.33$, aspecific interactions

(rough-smooth and rough-rough) became prevalent in the experiments; at such high concentrations of depletant even the small overlap volume between rough surfaces was sufficient to cause a net attraction. Therefore, the interactions between MM particles can be considered specific up to $\phi_d = 0.33$. Since this depletant concentration corresponds to $\varepsilon \approx -14 k_B T$, the ears of the particles can indeed safely be considered as hard objects throughout the whole range of the simulations from $\varepsilon = -4 k_B T$ to $-12 k_B T$.

3.4.1 Self-assembly behaviour

The experiments were performed with two different particle concentrations, namely $\phi_{\text{particles}} = 0.003$ and $\phi_{\text{particles}} = 0.01$.

For the samples with $\phi_{\text{particles}} = 0.003$, cluster formation was only observed for $\phi_d > 0.32$, corresponding to $\varepsilon \approx -13 k_B T$. At this particle volume fraction, primarily small clusters were formed. In computer simulations, we observed that the small clusters can grow out into longer, well-defined structures at all the investigated concentrations, once the interparticle attraction becomes lower than $\beta\varepsilon = -8$. Specific checks with simulations at $\phi_{\text{particles}} = 0.003$ confirmed this observation. However, in the experiments at $\phi_{\text{particles}} = 0.003$, cluster growth seemed inhibited due to the rapid depletion of free particles.

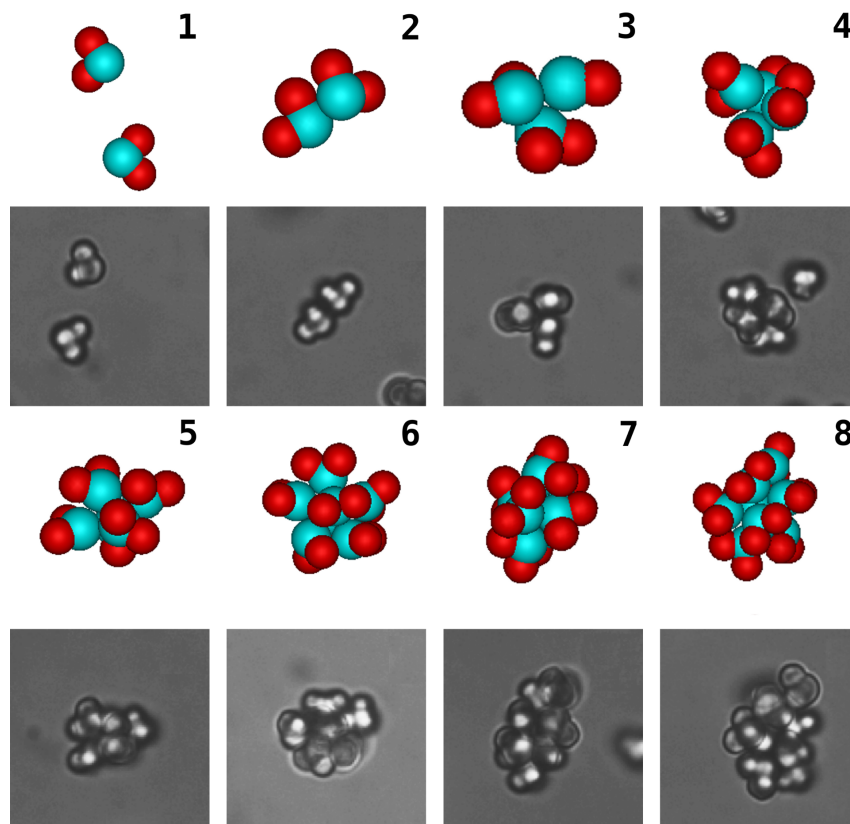


Figure 3.10: Snapshots of clusters of different sizes found in the Monte Carlo simulations compared to optical micrographs of similar clusters found at particle concentration $\phi_{\text{particles}} = 0.003$. In the simulation snapshots, the smooth (attractive) and rough (repulsive) sides are colored blue and red, respectively.

The small clusters and their structure can be investigated reasonably well using optical microscopy. Fig. 3.10 shows snapshots of typical clusters of 1 to 8 particles found in simulations next to similarly shaped clusters found in the experiments. It is clear how, also in the experiments, the particles specifically stick with their smooth sides together. The figure also shows that as clusters get larger, the positions and orientations of the individual particles become harder to observe under optical microscopy.

For the samples with $\phi_{\text{particles}} = 0.01$, it was found that a lower depletant concentration as compared to the case of $\phi_{\text{particles}} = 0.003$, indicating a lower attractive interaction potential, was required to form clusters, and that larger structures were formed. For comparison, optical micrographs from the experiments and snapshots from computer simulations at $\phi_{\text{particles}} = 0.01$ are shown in Fig. 3.11 for different attraction strengths.

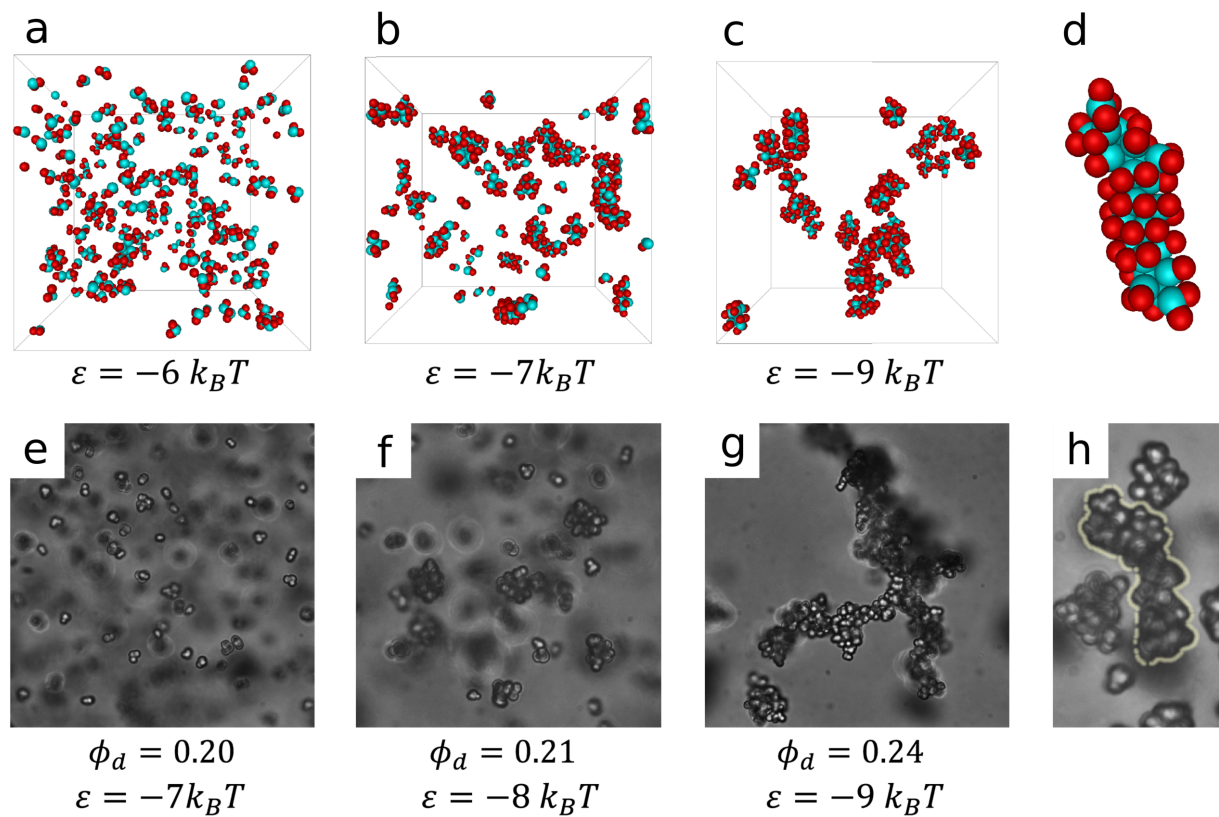


Figure 3.11: (a to c:) Optical micrographs of structures found in samples with volume fraction $\phi_{\text{particles}} = 0.01$ for a depletant volume fraction ϕ_d of 0.20 to 0.24, corresponding to an attractive interaction potential ε of $-7 k_B T$ to $-9 k_B T$. (e to g:) The MC-simulations at $\phi_{\text{particles}} = 0.01$ show the same resulting structures at comparable values of ε . (d and h:) Close-ups of comparable tube-like clusters from experiments (highlighted) and simulations, respectively.

Upon increasing the attractions, a trend can be observed from first small clusters and free single particles (Fig. 3.11.a and e), to larger clusters (Fig. 3.11.b and f), and finally tube-like structures (Fig. 3.11.c and g). The larger clusters seem to grow in only one dimension, resulting in tube-like structures with a well-defined diameter that grow seemingly unbounded in length and in random directions. A close-up of a single representative tube-like cluster from

experiments and simulations is provided in Fig. 3.11.d and h respectively. In the experiments, structures were found to branch occasionally (Fig. 3.11.c).

The shape of these structures can be attributed to the properties of the building blocks. While the attractive lobes of the particles attract each other and form the backbone of the tube-like structures, the rough lobes act as a steric constraint, preventing bond formation and structure growth on two sides of each particle at an angle of 90° . This means that if 3 or 4 building blocks are in a planar configuration, new particles can only attach from the two out of plane directions, i.e. either from below or above, promoting the growth of tubular-shaped aggregates.

In the experiments, the 8-particle cluster in Fig. 3.10 and the clusters in Fig. 3.11 show that for increasing cluster size, the scattering caused by the large refractive index mismatch between polystyrene and water ($\Delta n_D = 0.2592$) makes it more and more difficult to assess the internal structure using optical microscopy. What can be determined, however, is the diameter of the observed tubes. Fig. 3.12 shows a narrow distribution of cluster diameters. A Gaussian fit made to this distribution ($\mu = 8 \mu\text{m}$, $\sigma = 2 \mu\text{m}$) corresponds well to the diameters of the tubular structures (7 to 9 μm) found in the simulations (Fig. 3.11.h, Fig. 3.7 and Fig. 3.8, see also the insets in Fig. 3.12). The additional spread is caused by the random orientation of the rough lobes, which can make a difference of 1 μm , depending on whether one lobe ($R_r = 1.17 \mu\text{m}$) is oriented perpendicular to the tube or both are turned out of plane. The tail on the right side of the distribution can be explained by the presence of branch points, which have a larger diameter.

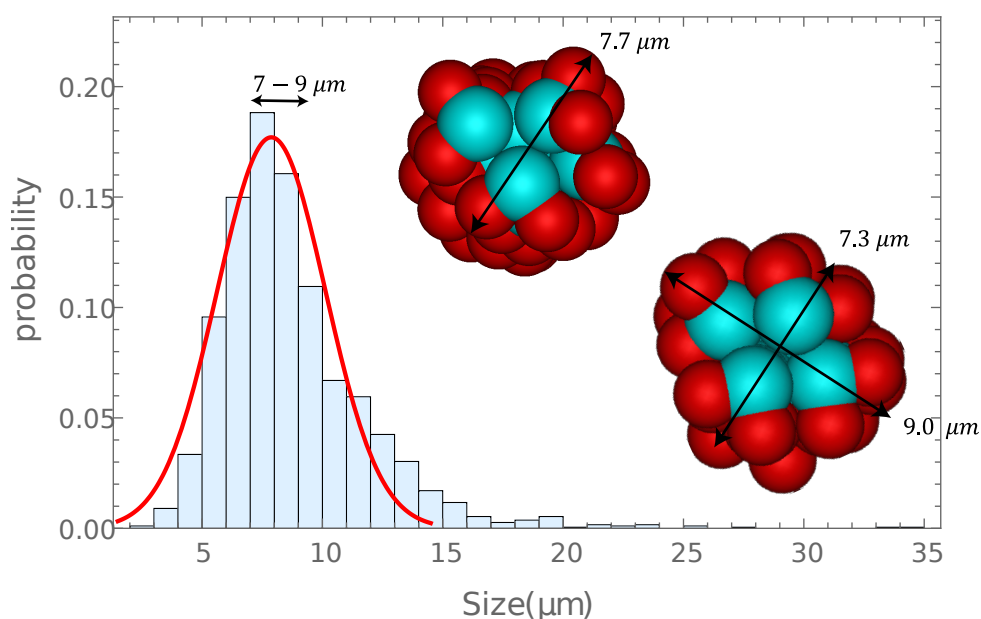


Figure 3.12: Distribution of tube diameters obtained from optical microscopy, with a Gaussian fit (in red). The diameter is well-defined around 7 to 9 μm . The insets show a cross-sections of the straight and spiral tube structures found in simulations, the diameters of which correspond to the peak in the distribution.

As can be seen in Fig. 3.7 and Fig. 3.8, the attractive smooth lobes are stacked in an ordered fashion. However, as the smooth lobes are free to rotate, the steric ears can also change position and essentially form a concentrated quasi-2D system of hard dimers on a cylinder.

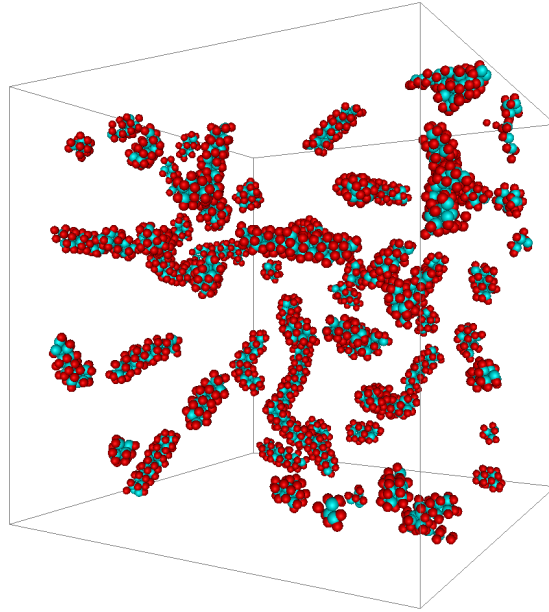


Figure 3.13: Simulation snapshot from MC simulations at $\phi_{\text{particles}} = 0.02$ and $\varepsilon = -10 k_{\text{B}}T$. Under these conditions and with the inclusion of cluster moves, considerably longer tubes form.

This gives rise to an inherently disordered, but heavily correlated configuration of rough lobes that dictates the direction from which additional particles can attach to the cluster and thereby contribute to the cluster structure. This mechanism can also cause branching of the tubes by occasionally allowing sufficient space between the rough lobes for a new particle to attach sideways (Fig. 3.11.c). However, this branching was only observed in experiments and not in simulations. Additionally, while the structure of the experimental clusters have the same diameter as the simulated tubes, they generally do not extend in one direction long enough to form a spiral (Fig. 3.11.c and d). It is therefore likely that also undesired experimental factors like particle size polydispersity and occasional rough-smooth attractive contacts contribute to disorder and branching.

In the case all particles had been incorporated in tube-like structures, the average number of bonds would have been expected to converge towards $\langle n \rangle \sim 6 - 6.5$. However, the computer simulations for attractions of $\varepsilon < -7 k_{\text{B}}T$ found that the number of bonds per particle converge to $\langle n \rangle \sim 5$. Adding cluster moves to the Monte Carlo simulations and increasing the particle concentration resulted in the formation of significantly longer tubes that also consisted of both straight and Bernal spirals. Fig. 3.13 shows a simulation snapshot with $\phi_{\text{particles}} = 0.02$ and $\varepsilon = -10 k_{\text{B}}T$. While in this situation longer tubes were formed, the average number of contacts was not significantly higher. This suggests that once the system has formed the observed tube-like structures, it is trapped in this state and cannot develop further.

To check if the same holds for the experiments, the time scales at which bonds between particles can break were calculated from the interaction potential using Kramers' approach [173] in the same way as performed previously [155]. In our system, the escape time for a single bond was found to range from 10 s for $\varepsilon = -7 k_{\text{B}}T$ to 10 minutes for $\varepsilon = -12 k_{\text{B}}T$. Escape times on the order of seconds for a single bond mean that pairs can break and form freely, and also

small clusters with up to 3 bonds per particle, which can be broken sequentially, can rearrange their structure. However, once a particle has formed 4 or more bonds, it is no longer possible to remove the particle without breaking at least 2 bonds simultaneously. Escape times for such configurations quickly rise to 10^5 s for breaking 2 bonds simultaneously and 10^{12} s for breaking 4 bonds, far beyond experimentally observable time scales. This means that once tube-like structures with 4 or 5 sufficiently strong bonds per particle are formed, the system gets trapped in this state and can no longer optimize its structure by breaking and reforming bonds. Although the internal structure of the clusters found in both experiments and simulations appears to be kinetically trapped, some particles can still exchange with the free particles in the medium, establishing a (local) equilibrium between the tubes and free particles.

3.4.2 Cluster structure and free particle concentration

Fig. 3.11 illustrates that upon increasing the interaction strength, the transition from hardly any clusters to an almost completely clustered system goes through a regime where both clusters and free particles are present. This concentration of free particles ϕ_{free} is easily determined in both simulations and experiments and can be related to the binding free energy of a particle to provide estimate information on the experimental cluster structure such as the average number of bonds.

The concentration of particles at which clusters start forming can be regarded as a critical micelle concentration (*cmc*) of a system of surfactants and consequently, just like with surfactants, this *cmc* is also the concentration of free particles present in the system once clusters are formed. This concentration can be related to the free energy difference between free particles and particles bound in a cluster via [155]

$$\phi_{\text{free}} = \phi_{\text{cmc}} \simeq \frac{v_{\text{MM}}}{v_{\text{av}}} e^{\Delta u/k_{\text{B}}T} \quad (3.6)$$

where ϕ_{free} is the volume fraction of free particles, v_{MM} is the volume of a colloid, v_{av} is a measure for the available free volume of a particle in a cluster and $\Delta u = \frac{\mu_n^\circ - n\mu_1^\circ}{n-1}$, where μ_n° is the chemical potential of a cluster of n particles and μ_1° is the chemical potential of a single particle. For large clusters ($n \gg 1$), Δu equals the average bonding free energy difference between a free particle and a particle in a cluster. Due to the system's short interaction range, bonds can be considered pairwise additive and the energy difference per particle is just half the number of bonds times the pair energy: $\Delta u = \frac{\langle n \rangle}{2} \varepsilon$. The v_{av} term in Eq. 3.6 is a measure of the translational entropy still available to particles in a cluster. The difference in rotational entropy between free particles and particles in a cluster is not taken into account in this equation, since particles bound by depletion interaction via their smooth lobes only lose a fraction of their rotational freedom due to geometric constraints.

The majority of particles in the tube-like clusters have the same number of bonds and, related to that, a similar value of v_{av} . A particle inside a cluster is confined in 3 dimensions such that $v_{\text{av}} = \xi^3$, where ξ is the width of the potential well the particle is in. This means that if there is an equilibrium between free particles and tube-like clusters in the system, the logarithm of the concentration of free particles, $\ln \phi_{\text{free}}$, should depend on ε via:

$$\ln \phi_{\text{free}} = \ln\left(\frac{v_{\text{MM}}}{\xi^3}\right) + \frac{\langle n \rangle}{2} \frac{\varepsilon}{k_{\text{B}}T} \quad (3.7)$$

Fig. 3.14 shows the logarithm of the free particle concentration $\ln \phi_{\text{free}}$ for the simulations at $\phi_{\text{particles}} = 0.01$ and the experimental systems with the lower ($\phi_{\text{particles}} = 0.003$) and higher ($\phi_{\text{particles}} = 0.01$) particle concentration. At low interaction strength, $\varepsilon/k_B T \sim 0$, only free particles are expected as in this case the total particle concentration is lower than the critical micelle concentration, $\phi_{\text{particles}} < \phi_{\text{cmc}}$. At sufficiently strong attractions, tubes and free particles are present and according to Eq. 3.7, $\ln \phi_{\text{free}}$ should depend linearly on ε , as is shown by the solid lines assuming values for ξ obtained from the shape of the interaction potential and a slope dependent on $\langle n \rangle$. At higher interaction strengths, from $\varepsilon \approx -8.5 k_B T$ in the simulations, almost all particles are part of a cluster and the fraction of free particles becomes too low to detect. Also in the experiments, hardly any free particles are found at higher values of $|\varepsilon|$, resulting in low concentrations ($\ln \phi_{\text{free}} \approx -10$) with large error bars.

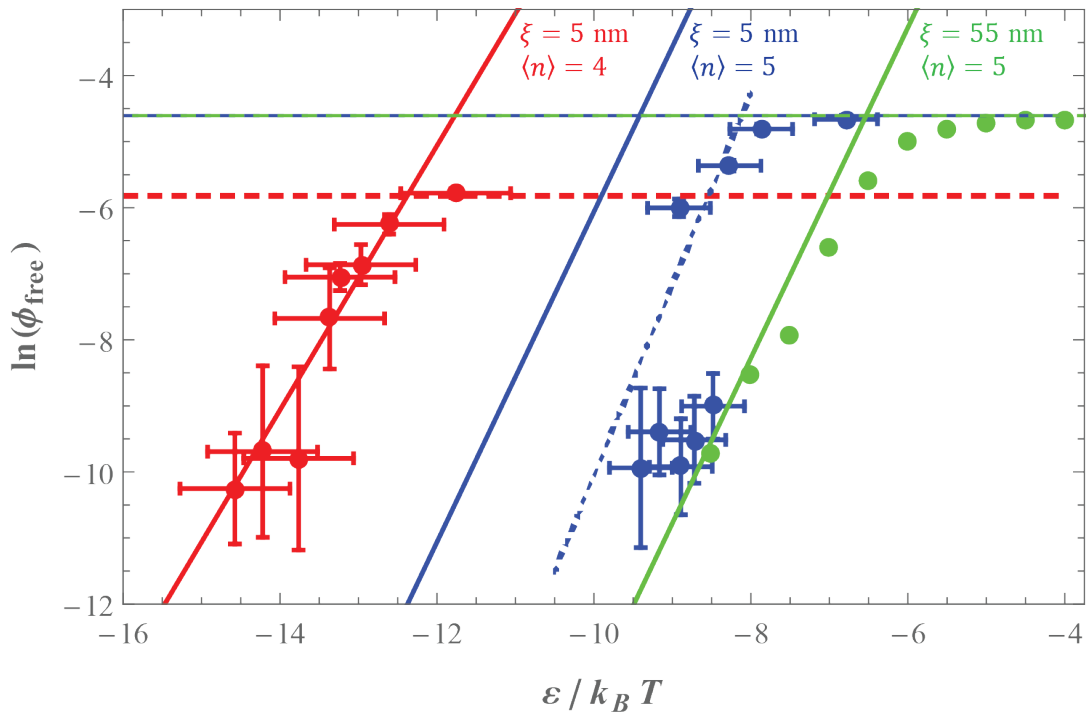


Figure 3.14: $\ln \phi_{\text{free}}$ as function of the system's pair interaction found for experiments at volume fractions $\phi_{\text{particles}} = 0.003$ (red) and $\phi_{\text{particles}} = 0.01$ (blue) and for computer simulations ($\phi_{\text{particles}} = 0.01$, green) plotted against ε . For the experiments, ε was calculated from experimental conditions (by finding the minimum of Eq. 3.3). For the simulation data, the depth of the square well ε was used. The solid lines represent plots of Eq. 3.7, using the values shown at the top as input parameters. The dashed horizontal lines mark the total particle concentrations $\phi_{\text{particles}}$. The dotted blue line is a fit of Eq. 3.7 finding $\langle n \rangle = 5.8$.

In the computer simulations performed for $\phi = 0.01$, upon increasing the attraction strength, the logarithm of the concentration of free particles was found to remain roughly constant up to $\varepsilon \approx -6 k_B T$, followed by a linear decrease over a range of $2 k_B T$. For the simulations, ξ is simply the width of the square well ($0.02\sigma_s = 55 \text{ nm}$) and $\langle n \rangle \approx 5$ (see Fig. 3.6). Using these numbers, the measured ϕ_{free} from the simulations is in good agreement with Eq. 3.7 in the region where tubes form.

The experiments performed for volume fractions $\phi_{\text{particles}} = 0.003$ and $\phi_{\text{particles}} = 0.01$, also show a decrease in $\ln \phi_{\text{free}}$ upon increasing attraction strength, from a point where all the particles are free, so $\phi_{\text{particles}} \approx \phi_{\text{free}}$, to a point where almost all particles are part of a larger cluster and $\phi_{\text{free}} \ll \phi_{\text{particles}}$. In the experiments, v_{av} is the volume that a bound particle can explore using its thermal energy, which can be approximated by the width of the potential well (Fig. 3.9) $1 k_B T$ above the potential minimum (approximately 5 nm in this case). We found that for the experiments at $\phi_{\text{particles}} = 0.003$, the data points show a good agreement with Eq. 3.7 using $\langle n \rangle = 4$. The small clusters in this system, like the ones shown in Fig. 3.10, suggest that this is a reasonable estimate for the number of bonds in the experiments at this concentration.

At a higher volume fraction $\phi_{\text{particles}} = 0.01$, where tube-like structures were observed also in experiments, the decrease of $\ln \phi_{\text{free}}$ with increasing attraction strength lies closer to the simulation values of the same $\phi_{\text{particles}}$ in Fig. 3.14. Because the tube-like structures in experiments at $\phi_{\text{particles}} = 0.01$ are comparable to those in the simulations in appearance (Fig. 3.11.d and h) and dimensions (Fig. 3.12), one would expect that $\langle n \rangle \approx 5$, which indeed provides reasonable agreement with the experimental data. However, we find a better fit to the measured data for $\langle n \rangle \approx 5.8$ (The dotted line in Fig. 3.14), indicating that the number of contacts is probably higher. This might be due to the presence of longer clusters with more branch points in the experiments compared to simulations.

The free particle concentration from both the simulations and experiments are in good agreement with Eq. 3.7, even though the system is not fully equilibrated. The trend in $\ln \phi_{\text{free}}$ provides a reasonable estimate of the number of bonds based on v_{av} and ε . The deviation from linearity that is present in the experiments, especially for higher depletant concentrations at $\phi_{\text{particles}} = 0.01$, can be attributed to the uncertainty in determining ε from the experiments. Firstly, as mentioned before, the surface potential of the smooth side of the particle is unknown and the value used to determine ε is most likely an overestimation. Secondly, the experimental error in determining ε , about $0.5 k_B T$, covers over a quarter of the total range where the decreasing free particle concentration can be determined.

The number of bonds obtained from the free particle concentration in the experiments corresponds to the overall $\langle n \rangle$ from the MC simulations (Fig. 3.6). Both values are lower than the 6 or 6.5 contacts for fully developed tubes (see Fig. 3.7 and Fig. 3.8), confirming that the tube-like clusters do not converge to their ground state under the present conditions.

3.5 Conclusions

In this chapter we presented Monte Carlo simulations on the self-assembly of trimers with anisotropic, selective, attractions, referred to as “Mickey Mouse” (MM) particles. These particles consist of one central smooth lobe connected to two rough lobes on either side at an angle of $\sim 90^\circ$. Specifically, we investigated the effect of tuning the interaction strength and the packing fraction of the system, and showed that, upon increasing the interparticle attraction, a transition between a gas and a cluster phase, and then the formation of tube-like structures are observed. We did not observe any significant effect of the packing fraction on the self-assembly behaviour, over all the range of investigated densities.

We compared our results to the experiments on the same system of colloidal particles performed in Ref. [79]. In the experiments, at sufficiently strong attractions and sufficiently high

particle concentration, the MM particles were shown to form tube-like structures. This is different from the spherical micelle-like clusters observed before for colloids with a single lobe [155]. Both in simulations and experiments, these particles were found to self-assemble into tube-like structures of seemingly unbounded length, but with a well-defined diameter. The structure of the tubes in the simulations consisted of a mixture of straight fragments and fragments in the shape of Bernal spirals. It is however hard to access equilibrium states in the experimental system, as the short ranged interactions and multiple bonds that can be formed by each colloid prevent them from effectively exploring many configurations on the experimental time scale. Although the predominant structure in the experiments therefore appears to be kinetically trapped, we could use the bond strength and bonding volume of the particles to get reasonable estimates for the number of bonds in the tube-like structures from concentration of free particles in the system.

Finite-sized clusters have been found experimentally for Janus particles with one sticky patch [174] and patchy dumbbells with an attractive lobe [155] and are supported by computer simulations [146, 149]. This work shows that the shape of the building block can be tuned to influence the final structure that is formed. In this case, the introduction of an additional non-sticky lobe even completely changed the dimensionality of the formed structures, marking important new steps on the road to the experimental realization of complex self-assembled colloidal structures. In particular, we highlight the formation of Bernal spirals of Mickey Mouse particles, as a direct result of the combination of the smooth lobes providing a selective short-range attraction and the steric ears facilitating directionality through an effective shielding. This is especially interesting as in previous works these structures were established either through careful tuning of the interaction potential [161, 162] or by well-defined attractive patches on the surface of spherical particles [163–165]. Since most patchy systems are, like the systems studied here, based on short-ranged interactions and considering the drive towards more complex patchy colloids, the results presented in this study are expected to play an increasingly important role in the practical realization of colloidal self-assembly.

Acknowledgements

I would like to thank Teun Vissers for the nice collaboration on this project. Joost Wolters, Fabian Hagemans, Daniela Kraft and Willem Kegel are gratefully acknowledged for all the experimental results presented in this chapter, and for the nice collaboration.

Phase separation and self-assembly in a fluid of “Mickey Mouse” particles

Recent developments in the synthesis of colloidal particles allow for control over shape and inter-particle interaction. One example, among others, is the so-called “Mickey Mouse” (MM) particle for which the self-assembly properties have been previously studied yielding a stable cluster phase together with elongated, tube-like structures. Here, we investigate under which conditions a fluid of Mickey Mouse particles can yield phase separation and how the self-assembly behaviour affects the gas-liquid coexistence. We vary the distance between the repulsive and the attractive lobes (bond length), and the interaction range, and follow the evolution of the gas-liquid (GL) coexistence curve. We find that upon increasing the bond length distance the binodal line shifts to lower temperatures, and that the interaction range controls the transition between phase separation and self-assembly of clusters. Upon further reduction of the interaction range and temperature, the clusters assume an increasingly ordered tube-like shape, ultimately matching the one previously reported in literature. These results are of interest when designing particle shape and particle-particle interaction for self-assembly processes.

4.1 Introduction

One of the fundamental questions in condensed matter physics is to understand the relation between the microscopic and macroscopic properties of a system. The answer to this question is also closely related to the possibility of creating new routes to fabricate novel functional materials. A variety of fabrication protocols has been devised over the past years, but more recently the focus has been shifted towards encoding information for the self-assembly into the basic colloidal building blocks [36, 175, 176]. This paradigm is now known as self-assembly or “colloidal LEGO”. Beforehand, it is unknown how the encoded information will manifest itself at the end of the self-assembly process, and it is even unknown what kind of encoded microscopic information will yield the desired macroscopic structure. Answering these questions is the key to using the self-assembly process of colloidal particles as a new method to fabricate functional materials.

“Hard” particle systems, which are purely entropic, give insights into the role of the particle shape in the self-assembly process. It has been shown that entropy alone can give rise to a large variety of close-packed crystal structures, as well as liquid and plastic crystal phases [37, 39–43, 45, 177, 178]. On the other hand, having particles explicitly attract each other along specific directions can be of advantage to target particular open structures as, for instance, diamond crystals and Kagome lattices [66, 179, 180]. This has brought a considerable amount of interest to what are now called patchy colloids, particles that interact with each other only via specific spots located at the particle’s surface [65, 67, 70, 101, 113]. Directional interactions can be given to colloids for example via attaching complementary DNA strands to the surface, as in Refs. [67, 181].

Another way of inducing directional interactions between building blocks is to combine depletion forces and surface roughness asymmetry [182–185]. In fact, if a building block is made up of rough and smooth lobes, the addition of depletants to the solution will induce specific attractions between the smooth lobes of different particles, while producing repulsions between the rough-smooth lobes and the rough-rough lobes [184, 185]. This approach has been used to self-assemble dumbbells [78] and, more recently, “Mickey Mouse” (MM) particles – trimers with one big smooth lobe (also referred to as the “head” of the MM particle) and two smaller rough lobes (the “ears”) [79]. In particular, in Ch. 3 we have shown that the MM particles self-assemble into tube-like structures at interaction strength of $\sim 9 - 10k_{\text{B}}T$.

Yet, with respect to isotropically attractive spheres like, for example, Lennard-Jones particles or Hard-Sphere Square-Well (HSSW) particles, that exhibit a gas-liquid (GL) phase separation, it is so far unclear whether MM particles can also undergo an analogous gas-liquid phase separation (colloidal poor-colloidal rich) and, if this is the case, what is the interplay of the latter with the depicted self-assembly scenario. The aim of this work is to address this question with Monte Carlo (MC) simulations. To do so, we follow the evolution of the GL binodal line for a series of models connecting the isotropic HSSW spheres to the MM particles. The path proceeds firstly by increasing the rough smooth (ear-head) bond length until we reach the experimental particle geometry, and secondly by decreasing the interaction range until the experimental one is reached, as described in Ref. 3.

The chapter is organised as follows: we introduce the model and the path connecting HSSW spheres and MM particles in Sec. 4.2, where we also discuss details about the different computational techniques we have used. In Sec. 4.3, we present our results on the phase separation

of MM particles and the transition to self-assembly. We also show how the particle geometry affects the structure of the liquid. We summarise and discuss these results in Sec. 4.4, where we also provide an outlook for future research directions.

4.2 Model and methods

4.2.1 Geometry and pair interaction

We begin with the geometry of the MM particle as shown in Fig. 4.1. Each MM particle is represented by an aggregate of three spheres, two small hard spheres (“ears”), of diameter σ_e , which represent rough lobes interacting with steric repulsions and a third bigger hard sphere (“head”), of diameter σ_h , which corresponds to the smooth lobe and plays the role of an attractive site. The interaction $u_{i,j}$ between a pair of MM particles i and j depends on the positional and orientational degrees of freedom $\mathbf{r}_i, \mathbf{r}_j, \Omega_i, \Omega_j$, respectively, which we drop here to lighten the notation, and consists of an attractive and a repulsive contribution,

$$u_{ij} = u_{ij}^{\text{att}} + u_{ij}^{\text{rep}} \quad (4.1)$$

The attractive part u_{ij}^{att} acts between the larger beads of particle i and j , and is given by a square-well (SW) interaction,

$$\beta u_{ij}^{\text{att}} = \beta u^{\text{SW}}(r_{ij}^{hh}) = \begin{cases} \beta \varepsilon & \text{for } \sigma_h \leq r_{ij}^{hh} \leq \lambda \sigma_h \\ 0 & \text{for } r_{ij}^{hh} > \lambda \sigma_h \end{cases} \quad (4.2)$$

where $\beta \varepsilon = \varepsilon/k_B T$, $\varepsilon < 0$, represents the interaction strength compared to the thermal energy, λ is the interaction range, and r_{ij}^{hh} is the centre to centre distance from the head of MM particle i to the head of MM particle j .

The repulsive part u_{ij}^{rep} , is determined by the hard-core interactions between the heads (h) and the ears (e_1, e_2) of two MM particles, and reads

$$\beta u_{ij}^{\text{rep}} = \sum_{\alpha, \beta = h, e_1, e_2} \beta u^{\text{HS}}(|\mathbf{r}_{i,\alpha} - \mathbf{r}_{j,\beta}|) \quad (4.3)$$

with the hard-sphere (HS) interaction,

$$\beta u^{\text{HS}}(|\mathbf{r}_{i,\alpha} - \mathbf{r}_{j,\beta}|) = \begin{cases} \infty & \text{if } |\mathbf{r}_{i,\alpha} - \mathbf{r}_{j,\beta}| < \sigma_{\alpha,\beta} \\ 0 & \text{otherwise} \end{cases} \quad (4.4)$$

where $\sigma_{\alpha,\beta} = (\sigma_\alpha + \sigma_\beta)/2$ with $\alpha, \beta = h, e_1, e_2$.

Finally, we set the ear-head size ratio to $q = \sigma_e/\sigma_h = 0.85$ and the angle between the directions of the ears to $\theta_{ee} = 90^\circ$, in order to match the values of the experiments in Ref. [79]. However, the centre-to-centre distance between the ears and the head, denoted hereafter as the bond length l/σ_h , is allowed to change, and it will be used as a parameter together with the interaction range. This particle and interaction model will be referred to as MMSW (Mickey Mouse Square-Well system). Note that in the limit $l/\sigma_h = 0$ our particles correspond to HSSW particles.

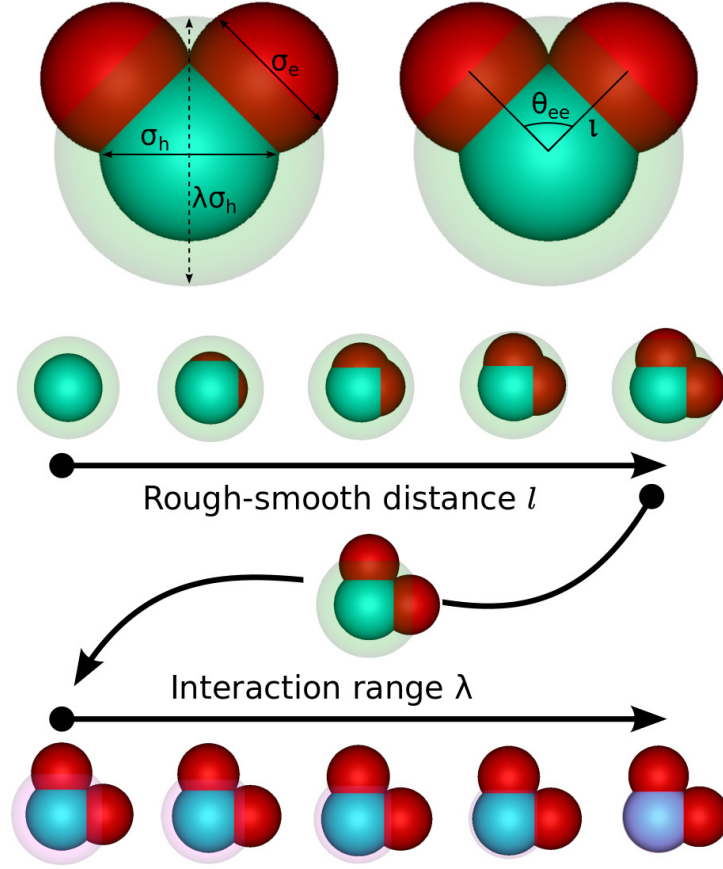


Figure 4.1: Model and parameters considered in this work. An experimental MM particle is obtained by a HSSW sphere by first changing the distance l/σ_h between the rough and the smooth beads (ear-head distance) and then by decreasing the interaction range λ . The red beads (rough protrusions) have diameter σ_e , while the blue bead (smooth protrusion) has diameter σ_h .

4.2.1.1 MM particle volume calculation

The volume of a MM particle v_p can be calculated exactly via MC integration, and in an approximated fashion considering the amount of overlap volume between the two ears and the head. In fact, from geometrical considerations, it holds that

$$v_p = V_h + 2V_e - 2V_{h,e} - V_{e,e} \quad (4.5)$$

where V_h is the volume of the attractive sphere, V_e the volume of the repulsive sphere, $V_{h,e}$ is the head-ear overlap volume, and $V_{e,e}$ is the ear-ear overlap volume. Since, as first approximation, the two ears in a MM particle do not overlap with each other in the region outside the head, their overlap volume $V_{e,e}$ is small compared to the head-ear one $V_{h,e}$ so the latter is the only quantity we need to calculate, which is given by

$$V_{h,e} \equiv V(R_h, R_e, l) = \frac{\pi(R_h + R_e - l)^2}{12l} \times (l^2 + 2lR_e - 3R_e^2 + 2lR_h + 6R_eR_h - 3R_h^2) \quad (4.6)$$

where $R_\alpha = 0.5\sigma_\alpha$, $\alpha = h, e_1, e_2$ are the radii of the attractive and the repulsive spheres and l is the centre to centre distance of the spheres.

The Monte Carlo integration is similar to a MC calculation of π , and we discuss it in the following. We place a MM particle in a box with fixed volume V , big enough to enclose the particle. We then generate a random position in the box and check whether it overlaps with the MM particle. If the number of generated random positions is $N_{\text{trial}} \sim \mathcal{O}(10^8)$ and the number of hits on the MM particles is N_{hit} , then the MM particle volume is given by

$$v_p \simeq V \frac{N_{\text{hit}}}{N_{\text{trial}}} \quad (4.7)$$

The results of the calculations for the volume of a MMSW particle are shown in Fig. 4.2, for the ratio studied in this paper $q = 0.85$, as a function of bond length l/σ_h . The MC integration and the theoretical calculation are almost indistinguishable.

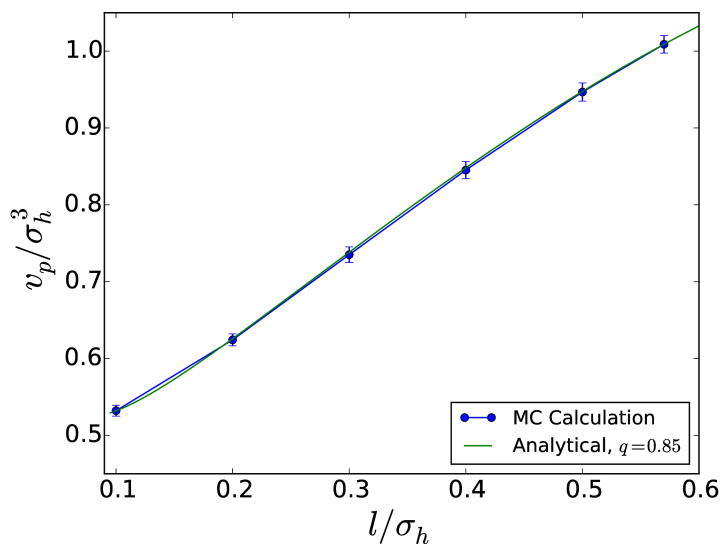


Figure 4.2: Volume of a MMSW particle as a function of bond length l/σ_h for size ratio $q = 0.85$. The solid green line is the prediction from Eq. 4.5 with $q = 0.85$, and the blue dots are the results from the MC calculations according to Eq. 4.7. The errors are multiplied by 10 for visualisation purposes.

4.2.2 Simulation methods

We focus on the effect of varying the ear-head distance l/σ_h of the particle and the interaction range λ on the gas-liquid (GL) binodal line, where we ignore the possibility of crystallisation. We compute the GL binodal using the Successive Umbrella Sampling (SUS) technique [186] together with the Histogram Reweighting method [187–190]. Since the SUS method has been discussed elsewhere [186], here we limit ourselves to only recalling the working scheme. The quantity of interest in the GL coexistence is $P(N)$, the probability that the system will be in a state with N particles at fixed volume V , fixed temperature T , and fixed chemical potential μ . This probability is unimodal above the critical temperature and assumes a typical bimodal shape, displaying gas and liquid peaks, for temperatures below the critical one. Furthermore, it can be shown that the bulk chemical potential at coexistence, at a given temperature, will be such that the area of the gas peak and the area of the liquid peak are equal. In fact, this is all

we need to know to determine the coexisting chemical potential via the histogram reweighting technique [187–190].

The probability distribution function can be computed by splitting the entire N range into overlapping windows of fixed size and by performing Grand Canonical Monte Carlo (GCMC) simulations in each window. During the simulation one keeps track of how many times the system has a certain particle number N , which lies in between the lower and the upper limit of the window. The probability function can be reconstructed via the “stitching” procedure, which reads [186]:

$$\frac{P(N)}{P(0)} = \frac{H_0(1)}{H_0(0)} \times \frac{H_1(2)}{H_1(1)} \times \cdots \times \frac{H_k(N)}{H_k(N-1)} \quad (4.8)$$

where we have implicitly assumed a window size of 1. From a computational point of view, Eq. 4.8 shows us that this scheme is inherently parallel since all the ratios can be estimated from independent simulations. This is very convenient from a computer cluster perspective.

Once $P(N)$ has been calculated for a fixed temperature and (irrelevant) chemical potential, the coexistence chemical potential can be obtained by reweighting the distribution until the area under the gas peak equals the area under the liquid peak. The reweighting is carried out via the following equation [191, 192]:

$$\ln P(N|\beta\mu_1) = \ln P(N|\beta\mu_0) + \beta(\mu_1 - \mu_0)N \quad (4.9)$$

In such a way, one can construct the GL coexistence envelope for particles with fixed geometry and fixed interaction range. In the following, we study how the GL coexistence curve is affected by the particle shape and particle-particle interaction range and where and how the regime of phase separation changes to self-assembly.

Once we obtain the GL coexistence curve, we attempt to estimate the critical point via a least-squares fit to the equation:

$$\rho_{\pm} - \rho_c = A |T - T_c| \pm \frac{1}{2} B |T - T_c|^{\beta} \quad (4.10)$$

which stems from the law of densities and the law of the rectilinear diameter [124, 191, 193, 194]. Here, \pm stands for liquid/gas and $\beta = 0.325$ is the exponent of the 3D Ising universality class. Such a procedure yields only a rough estimation and we stress that an appropriate determination of the GL critical point should involve extensive use of the finite-size scaling technique [195–198].

To explore under which conditions of particle geometry, temperature and interaction range the interparticle attractions are more important than the repulsions, we additionally compute the second virial coefficient normalised to the one of a system of hard spheres with diameter σ_h , $B_2^* = B_2/B_2^{\text{HS}}$. If attractions dominate, the value of the second virial coefficient will be negative, while positive otherwise. The temperature at which the second virial coefficient vanishes, so called Boyle temperature $k_B T_{\text{Boyle}}/\epsilon$, marks the crossing from one behaviour to another. The definition of the second virial coefficient involves the Mayer function, which takes into account the interaction between two MMSW particles [199, 200]

$$f_{ij} = \exp[-\beta u_{ij}] - 1 \quad (4.11)$$

The integral of the Mayer function over all possible positions and orientations of the two MM particles yields the second virial coefficient [199, 200]

$$B_2(k_B T/\varepsilon) = -\frac{1}{2V} \int d\mathbf{q}_1 d\mathbf{q}_2 f_{12} \quad (4.12)$$

where $d\mathbf{q}_i = d\mathbf{r}_i d\Omega_i$ represents integration over the particle's positional and orientational degrees of freedom. Eq. 4.12 can be computed via Monte Carlo integration. We place the MMSW "1" with fixed orientation in the middle of a box with volume $V = (5\sigma_h)^3$ at a given temperature $k_B T/\varepsilon$. We then generate a number $N_c \sim \mathcal{O}(10^8)$ of random positions and orientations for the MMSW "2" in the same volume, and for each configuration k we compute the value of the Mayer function between particle "1" and "2", f_{12}^k . Then, the second virial coefficient can be estimated as [201, 202]

$$B_2(k_B T/\varepsilon) = -\frac{V}{2} \frac{1}{N_c} \sum_{k=0}^{N_c} f_{12}^k = -\frac{V}{2} \langle f_{12} \rangle \quad (4.13)$$

where $\langle f_{12} \rangle$ represents the average of Mayer function over all the configurations. We repeat this computation for different temperatures, particle shapes and interparticle range to locate regions where attractions prevail with respect to repulsions.

4.3 Results

We have evaluated the GL coexistence curve for the MMSW model by varying the ear-head bond length l/σ_h from 0.1 to 0.57, corresponding to the experimental MM particles [79], and the particle-particle interaction range λ from 1.5 to 1.02. Following this path, we can connect the experimental MM system, for which the self-assembly behaviour has been investigated in Ch. 3, all the way to the HSSW limit, for which the GL coexistence has been intensively studied [124, 193, 194, 203].

4.3.1 Shift of the binodal line with the particle shape

With a fixed interaction range $\lambda = 1.5$, we change the particle shape by progressively increasing the bond length distance l/σ_h between the ears and the head of the MMSW particle. The highest value of bond length investigated in this work is set by the geometry of the experimental MM particle we want to match and reads $l/\sigma_h = 0.57$. We observe that the change in the MMSW particle shape affects the position of the GL coexistence curves, as seen in Fig. 4.3.

We quantify the change in the binodal curves, by computing the critical parameters as function of the bond length l/σ_h by means of a least square fit to Eq. 4.10. Going from the HSSW to the MMSW, the critical temperature $k_B T_c/\varepsilon$ shows a linear decrease upon increasing the bond length l/σ_h , as can be seen from Fig. 4.4. In Fig. 4.5, the critical density ρ_c is also seen to decrease monotonically with the bond length, while for the critical packing fraction ϕ_c we observe a non-monotonic behaviour which is caused by a decrease of the critical number density and a simultaneous increase of the particle volume v_p/σ_h^3 upon increasing the bond length l (for more details see Sec. 4.2.1.1).

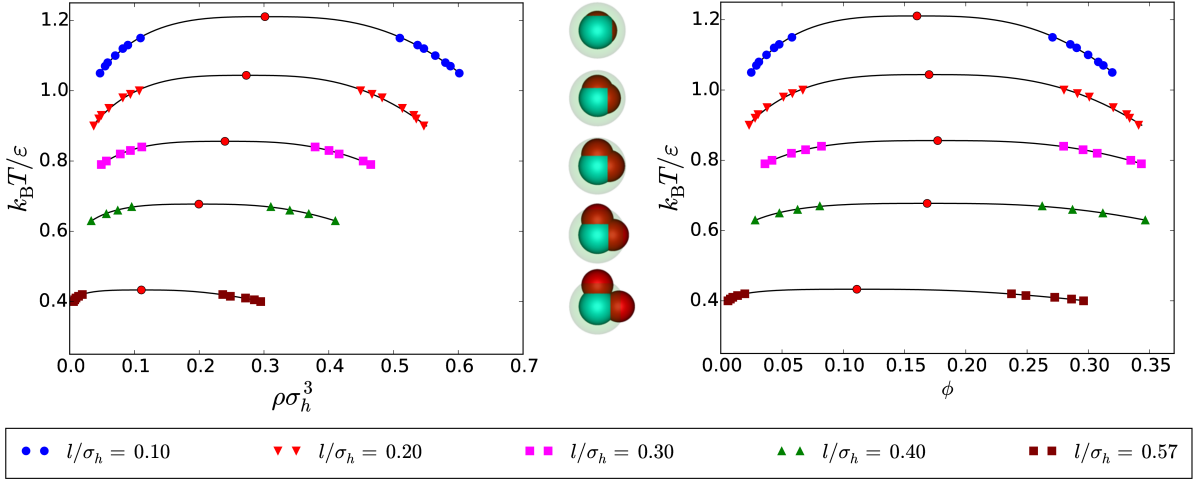


Figure 4.3: Gas-Liquid coexistence curves for MMSW particles. We provide both the temperature $k_B T/\varepsilon$ –density $\rho\sigma_h^3$, and temperature $k_B T/\varepsilon$ –packing fraction ϕ representation. The packing fraction is calculated as $\phi = Nv_p/V$, with v_p the particle volume as discussed in Sec. 4.2.1.1. The labels stand for different increasing values of the bond length l . The full red dots indicate the location of the critical points by Eq. 4.10.

Shifts of the critical temperature to lower values have been reported in different contexts. In fact, it is well known that attractive colloidal particles confined between two parallel plates display a shift of the critical point to lower temperatures because the confinement reduces the cohesive energy of the system [204–208]. More recently, the concept of “limited valence” has been introduced in the context of patchy colloids [56, 209–212]. The idea is that the valence of a particle (defined as the maximum possible number of bonded nearest neighbours) affects the location of a system’s critical point. Number of attractive patches [56, 209, 210], patch surface coverage [211, 212], patches with tunable attractions [116, 117], are all examples of controlling a particle’s valence. Our model suggests that changing the distance between the attractive and repulsive spheres is another way of achieving such a control. In other words, we can think of the bond length as a “knob” for limiting the valence of the MMSW particle. Interestingly, similar trends for the critical temperature and critical density were recently reported for a system of attractive dimers interpolating between SW-SW and HS-SW in Ref. [117].

The second virial coefficient at the critical point has been suggested as possible measure of a particle’s valence in Refs. [211, 213]. By using Eq. 4.13, we calculate the second virial coefficient B_2 at the critical point $k_B T_c/\varepsilon$ for each value of the bond length l/σ_h . Our results are shown in Fig. 4.6, where we have normalised the values by the second virial coefficient of a hard sphere of diameter σ_h . Upon increasing the bond length, the value of B_2 is seen to decrease (become more negative), which suggests that the limited valence picture could also hold in the system at hand. In this direction points also the difference in mean energy per particle $U/N\varepsilon$ of the coexisting liquid phases at $T = 0.90T_c$ for different bond length l/σ_h . In fact, $U/N\varepsilon(l/\sigma_h = 0.1) \sim -4.5$, while $U/N\varepsilon(l/\sigma_h = 0.57) \sim -3.5$. Since the difference of mean interaction energies equals half the excess number of bonds that a particle can have, we find that a MMSW particle with bond length $l/\sigma_h = 0.57$ forms 2 bonds less than a MMSW particle with bond length $l/\sigma_h = 0.1$, supporting the limited valence hypothesis.

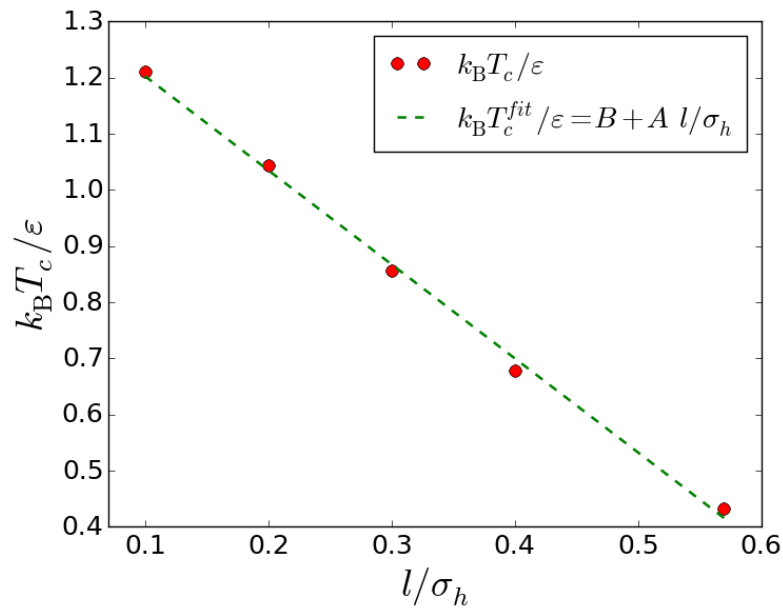


Figure 4.4: Critical temperature $k_B T_c / \epsilon$ (full red dots) as a function of bond length l / σ_h . The green dashed line shows the linear fit to the data for the critical temperature $k_B T_c^{fit} / \epsilon = B + A l / \sigma_h$, with $B = 1.37$ and $A = -1.66$, indicating a linear relation between the bond length “knob” and the system’s critical temperature.

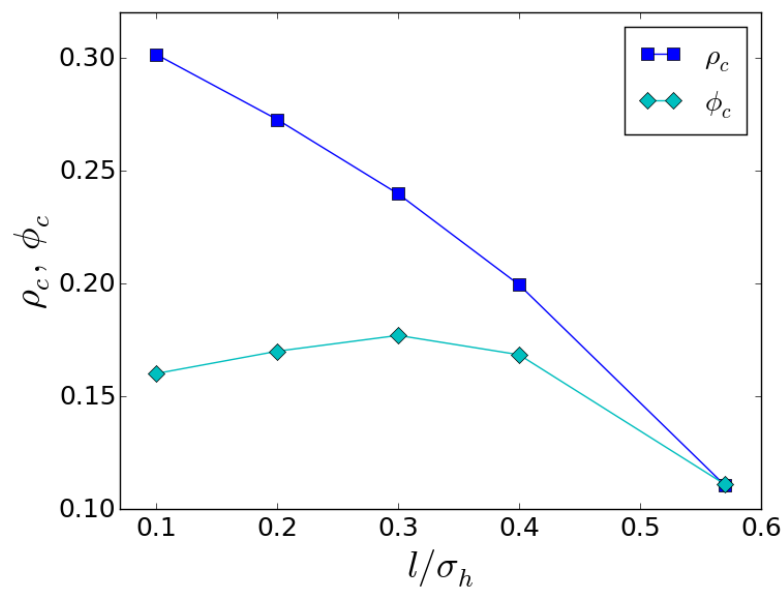


Figure 4.5: Critical density ρ_c (full blue squares) and critical packing fraction ϕ_c (full cyan diamonds) as a function of bond length l / σ_h . The solid curves are guides to the eye.

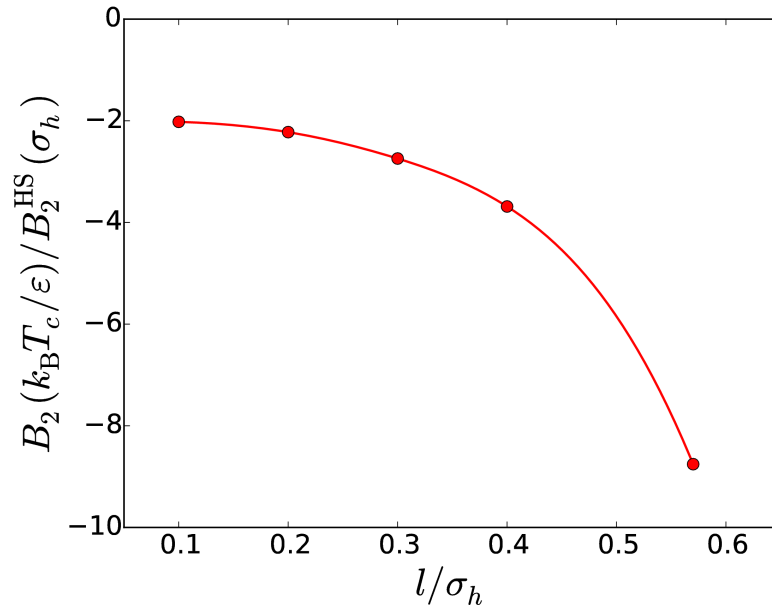


Figure 4.6: The reduced second virial coefficient at the GL critical point as a function of the ear-head bond length l/σ_h . The red line is a guide to the eye.

It is interesting to investigate the structure of the MMSW coexisting liquid phase as function of bond length, by keeping the volume fraction fixed at $\phi = 0.27$. We do this by calculating the radial distribution function for all the MM attractive beads (heads) $g^{\text{hh}}(r)$, the results being shown in Fig. 4.7, for bond length $l/\sigma_h = 0.1$ and $l/\sigma_h = 0.57$, respectively. We wish to remark here that we ignore the anisotropy of the particle and average over all possible particle orientations. Although both curves display features of the HSSW radial distribution functions, such as the presence of a hard-core diameter at $r/\sigma_h = 1$, and a discontinuity at $r/\sigma_h = \lambda = 1.5$, we see that the peak positions for the case $l/\sigma_h = 0.57$ hardly resembles the ones for $l/\sigma_h = 0.1$. In fact, especially the first peak of the radial distribution function moves to higher values of r/σ_h , specifically from $r/\sigma_h = 1$ for $l/\sigma_h = 0.1$ to $r/\sigma_h = 1.5$ in the case of $l/\sigma_h = 0.57$, and the same can be seen for the second and third peak. Clearly, even in the case of large interaction range $\lambda = 1.5$, the presence of the ears of the MM particle has an influence on the fluid structure, pushing the heads further away from each other on average.

4.3.2 Interaction range-driven transition to self-assembly

After having analysed how the particle shape affects the GL phase separation, we now ask ourselves how this behaviour ultimately transforms into self-assembly, which is the behaviour experimentally observed for the MM particles. In fact, the interaction range of the experimental MM particles system, i.e. $\lambda \sim 1.02$, is much smaller than the one so far considered ($\lambda \sim 1.50$). To this end, we perform a more extensive study of the second virial coefficient, where we map B_2 for several values of the interaction range, down to the experimentally relevant range, in the whole temperature $k_B T/\epsilon$ and bond length plane l/σ_h . This gives us an overview of the conditions under which the attractions overcome the repulsions, and guides us in the choice of regions of the parameter space which are interesting to simulate.

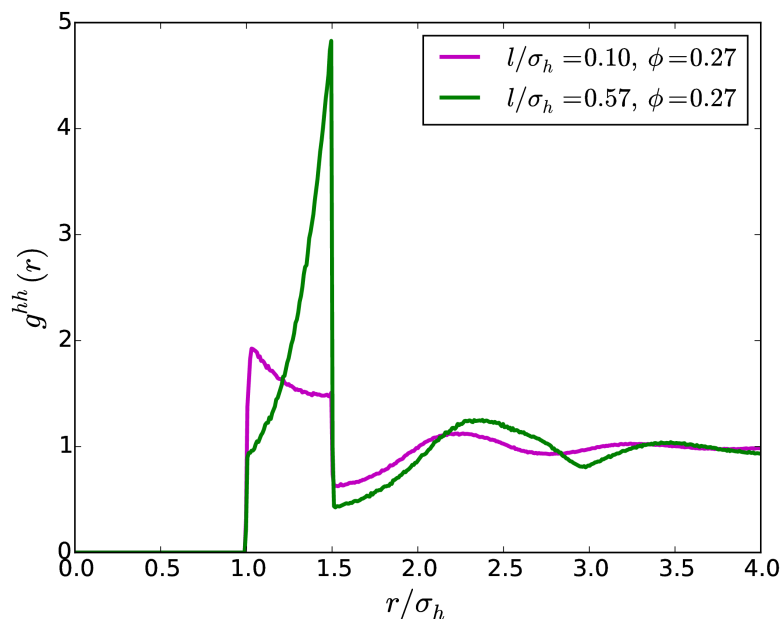


Figure 4.7: Bulk head-head radial distribution functions $g^{hh}(r)$ of the coexisting MMSW liquid at packing fraction $\phi = 0.27$ for bond length $l/\sigma_h = 0.1$ (magenta curve) and $l/\sigma_h = 0.57$ (green curve), as function of the distance r . The repulsive beads increase on average the spacing between the attractive beads.

Fig. 4.8 shows our results for the calculation of B_2 through the entire temperature $k_B T/\varepsilon$ bond length l/σ_h plane for different values of the interaction range $\lambda = 1.50, 1.40, 1.30, 1.20, 1.10, 1.02$. The results in Fig. 4.8 concern the sign of the second virial coefficient B_2 , red areas show a negative B_2 , where attractions overcome repulsions, and blue areas refer to a positive B_2 , where the repulsions are more important than the attractions. We remind the reader that the Boyle temperature $k_B T_{\text{Boyle}}/\varepsilon$ is defined as the temperature where the second virial coefficient B_2 vanishes. We also note that the case of MM geometry, which matches the experimental geometry in Ref. [79], is found at the right-most end of each diagram, where $l/\sigma_h = 0.57$.

For $l/\sigma_h = 0.57$, the region where $B_2 < 0$ is seen to dramatically shrink as the interaction range is decreased. This also means that the Boyle temperature is considerably dropping, going from $k_B T_{\text{Boyle}}/\varepsilon(\lambda = 1.50) \sim 0.9$ to $k_B T_{\text{Boyle}}/\varepsilon(\lambda = 1.02) \sim 0.15$. It is also known that for temperatures below ~ 0.1 the system can get stuck in kinetic traps and our calculations show that upon decreasing the interaction range λ up to $\lambda = 1.02$ the Boyle temperature gets closer to this limit. In such conditions, the temperature window where GL phase separation can be found is very small, if present at all. A confirmation of our calculation is given in Ref. [79], where it is mentioned that the temperature window between clustering and kinetic trapping is very narrow.

Based on the second virial coefficient analysis, the largest temperature window where it is in principle still possible to locate a GL phase separation is $\lambda = 1.40$, besides the already investigated case of $\lambda = 1.50$. We have therefore calculated $P(N)$ for a temperature range of $k_B T/\varepsilon \in [0.31, 0.35]$, the resulting distributions being shown in Fig. 4.9.

For all investigated temperatures, the distributions appear to develop a shoulder at higher particle number N than the first peak corresponding to the gas phase. Upon increasing the

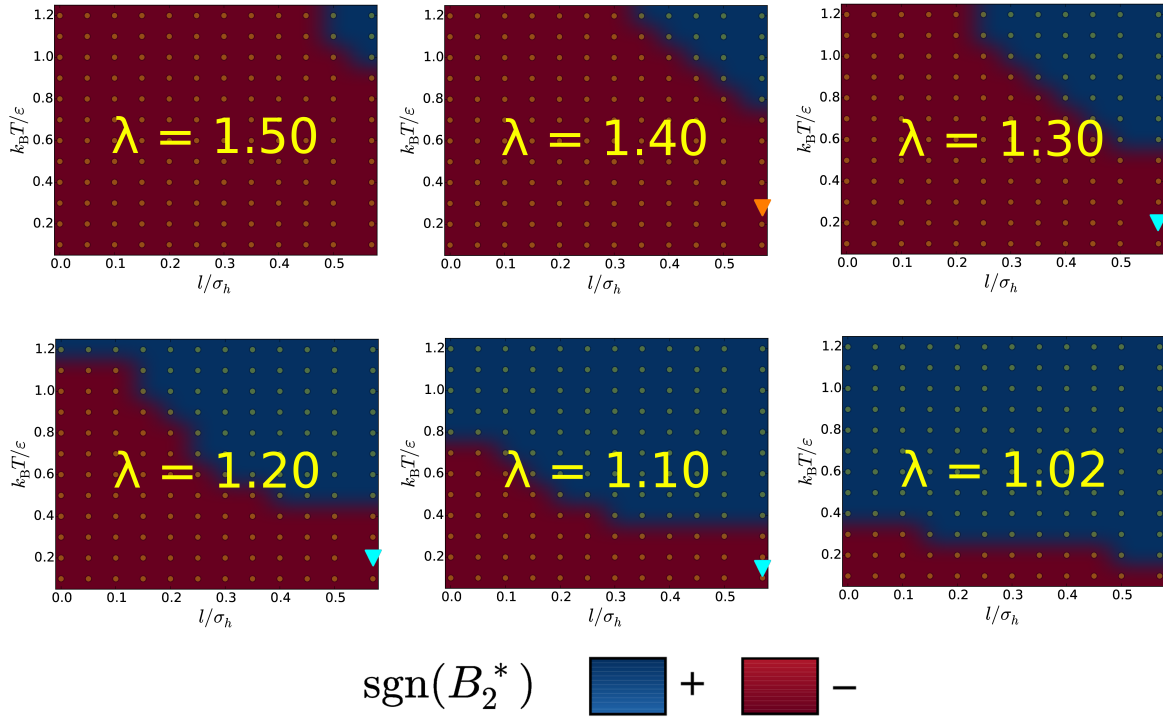


Figure 4.8: The sign of the reduced second virial coefficient B_2^* plotted in the reduced temperature $k_B T / \epsilon$ versus bond length l / σ_h representation, for various interaction ranges $\lambda = 1.50, 1.40, 1.30, 1.20, 1.10, 1.02$ as labelled. The orange triangle represent the state point where we have combined SUS and MC-NVT simulations as shown in Fig. 4.9 and 4.11, the cyan triangles represent the state points we have investigated only via MC-NVT simulations, see Fig. 4.11.

system volume, this second peak is shown to remain at the same location, as shown in the inset of Fig. 4.9, and is therefore associated with clusters developing in the system. This suggests that a self-assembly process preempts the macroscopic GL phase separation, either by shifting the transition to much lower temperatures than the investigated ones, or by destabilising the liquid with respect to the micellar fluid, as pointed out in previous works [117, 214–216]. Thus, even for the best case scenario of $\lambda = 1.40$, we have not found evidence of a GL phase separation, but instead we find indication of spontaneously formed aggregates in the system. Additional simulations for $\lambda = 1.48$ suggest that the GL coexistence curve moves to lower temperatures. Due to limited computer resources and slow equilibration at low temperatures it could not be ascertained whether or not the critical point remains present at finite temperatures in the limit $\lambda \rightarrow 0$.

The snapshots of the system for particle numbers within the micellar peak of $P(N)$ ($N = 15, N = 20$), shown in Fig. 4.10, reveal the disordered microscopic configurations of the clusters associated with the relatively high interaction range $\lambda = 1.40$.

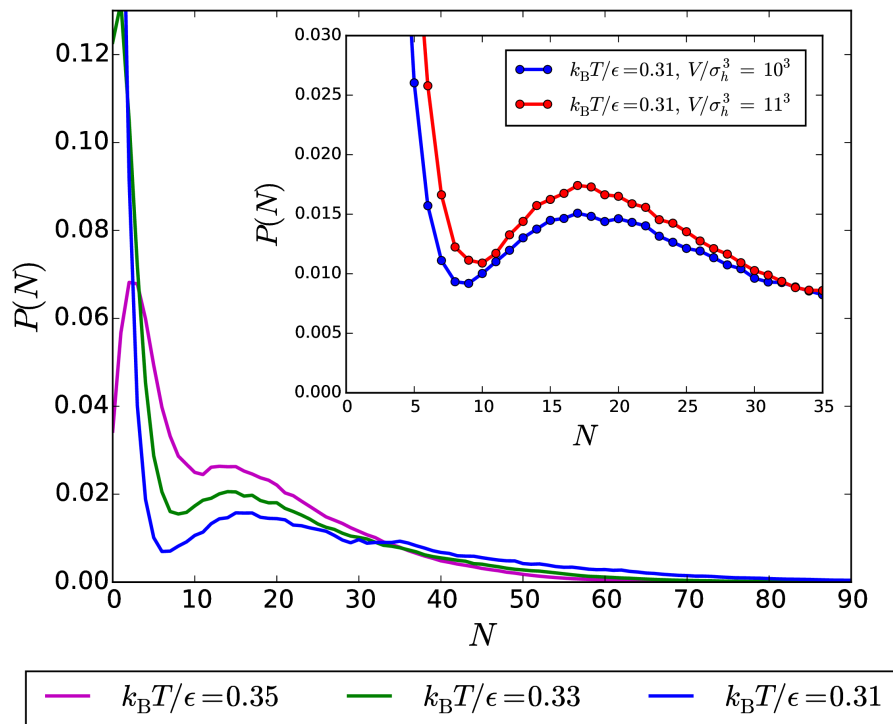


Figure 4.9: Probability $P(N)$ of finding N particles in the system for bond length $l/\sigma_h = 0.57$, interaction range $\lambda = 1.40$ and temperature as labelled. All the distributions are reweighted as to highlight the peaked region present for particle number $N \in [10, 40]$. Inset: finite size study performed at temperature $k_B T / \epsilon = 0.31$ confirming that the second peak is always located in the same window of particle number N .

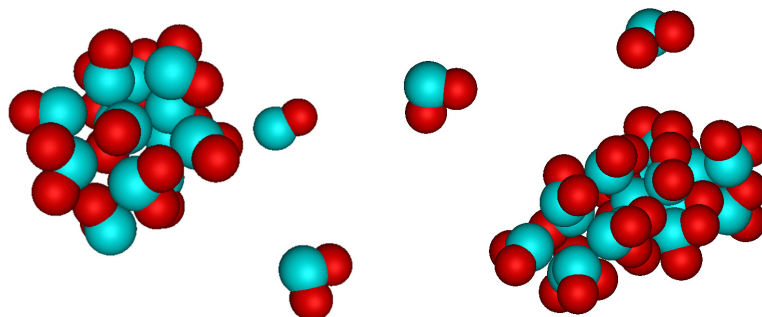


Figure 4.10: Disordered clusters of MMSW particles for bond length $l/\sigma_h = 0.57$, interaction range $\lambda = 1.40$ and temperature $k_B T / \epsilon = 0.31$. (left) $N = 15$, $\phi = 0.011$, (right) $N = 20$, $\phi = 0.015$.

For lower values of the interaction range λ , we select a few state points, as indicated in Fig. 4.8, and investigate the system via MC simulations in the NVT ensemble, due to computational reasons. The final configurations of the NVT simulations for $\lambda = 1.40, 1.30, 1.20, 1.10$ are reported in Fig. 4.11. The panel for a long ranged interaction $\lambda = 1.40$ (top left) displays a micellar fluid with clusters of a size comparable to the peak in the computed $P(N)$. On the other hand, the remaining panels for shorter-ranged interactions show self-assembled, tube-like structures. Once the self-assembly regime has been reached, starting at $\lambda = 1.40$, the shape of the resulting structures can be tuned by decreasing the interaction range. The backbone of the tubes becomes more close packed upon decreasing the interaction range, and the branching is suppressed for $\lambda \leq 1.05$. Thus, structures as the Bernal spirals, which were reported in Ch. 3, are eventually recovered upon shrinking the interaction range to values lower than $\lambda = 1.05$. Performing simulations with $N = 256$, $N = 512$ and $N = 1024$ particles, we found these results to be robust against finite size effects.

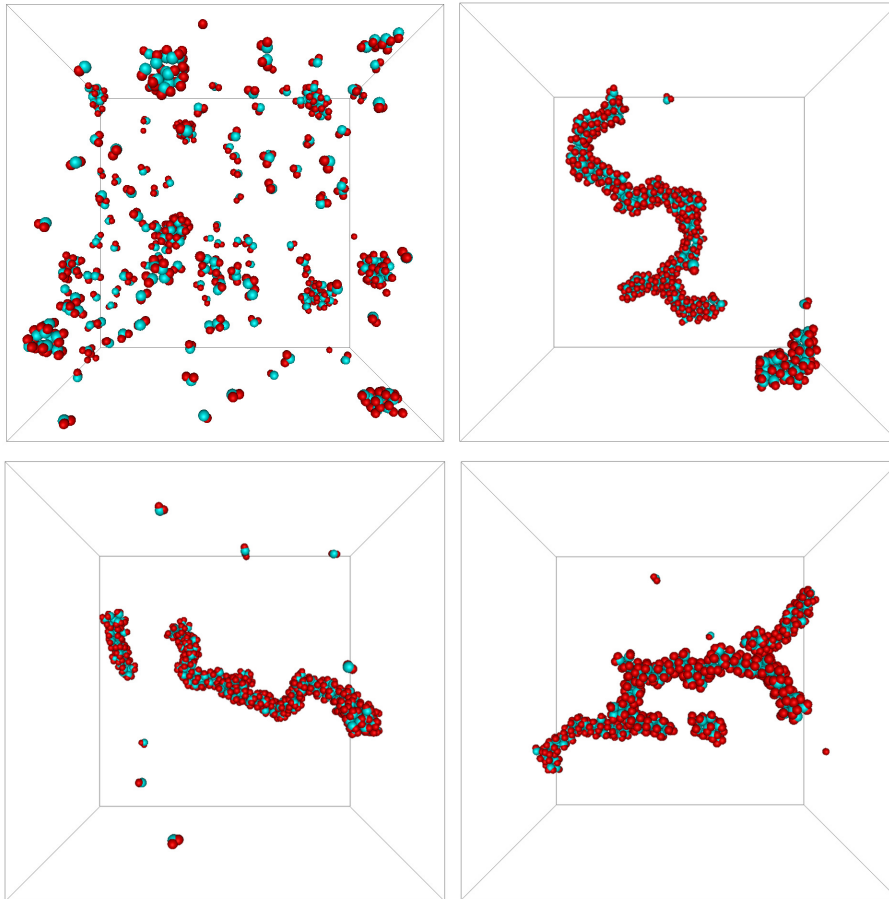


Figure 4.11: Snapshots from MC- NVT simulations at fixed packing fraction $\phi = Nv_p/V = 0.006$ and bond length $l/\sigma_h = 0.57$ for different interaction ranges λ and temperatures $k_B T/\varepsilon$ as described by the coloured triangles in Fig. 4.8. Top left: amorphous clusters for $\lambda = 1.40$ and $k_B T/\varepsilon = 0.310$, in agreement with the $P(N)$ calculated at the same temperature in Fig. 4.9; Top right: branched tube-like structures appearing at $\lambda = 1.30$ and $k_B T/\varepsilon = 0.200$; Bottom left: self-assembled tubes at $\lambda = 1.20$ and $k_B T/\varepsilon = 0.200$; Bottom right: branched tubes at $\lambda = 1.10$ and $k_B T/\varepsilon = 0.143$. For all the panels, $N = 256$ and $V = 35\sigma_h^3$.

The above findings highlight the role of the interaction range in the self-assembly of MM particles: shrinking the interaction range first destabilises the GL phase separation with respect to self-assembly, and then favours the formation of increasingly ordered structures, eventually recovering those found in Ch. 3.

In a very recent work, the fluid phase behaviour of trimers with one soft, attractive bead and two soft, repulsive beads has been investigated [217]. There are substantial differences with our investigation, which we summarise in the following. Firstly, the particle model employed here uses hard-core particles, whereas the model in Ref. [217] makes use of soft-core particles. Secondly, the shape of their trimer is slightly different from our MM particle, since we keep the angle between the repulsive beads fixed. Thirdly, their methodology is fundamentally different, although it aims to compute the same quantity $P(N)$. Lastly, due to the form of the SW potential, we can explicitly control the interaction range between two particles, and track down the evolution of the self-assembly with it. Notwithstanding these differences, it is interesting to compare our results to Ref. [217]. Concerning the shift of the binodal line with the bond length distance, both works have found a linear scaling. The slopes of the scaling are comparable, our estimate being $a = -1.67$, see the fit in Fig. 4.4, against the reported $a = -1.40$. However, the actual values of the critical points for specific bond lengths do not match with each other, the discrepancy being ascribed to the differences in the particle geometry and particle-particle interaction. Furthermore, by very different analyses, both works agree on the region where the tube-like structures are expected to occur for the system presented in Ch. 3 – roughly for temperatures $k_B T/\epsilon < 0.15$.

The results from our work show interesting similarities with those in Ref. [117]. In that work, a system of colloidal dumbbells where both beads are attractive is transformed into “Janus” dumbbells, via progressively decreasing the interaction parameter of one of the beads with respect to the other. As a result, the GL coexistence curve is seen to move to lower and lower values of temperatures, and the critical temperature is found to scale with the interaction parameter. This is somewhat reminiscent of the critical temperature scaling we have encountered in our work, but there is a fundamental difference in the parameters which drive the scaling: in Ref. [117], this is due to the interaction strength, whereas in our work the driving parameter is the bond length, a geometrical quantity. Nevertheless, we believe both works present nice examples of achieving limited valence with different “control knobs”.

4.4 Conclusions

In this work we have investigated, via Monte Carlo simulations, how the combined actions of particle geometry and particle-particle interaction range affect the gas liquid phase separation. We have also addressed the role of the interaction range onto the self-assembly process.

Starting from the well-known HSSW model, we have mapped out the different binodal curves for a family of Mickey Mouse particles with increasing steric repulsion. We have found that there is a linear relation between the critical temperature $k_B T_c/\epsilon$ of the binodal curves and the bond length l/σ_h , which controls the influence of the repulsive spheres on the overall interaction. We interpreted this phenomenon in the “limited valence” paradigm and documented it by calculating the value of the second virial coefficient at the critical temperature $B_2^*(k_B T_c/\epsilon)$ as function of bond length l/σ_h . This is a possible measure of the effective valence of the

system and indeed we have proven that this value decreases as the valence is reduced, which is controlled in this case via the bond length. We have also seen an increase of the internal energy of the coexisting liquid phases upon increasing the bond length, which is yet another indication that less bonds are being formed in the system.

The transition from macroscopic GL phase separation and self-assembly is driven by the interaction range, which has also an important effect on the Boyle temperature T_{Boyle} of the system. In fact, as the interaction range is reduced, both the Boyle temperature decreases and the phase separation process is preempted by a self-assembly process. Microscopic configurations from the SUS simulations, complemented with snapshots from *NVT* simulations, have shown that the structure of the self assembled clusters changes from disordered to more ordered, branched tube-like structures. Upon further decrease in the range, these structures are seen to transform into the very ordered ones as reported in Ch. 3.

Our results highlight the role of particle geometry and interparticle interaction range in the competition between phase separation and self-assembly for Mickey Mouse particles and, in general, trimers with one attractive sphere and two repulsive spheres. This is of direct interest for experiments where trimers are used as basic building blocks, where – as we have documented – both the trimer exact shape and the trimer-trimer interaction range are expected to play a significant role. At a more general level, we have shown how tuning a particle's valence can be achieved by controlling the bond length. This conclusion is expected to hold also in other particle geometries as long as the particles are composed of different beads, e.g. colloidal dimers with one rough (repulsive) and one smooth (attractive) beads.

Part II

Anisotropic particles with excluded-volume interactions

Fabrication of colloidal Laves phases for photonic crystals via hard tetramers and hard spheres: bulk phase diagram and stacking diagram for sedimentation

Colloidal photonic crystals display peculiar optical properties which make them particularly suitable for application in different fields. However, the low packing fraction of the targeted structures usually poses a real challenge in the fabrication stage. Here, we propose a novel route to colloidal photonic crystals via a binary mixture of hard tetramers and hard spheres. By combining theory and computer simulations, we calculate the phase diagram as well as the stacking diagram of the mixture, and show that a colloidal analogue of the MgCu_2 Laves phase – which can serve as a precursor of a photonic bandgap structure – is a thermodynamically stable phase in a large region of the phase diagram. Our findings show a relatively large coexistence region between the fluid and the Laves phase, which is potentially accessible by experiments. Furthermore, we determine the sedimentation behaviour of the suggested mixture, by identifying several stacking sequences. Our work uncovers a new self-assembly path towards a photonic structure with a band gap in the visible region.

5.1 Introduction

It is known that colloidal particles can spontaneously form ordered, periodic phases which are the analogue of crystals in atomic systems. The most prominent example of such a transition, first discovered by computer simulations [11–13], and later confirmed by experimental work [14], is the formation of a face-centered-cubic (FCC) crystal from a fluid of colloidal particles which behave as hard spheres (HS).

The study of crystalline phases on colloidal length and time scales is important not only at a fundamental level, where it allows for insights into e.g., phase transitions and crystallisation kinetics [15–17], but also for potential applications. In particular, it is possible to fabricate photonic crystals (PCs) from colloidal particles. By PCs we mean structures with periodically varying dielectric constant that display a complete photonic band gap. Due to the intrinsic size of the employed building blocks, colloidal photonic crystals display a band gap in the visible range of frequencies. These structures act for photons in the same way semiconductors do for electrons, hence opening up a way to control light propagation. The application area of such materials is quite broad, ranging from optical fibres, displays and switches to (bio-)sensing and bio-medical engineering, and finally to energy storage and security [18–29]. Therefore, a significant amount of research in the colloid science community deals with the design and fabrication of such photonic crystals.

Since the early work on PCs [218–221], different particle arrangements were explored as a candidate [222–227], and some of them – most notably the so called “inverse opals” – were also fabricated in the lab [228–233]. To date, the most suitable structures to make PCs remain the Diamond Crystal (DC) and the Pyrochlore structure, in which the colloids are located on the lattice positions of the respective crystal structures [59, 60]. However, despite the efforts, the fabrication of such open (non close-packed) structures at the colloidal scales has not been achieved yet, and it is a long-standing research focus in the nanomaterials and colloidal science community.

Nevertheless, new perspectives on the subject arise because recent advances in the colloidal synthesis allow for more and more exotic building blocks to be used in the colloidal self-assembly arena. Clusters of spheres with well defined shapes, such as dimers, trimers and tetramers, have become available, together with the intriguing possibility of employing them to self-assemble PCs [42, 184, 234–239]. These colloidal clusters can be produced in several ways. One method takes advantage of the drying forces in an evaporating emulsion droplet to drive the confined colloidal particles to a specific geometry [234, 235, 237]. A different class of fabrication procedures relies instead on microfluidics setups, with or without the use of lithographically patterned surfaces [239–243].

In addition, on the theoretical side, two new ideas were put forward to possibly facilitate the fabrication of PCs, and we shall briefly discuss them in the following. One study showed that a structure composed of tetrahedral clusters of spheres (“tetrastack”) displays a photonic band in the optical region [244]. However, while they employ a complex building block, it is not clear how the suggested structure can be realised experimentally. Another study suggested that, by using a binary mixture of colloidal particles with different sizes, it is possible to assemble an MgCu_2 Laves phase. This is appealing because the MgCu_2 consists of a DC of large spheres and a Pyrochlore lattice of small spheres, and both substructures display a photonic bandgap [245]. In this case, the authors addressed the problem posed by the open structure by using a binary

mixtures of spheres. Nevertheless, issues arise when one considers that three phases can actually be assembled from a binary hard-sphere mixture, namely the MgCu_2 , the MgNi_2 , and the MgZn_2 . It is also important to note that the latter is the thermodynamically stable phase, and unfortunately not the aimed MgCu_2 phase [246]. Furthermore, the three aforementioned Laves phases are nearly degenerate as they have very similar free energies, hence the self-assembly of the mixture results in glassy states, unless the assembly is directed, *e.g.*, by using templated walls [245].

In this work, we combine Monte Carlo (MC) computer simulations and theory to study the phase behaviour of a binary mixture of large hard spheres and rigid, hard tetrahedral clusters of small hard spheres (hereafter denoted as tetramers) with a fixed size ratio. For this mixture, we compute both the bulk phase diagram and the sedimentation behaviour. In particular, using free-energy calculations, we address the stability of the MgCu_2 Laves phase that can result from the self-assembly of the mixture. In this way, we retain the best of both approaches previously introduced, while also circumventing some of the other problems.

For instance, employing a binary mixture mitigates the problem of the low-coordinated open target structures of the diamond and pyrochlore phase, whereas using tetramers as one of the building blocks alleviates the lattice degeneracy problem as MgNi_2 phase cannot be self-assembled from tetramers and spheres, and moreover using tetramers also removes the metastability problem as the MgCu_2 phase is more stable than the MgZn_2 phase in mixtures of tetramers and spheres. Hence, the particular choice of colloidal building blocks intrinsically pre-selects the desired structure, and thus the MgCu_2 Laves phase is obtained by design. Furthermore, by using the bulk phase diagram and the local density approximation, we theoretically calculate the stacking diagram of the mixture, which predicts the stacking sequences of different phases that could be observed in sedimentation experiments on the same mixture.

We stress that such a model mixture is well within experimental reach, even though no studies on it have been performed yet, to the best of our knowledge. This is somewhat surprising as hard-core systems are usually much easier to control than systems with attractive interactions, which often requires substantial fine-tuning of the range, strength, and directionality of the interactions.

This chapter is organised as follows. We introduce the model and discuss the employed methods in Sec. 5.2. In Sec. 5.3 we present the results on the phase behaviour of the binary mixture of spheres and tetramers, while in Sec. 5.4 we discuss the sedimentation behaviour. In Sec. 5.5 we sum up our findings, and outline future research directions.

5.2 Model and methods

5.2.1 Monte Carlo simulations

We consider a binary mixture of N_s hard spheres and N_t hard tetramers with composition $x = N_s/N$, where $N = N_s + N_t$. The spheres have diameter σ_L . Each tetramer consists of four touching spherical beads of diameter σ_B arranged in a tetrahedral fashion. We assume the tetramers to behave like a rigid body, *i.e.*, fluctuations in the geometrical arrangement of the spheres are neglected. The size ratio between a bead in a tetramer and a sphere is labelled as $q = \sigma_B/\sigma_L$. Since the MgCu_2 Laves phase of an ordinary binary hard-sphere mixture achieves its

highest packing fraction for $q = \sqrt{2/3} \sim 0.82$ [245–248], we employ this value in our work. All interactions are assumed to be HS-like, meaning that the objects do not interpenetrate each other. Thus, spheres cannot approach each other closer than σ_L , beads belonging to different tetramers cannot approach each other closer than σ_B , spheres and tetramer beads cannot approach closer than $\sigma_{LB} = (\sigma_L + \sigma_B)/2$. A model of the different building blocks employed in this work is shown in Fig. 5.1.

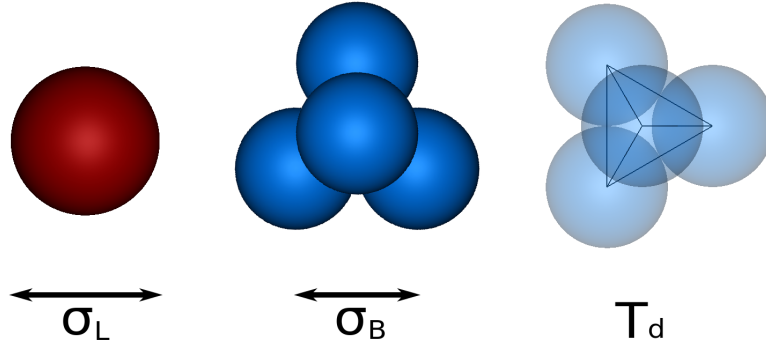


Figure 5.1: Building blocks of the investigated binary mixture. (left) Hard spheres with diameter σ_L . (centre) Hard tetrahedral tetramers of bead size σ_B . Note that the beads are tangential to one another. The size ratio $q = \sigma_B/\sigma_L$ is fixed to 0.82. (right) Faceted model of a tetrahedron, with symmetry group T_d , connecting the centres of the beads.

In order to map out the phase diagram of the system, we combine Monte Carlo (MC) simulations in the isobaric-isothermal ensemble and free-energy calculations. Hence, the relevant thermodynamic quantities are N_s, N_t, P, T . The pressure P is measured in reduced units as $\beta P \sigma_L^3$ with $\beta = 1/k_B T$, k_B Boltzmann's constant, and T the system temperature. The dimensionless number density is $\rho \sigma_L^3 = N/V$, where V represents the volume of the simulation box. The packing fraction is defined as $\eta = \gamma \rho$, with $\gamma = \pi \sigma_L^3 [x + 4q^3(1-x)]/6$. To evolve the system, we use displacement moves for spheres and tetramers, rotational moves for tetramers, and volume moves. For each move, we set an acceptance rate of 30%. An MC step (MCS) is defined as N attempted translations or rotations, and one volume move of the simulation box. The length of the simulations in the isobaric-isothermal ensemble is at least 5×10^6 MCS, while the free-energy calculations run for at least 2×10^6 MCS. For the case of non-cubic crystal structures, we also employ NPT simulations where the box lattice vectors are free to fluctuate, in order to remove any additional stress from the crystal phase [87, 88]. For each composition of large spheres x , the equation of state (EOS) is computed by means of compression and expansion runs. For the compression runs, the starting configuration is a disordered fluid of $N_s = xN$ spheres and $N_t = (1-x)N$ tetramers. For the expansion runs, crystalline structures of selected composition provide the initial configuration as explained in the following.

5.2.2 Crystalline structures

For a binary hard-sphere mixture, previous studies have shown that, at the chosen size ratio $q = \sigma_B/\sigma_L = 0.82$, the stable crystal structures are the FCC crystals of large and small spheres, and the MgZn_2 Laves phase [245, 246], whereas the MgCu_2 Laves phase can be stabilised by

wall templating [245]. In the case of a mixture of tetramers and spheres, we employ the same packing arrangements as those in Ref. [246], but we replace four small spheres by a tetramer. This procedure yields structures which are made from the investigated building blocks (spheres and tetramers), but are arranged similarly to the respective literature cases. Here it is important to note that the third kind of Laves phase – the MgNi_2 crystal – cannot be reproduced by a combination of tetramers and spheres, hence it falls already out of the picture when considering candidate crystal structures.

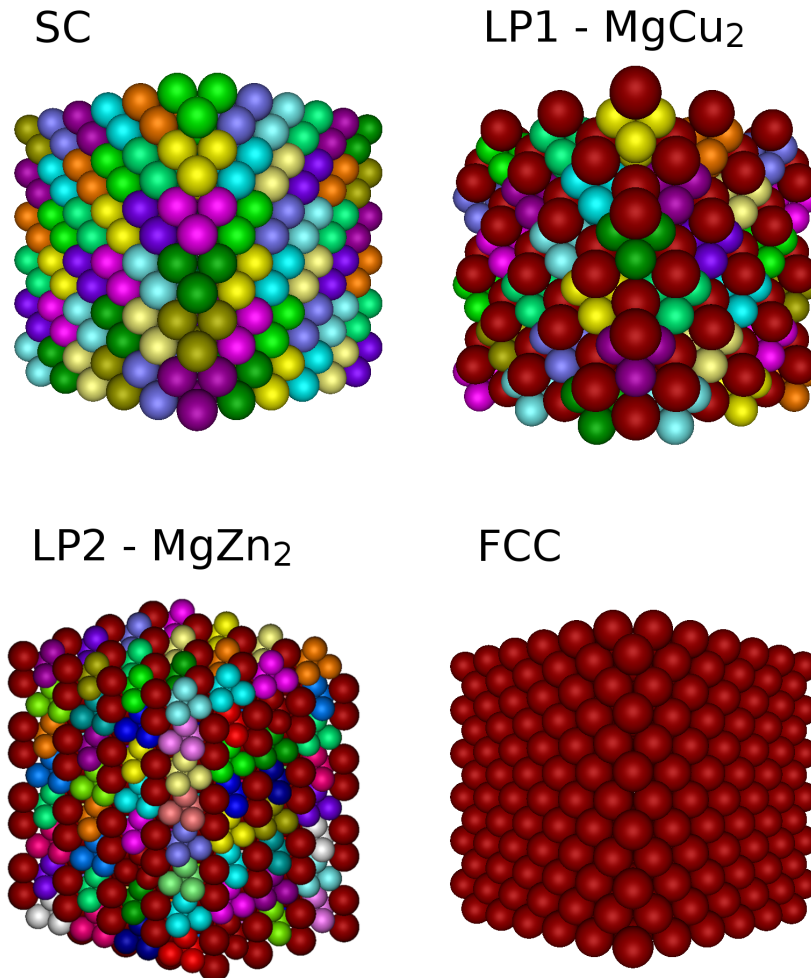


Figure 5.2: Crystal structures considered in this work. (top left) The Simple Cubic crystal of pure tetramers (SC) at composition $x = 0$. (top right) The binary MgCu_2 Laves phase (LP1) at composition $x = 2/3$. (bottom left) The binary MgZn_2 Laves phase (LP2) at composition $x = 2/3$. (bottom right) The Face Centered Cubic crystals of pure large spheres (FCC) at composition $x = 1$. The colour code identifies different tetramers and separates tetramers from spheres.

Summing up, for different compositions of large spheres x we have:

- SC** simple cubic lattice of tetramers with specified orientation at composition $x = 0$.
- LP1** a mixed structure of tetramers and spheres, which packs the same way as an ordinary MgCu_2 lattice, at composition $x = 2/3$.

LP2 the analogue of the MgZn_2 crystal, but made out of tetramers and spheres, also at composition $x = 2/3$. Note that this structure has a non-cubic unit cell.

FCC the thermodynamic stable structure for hard spheres, at composition $x = 1$.

In the SC, LP1 and LP2 phases, respectively, all the tetramers have the same orientation, which is calculated by a rigid transformation of the bead positions in the reference frame to the bead positions in the crystal at hand. We note that other arrangements are, in principle, possible for the SC phase, with respect to both the positions and the orientations of the tetramers, nevertheless the positions of the beads of the tetramers must always be compatible with an FCC packing. Moreover, the degeneracy of the SC phase, if present at all, is expected to be small [249], hence we neglect it in our calculations.

5.2.3 Free-energy calculations

The bulk phase diagram is determined by using the common tangent construction in the Gibbs free-energy g – composition x representation. We remind the reader that the dimensionless Gibbs free energy per particle is defined as $g = \beta G/N = f + Z$, where $f = \beta F/N$ is the dimensionless Helmholtz free energy per particle and $Z = \beta P/\rho = \gamma\beta P/\eta$ is the compressibility factor.

Thus, in order to compute the Gibbs free energy g , one must first calculate f , and thermodynamic integration is the method of choice for this task [90]. Starting from a reference point, f is obtained by integrating the EOS to the packing fraction of interest η , assuming no phase transition is crossed along the integration path

$$f(\eta) = f(\eta_0) + \frac{\gamma}{k_B T} \int_{\eta_0}^{\eta} d\eta' \frac{P(\eta')}{\eta'^2} \quad (5.1)$$

The main problem is now shifted to the computation of f at the reference point. For the fluid phase we choose this point to be an ideal gas mixture. For the crystal phases we use the Frenkel-Ladd method extended to account for the anisotropic particle shape [90, 250–252]. In this method, one connects an Einstein crystal, where particles are tied to their ideal lattice positions and orientations by harmonic springs, to the system of interest by slowly removing the harmonic springs. More details can be found in Ref. [252] and references therein. The Helmholtz free-energy per particle f of a crystal reads [251, 252]:

$$f(\eta_0) = f_{\text{Einst}}(\lambda_{\text{max}}) - \frac{1}{N} \int_0^{\lambda_{\text{max}}} d\lambda' \left\langle \frac{\partial U_{\text{Einst}}(\lambda')}{\partial \lambda'} \right\rangle_{\text{NVT}} \quad (5.2)$$

where f_{Einst} , which stands for the free energy per particle of an ideal Einstein crystal, is given by:

$$f_{\text{Einst}}(\lambda_{\text{max}}) = -\frac{3(N-1)}{2N} \ln \left(\frac{\pi}{\lambda_{\text{max}}} \right) + \ln \left(\frac{\Lambda_t^3 \Lambda_r}{\sigma_L^3} \right) + \frac{1}{N} \log \left(\frac{\sigma_L^3}{VN^{1/2}} \right) + (1-x)f_{\text{or}}(\lambda_{\text{max}}) \quad (5.3)$$

In Eq. 5.2, the function $U_{\text{Einst}}(\lambda)$ denotes the harmonic potential that couples the particle positions and orientations to the corresponding Einstein lattice values and reads:

$$\beta U_{\text{Einst}}(\lambda) = \lambda \sum_{i=1}^N (\mathbf{r}_i - \mathbf{r}_{i,0})^2 / \sigma_L^2 + \lambda \sum_{i=1}^{N_t} (\sin^2 \psi_{ia} + \sin^2 \psi_{ib}) \quad (5.4)$$

where $(\mathbf{r}_i - \mathbf{r}_{i,0})$ represents the displacement of particle i from its position in the ideal Einstein crystal, and where the angles ψ_{ia} and ψ_{ib} are the minimum angles formed by the vector pointing to any of the beads in the tetramer and the rest position of two arbitrarily chosen beads a and b , respectively. Note that all the spheres and tetramers are connected with springs to their respective lattice positions in the Einstein crystal, whereas an aligning potential is acting only on the tetramers. The term $f_{\text{or}}(\lambda_{\text{max}})$ in Eq. 5.3 takes into account the orientational free energy of the ideal Einstein crystal and reads:

$$f_{\text{or}}(\lambda_{\text{max}}) = -\ln \left\{ \frac{1}{8\pi^2} \int d\phi d\theta d\chi \sin(\theta) \times \exp \left[-\frac{\lambda_{\text{max}}}{k_B T} (\sin^2 \psi_{ia} + \sin^2 \psi_{ib}) \right] \right\} \quad (5.5)$$

where ϕ , θ and χ are the Euler angles. This integral depends only on the maximum value chosen for the coupling constant λ and, of course, on the form of the Hamiltonian chosen for the orientational springs. In simple cases, it can be evaluated exactly or in an approximated analytic form. However, when the orientational Hamiltonian is more complex as in the current case, it must be calculated numerically, e.g. via MC integration.

Once the Helmholtz free energy is known, the Gibbs free energy per particle for fixed composition and varying pressure is calculated as

$$g(P, x) = f(\eta_0, x) + \gamma \int_{\eta_0}^{\eta} d\eta' \frac{\beta P(\eta', x)}{\eta'^2} + Z(P, x) \quad (5.6)$$

With the outlined procedure, we calculate the Gibbs free energy $g(P, x)$ for the fluid phase at different compositions with a grid spacing of 0.1, as well as the Gibbs free energy $g(P, x)$ for the solid phases. We then use the common tangent construction in the (g, x) -plane to draw the phase diagram. A representative calculation of $g(P, x)$ is given in Fig. 5.3, where we also show the results of the common tangent construction. By collecting the information about $g(P, x)$ at several pressure values, we eventually map out the phase diagram of the binary mixture in the pressure $\beta P \sigma_L^3$ – sphere composition x representation.

5.2.4 Stacking sequences and stacking diagram

Once ascertained the bulk thermodynamics, we also study the system sedimentation behaviour. To this end, we theoretically construct a stacking diagram which is the set of all possible sequences of phases stacked in a sedimentation column, following the method recently presented in Ref. [253]. The theory behind the construction of a stacking diagram is based on chemical potentials, hence the bulk phase diagram in the $P - x$ representation must first be converted to the plane of the chemical potential of the spheres (L) and tetramers (T), respectively. In the following, we assume that such a conversion has been done and only discuss in terms of chemical potentials of the two species.

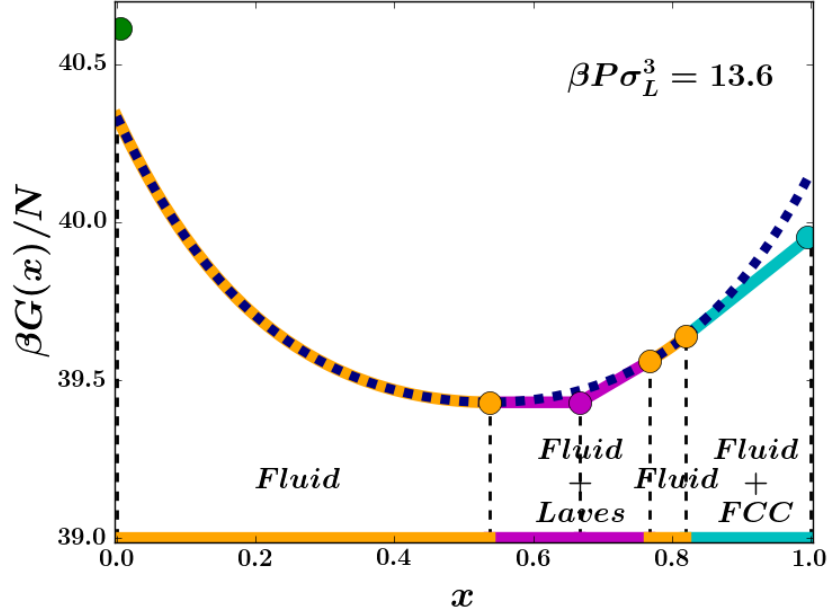


Figure 5.3: Gibbs free energy per particle $g = \beta G(P, x)/N$ as function of composition $x = N_s/N$ for a fixed pressure $\beta P \sigma_L^3 = 13.6$. The green, magenta and cyan dots represent the SC phase of pure tetramers (at $x = 0$), the LP1 crystal (at $x = 2/3$), and the FCC of pure large spheres (at $x = 1$), respectively. The blue dashed line shows the Gibbs free energy $g(P, x)$ of the fluid as function of composition x . The orange dots represent the coexistence points between the fluid and the LP1 crystal (2 points), and between the fluid and the FCC crystal of pure large spheres, as calculated by the common tangent construction. The thick lines show the path of minimal Gibbs free-energy.

Once gravity is switched on, there is an increasing concentration profile along the column in the direction of gravity z . We now define a z -dependent chemical potential which varies with concentration along the sedimentation column

$$\psi_i(z) = \mu_i^0 - m_i g z \quad (5.7)$$

where $\psi_i(z)$ is the chemical potential of species $i = \{L, T\}$ at a height z of the column and μ_i^0 is its chemical potential in the absence of gravity, and m_i its buoyant mass. Rearranging Eq. 5.7 and eliminating the z -dependence, we obtain a linear relation between the chemical potential of the spheres $\psi_L(z)$ and the chemical potential of the tetramers $\psi_T(z)$

$$\psi_L(\psi_T) = a + s \psi_T \quad (5.8)$$

$$s = m_L/m_T \quad (5.9)$$

$$a = \mu_L^0 - s \mu_T^0 \quad (5.10)$$

where s is the gravitational variable and a is the composition variable.

Assuming the local density approximation (LDA) is valid, we can set the local chemical potential $\psi_i(z)$ of species i equal to the chemical potential μ_i of an equilibrium bulk state, i.e.

$$\psi_i(z) = \mu_i \quad (5.11)$$

so that the correlation between s and a appears as a straight line (Eq. 5.8) on the plane of chemical potentials $\mu_T - \mu_L$. This straight line is called a “sedimentation path” and the set of all such lines constitutes a stacking diagram. The point at which a sedimentation path crosses a bulk binodal represents a phase transition. Therefore, each path yields a specific stacking sequence of phases in the corresponding stacking diagram.

5.3 Bulk phase behaviour

In this section, we present and discuss our results for the bulk phase diagram of the binary mixture of spheres and tetramers, including a representation of the phase diagram more suitable to experiments.

5.3.1 Equations of state

The equations of state (EOS) of both the fluid phase at different compositions x and of the crystalline structures considered are a key ingredient of the calculation of the phase diagram, as we see from Eq. 5.6. For the fluid phase, we calculated the EOS at composition intervals of 0.1, whereas for the crystal phases the compositions are fixed. In Fig. 5.4 we show the EOS of the different crystal structures investigated, as well as the EOS of the fluid mixture at different compositions x .

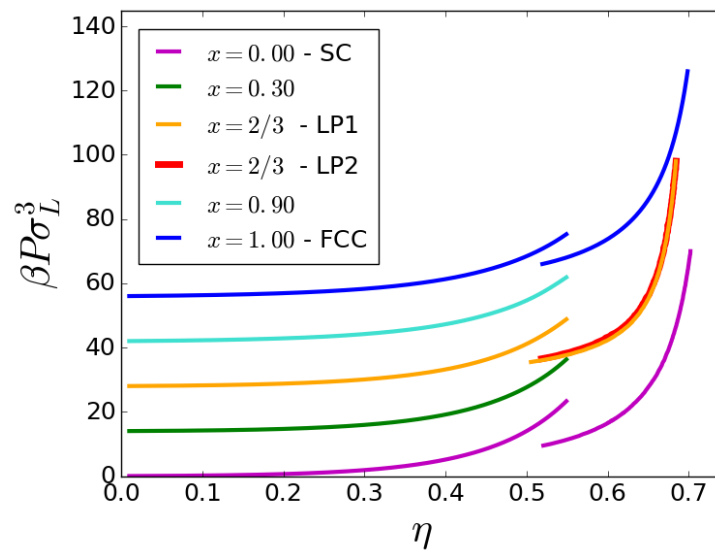


Figure 5.4: EOS of the mixture of large hard spheres and hard tetramers at different compositions x . The solid branches correspond to expansion runs of the studied solid structures, namely SC at $x = 0.0$, LP1 and LP2 at $x = 2/3$, and FCC at $x = 1.0$. Note that the EOS of LP1 and LP2 coincide for high pressures, but differ at lower pressures. For visualisation purposes, the curves have been shifted with respect to each other in the y direction by an amount $\Delta y = 14$.

We subsequently fit the simulation results to

$$\frac{\gamma\beta P}{\eta} = 1 + \sum_{i=1}^n a_i \eta^i \tag{5.12}$$

for the fluid phase, and

$$\frac{\gamma\beta P}{\eta^2} = \sum_{i=0}^m b_i \eta^i \quad (5.13)$$

for the crystal phases. The typical value of n is 12, while $m = 3$ for all cases. The fitting procedure allows us to easily perform the thermodynamic integration in Eq. 5.6.

5.3.2 Stability of LP1 and phase diagrams

Previous work on binary hard-sphere mixtures has shown that, unless wall templating is used, the MgZn_2 Laves phase is more stable than the MgCu_2 Laves phase [245, 246]. Unfortunately, the MgCu_2 structure is the only Laves phase whose sublattices display a complete photonic band gap [59, 60]. Hence, the first issue for us to investigate is the thermodynamic stability of LP1– MgCu_2 compared to LP2– MgZn_2 . We addressed this by performing free-energy calculations at a fixed packing fraction of $\eta = 0.60$ for different total number of particles N . By plotting the excess free energy per particle including finite-size corrections versus $1/N$ for both structures, we can extrapolate to the thermodynamic limit $N \rightarrow \infty$ by looking at the intercept of the two lines. This is displayed in Fig. 5.5, where it becomes clear that the LP1– MgCu_2 structure of hard tetramers and hard spheres is more stable than the LP2– MgZn_2 structure in the thermodynamic limit.

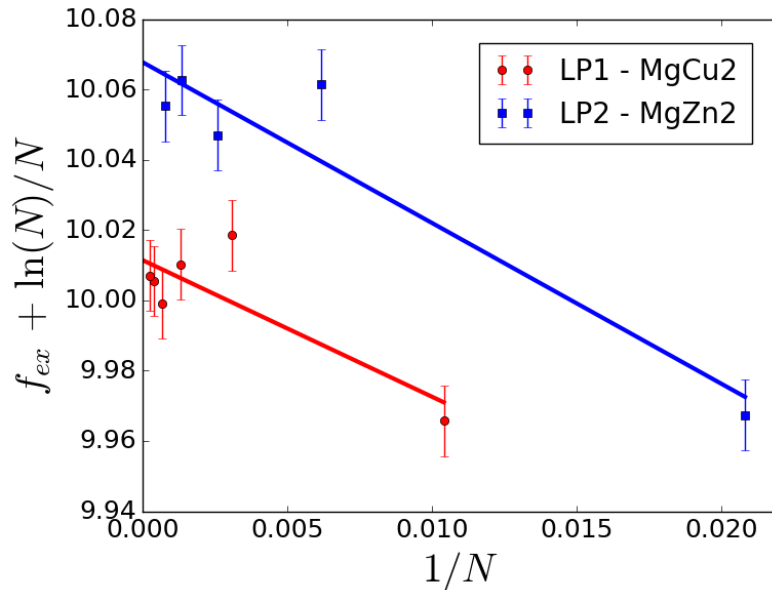


Figure 5.5: Finite-size scaling of the excess Helmholtz free energy $f_{ex} + \ln(N)/N$ vs $1/N$ at diameter ratio $q = 0.82$ and packing fraction $\eta = 0.6$ for the LP1– MgCu_2 and LP2– MgZn_2 Laves structures of hard tetramers and hard spheres. The lines are linear fits to the data points. The LP1 crystal is always significantly more stable than the LP2 structure, the free energy difference in the thermodynamic limit being $6 \times 10^{-2} k_B$ per particle.

The LP1 structure has a bulk excess free energy per particle of $10.01(1)k_B T$, while the LP2 crystal has an excess free energy per particle of $10.07(1)k_B T$, the difference being $6 \times 10^{-2} k_B T$. Incidentally, we note that this free-energy difference is not at all small, being hundreds of times

larger than the free-energy difference between an FCC and an HCP of hard spheres. Thus, by employing a mixture of hard tetramers and large hard spheres, the MgCu_2 structure – the precursor of colloidal photonic crystals – is stabilised in bulk. In view of this result, we will refer to LP1 more generically as “Laves phase” in the following.

To draw the phase diagram in the pressure $\beta P\sigma_L^3$ –composition x representation, we apply common tangent constructions to the Gibbs free-energy curves $g(P,x)$ at different pressures, in order to determine the composition and densities of the coexisting phases. The results are summarised in Fig. 5.6.

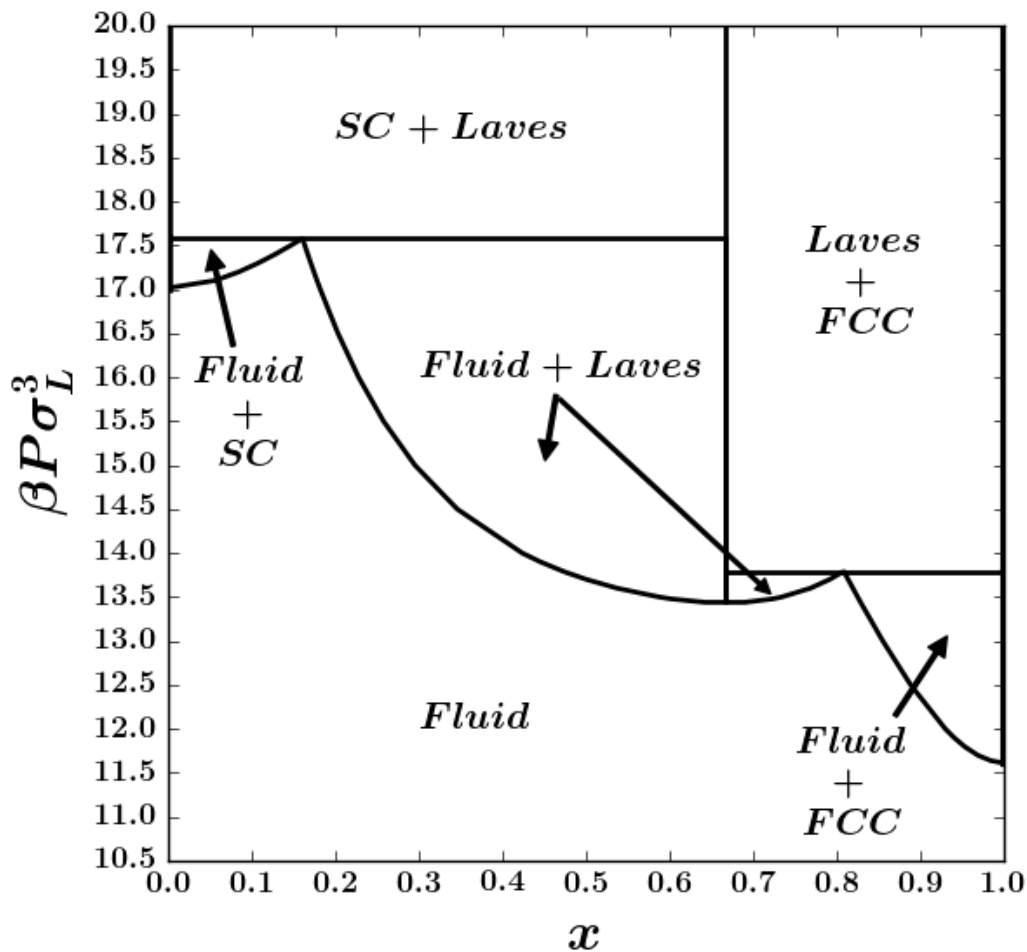


Figure 5.6: Phase diagram of a binary mixture of hard spheres and hard tetramers in the pressure $\beta P\sigma_L^3$ –composition x representation. The composition $x = N_S/N$ refers to the spheres. Two triple points (Fluid+SC+Laves, Fluid+Laves+FCC) are found, together with a relatively large phase coexistence region between the fluid and the Laves phase.

For pressures $\beta P\sigma_L^3 \leq 11.5$, we find that the fluid is the only stable phase. Increasing the pressure results in different coexistence regions, between the fluid and the three crystal structures investigated, and between the different crystal structures at even higher pressures.

For $11.5 \leq \beta P\sigma_L^3 \leq 13.9$ and compositions $x > 0.81$ we find coexistence between the FCC crystal of large spheres and the fluid phase, while for $17.0 \leq \beta P\sigma_L^3 \leq 17.6$ and compositions $x < 0.17$ we find a coexistence between the simple cubic crystal of tetramers and the fluid phase.

Interestingly, at intermediate pressures and compositions we observe two distinct phase coexistence regions between the Laves phase and the fluid phase with either a composition smaller or larger than that of the Laves phase, *i.e.*, $x \leq 2/3$ and $x \geq 2/3$. Moving towards high pressures we find solid-solid coexistence between the simple cubic phase of pure tetramers and the Laves phase, and between the Laves phase and the pure FCC phase of large spheres, the former starting at somewhat higher pressures than the latter ($\beta P \sigma_L^3 > 17.6$ vs $\beta P \sigma_L^3 > 13.9$).

For very high pressures, we expect, due to packing considerations, only a single coexistence region between the simple cubic phase of tetramers and the FCC crystals of large spheres, *i.e.* we expect to find another triple point where the SC, Laves, and FCC phases are in coexistence with each other. However, we were unable to detect the crossover, even by simulating at pressures as high as $\beta P \sigma_L^3 = 70.0$. Thus, we can only set a lower limit on this specific crystal-crystal phase coexistence region.

The relatively large two-phase coexistence region between the fluid phase and the Laves phase is the most remarkable feature of the presented phase diagram, signalling an extended and easily accessible parameter range to obtain the targeted MgCu_2 Laves phase in simulations as well as in experiments. We checked this result by additionally performing direct coexistence simulations at overall compositions $x = 0.5$ and $x = 0.6$ and pressure $\beta P \sigma_L^3 = 15.0$. In Fig. 5.7 we present snapshots of the final configurations as obtained from the simulations, which confirm the coexistence between the fluid phase and the Laves phase of tetramers and spheres.

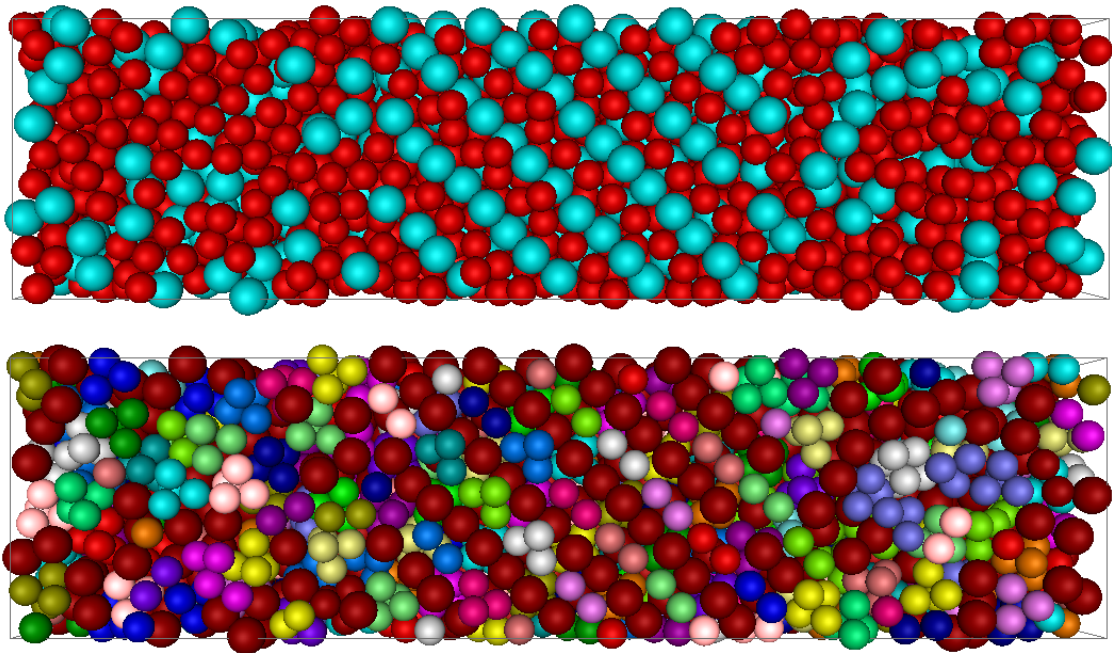


Figure 5.7: Representative final configuration from direct coexistence simulations displaying coexistence between the fluid phase and the Laves crystal of hard tetramers and hard spheres. (top) Overall composition $x = 0.6$ and pressure $\beta P \sigma_L^3 = 15.0$. (bottom) Same as top panel, but with colour coding as to highlight the different tetramers.

Despite the progress in the fabrication of colloidal building blocks, we are unaware, to the best of our knowledge, of experimental realisations of the proposed binary mixture. In order to

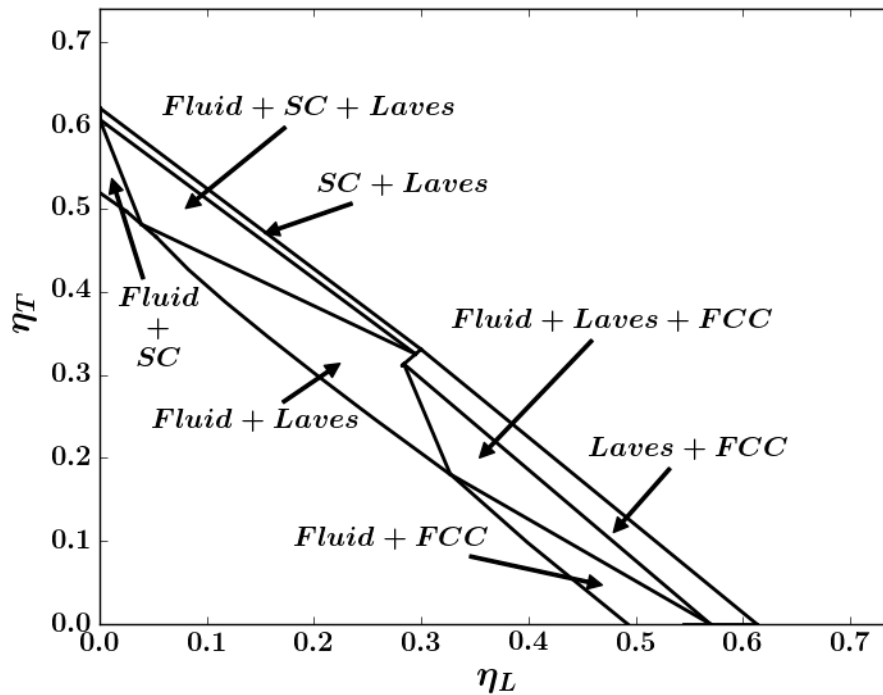


Figure 5.8: Phase diagram of the investigated binary mixture in the packing fraction of tetramers η_T – packing fraction of large spheres η_L representation.

facilitate the comparison with experimental results we additionally convert the phase diagram to the packing fraction of tetramers η_T – packing fraction of spheres η_S representation, the result being shown in Fig. 5.8. The triple points we found in Fig. 5.6 – Fluid + SC + Laves, Fluid + Laves + FCC – transform to triangular areas in this representation. In between the triple points we find the coexistence region between fluid phase and Laves structure, which could be probed experimentally. Note that the triple point SC + Laves + FCC is outside the scanned pressure range and for this reason does not appear in Fig. 5.8. Finally, we also calculate the phase diagram in the chemical potential of the spheres μ_L – chemical potential of the tetramer μ_T representation. While this diagram is not suitable for comparison with experiments, it is instead crucial in order to theoretically address the role of gravity on the presented bulk results, as accomplished in the next section.

5.4 Sedimentation behaviour and stacking diagram

We now study the system while sedimenting under a gravitational field. The phase diagram in the chemical potential of the spheres μ_L – chemical potential of the tetramers μ_T representation is shown in Fig. 5.9, where full black lines represent bulk binodals. At each point on a binodal two phases are in equilibrium with each other.

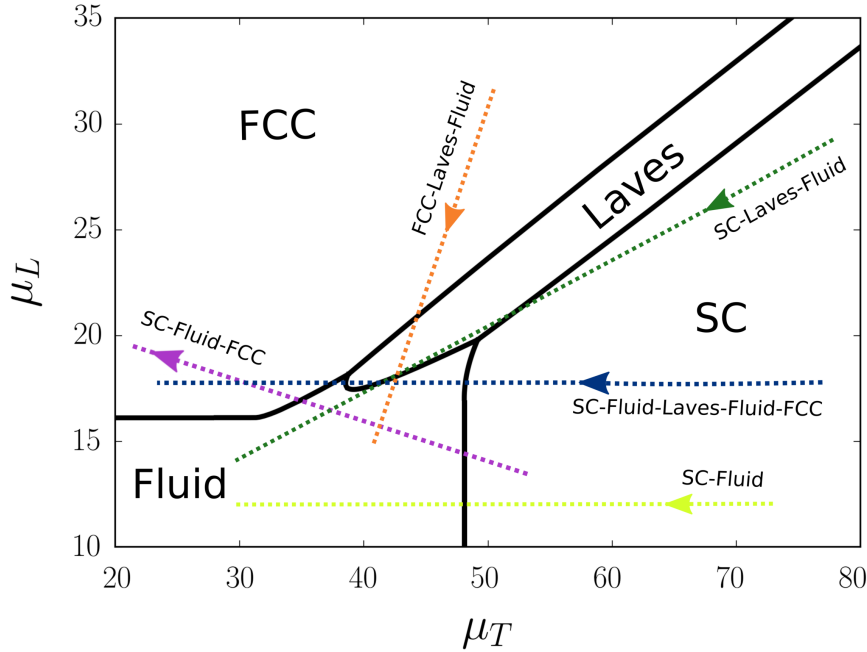


Figure 5.9: Phase diagram of the binary mixture in the chemical potential of large hard spheres μ_L – chemical potential of hard tetramers μ_T representation. The solid lines represent the bulk binodals, and delimit single-phase regions. The phase transitions of the pure system of spheres and the pure system of tetramers are shown by the horizontal and vertical asymptotic extensions of the respective binodals. The coloured dashed lines represent some of the possible phase-stacking sequences in the sediment. The colour code is the same as the one used for the stacking diagram. The arrows on the dashed lines indicate the direction from the bottom to the top of the sediment.

This bulk phase diagram is used as an input for our theory, as discussed in Sec. 5.2.4, in order to calculate the stacking diagram. The different regions in a stacking diagram, each of which represent a unique stacking sequence, are delimited by the following features:

Sedimentation binodal is the locus of all sedimentation paths tangential to the bulk binodal(s). We have five bulk binodals indicating the various coexistences as shown in Fig. 5.9 thus giving five corresponding sedimentation binodals.

Terminal lines which represent sedimentation paths passing through any point where a binodal terminates. Referring to our bulk phase diagram, we have three such terminal points:

1. The triple point where the Laves, fluid and FCC phases coexist.
2. The triple point where the Laves, fluid and SC phases coexist.

3. The triple point where the Laves, FCC and SC phases coexist. In order to locate this point in the plane of chemical potentials, we obtain the FCC-Laves and SC-Laves binodals from simulations until pressures $\beta P \sigma_L^3 = 70$, and we extrapolate the last simulated points until the two binodals meet.

Asymptotic terminal lines appear when the bulk binodal does not terminate at a finite value for one of the chemical potentials, i.e., when the binodal is connected to a phase transition of a one-component system or when, at very high chemical potentials, both pure component crystals approach close packing densities. For example, in our system the fluid-FCC binodal goes asymptotically to the fluid-FCC phase transition of the pure large hard spheres, which is denoted by the $s = 0$ line. In addition, the fluid-hard tetramer SC phase continues in the pure tetramer system, which is at $s = -\infty$ (not shown in figure).

With these features in place, we obtain the corresponding stacking diagram of system of large hard spheres and hard tetramers undergoing sedimentation, shown in Fig. 5.10, with the assumption that both species sediment slowly enough for LDA to apply. The differently coloured regions in Fig. 5.10 represent the different stacking sequences for this binary mixture. We remind the reader that s equals the ratio of the buoyant masses of the spheres to the tetramers, as from Eq. 5.9. A negative s means that one species settles while the other creams up. For the purposes of analysis, in this paper we assume that the tetramers always settle, which means that the buoyant mass of the tetramer species is always positive. Alternatively, if the identity of the settling species is switched, the stacking sequences for the negative s region will simply be reversed. Keeping this in mind, the following observations can be made about the resulting stacking diagram.

1. For negative s , the single species crystal phase formed at the bottom is always the SC phase of tetramers, as is expected.
2. For $0 < s \lesssim 0.45$, the pure component crystal phase is the SC of tetramers, which is also expected because the tetramers have a higher buoyant mass than the spheres and therefore sediment faster.
3. For $s \gtrsim 0.45$, the large spheres form the FCC phase at the bottom of the column. This is counter-intuitive as the spheres have a lower buoyant mass and should sediment less than the tetramers, and it is reminiscent of the ‘‘Brazil-nut effect’’ in binary granular mixtures under shaking, where the large species rises to the top of the smaller one [254, 255]. However, the nature of the two phenomena is different, because the Brazil-nut effect happens under out of equilibrium conditions, while the observed settling behaviour is an equilibrium phenomenon. We also note that Brazil-nut-like effects have been observed – both theoretically and experimentally – in colloidal systems, however involving charged binary mixtures [256, 257].
4. For $s \approx 1$, which means that the buoyant mass of both species are equal, we still observe that the large hard spheres form an FCC crystal at the bottom. This can be understood if we approximate the hard tetramer by a circumscribed sphere with a diameter $\sigma_{\text{eff}} = q(1 + \sqrt{3/2})\sigma_L \simeq 1.83\sigma_L$. We thus find that the tetramers are the larger than the spheres, and hence the system minimises its potential energy by having the smaller species at the bottom.

triple points. Surprisingly, we find a relatively large coexistence region between the fluid and the Laves phase – the structural analogue of the MgCu_2 phase, which may be experimentally accessible. In order to facilitate comparison with experimental parameters, we also converted the phase diagram from the pressure $\beta P \sigma_L^3$ – composition x representation to the packing fraction of tetramers η_T – packing fraction of spheres η_L plane.

Assuming the validity of the local density approximation under relevant experimental conditions for our binary system, we also investigated the sedimentation behaviour by calculating the stacking diagram of this mixture. We observed several stacking sequences, some of which were reminiscent of the “Brazil-nut effect” in binary granular mixtures, while others intriguingly displayed floating phases.

Our results demonstrate a novel self-assembly route towards a photonic crystal, in which the Diamond and the Pyrochlore structures can be assembled in one crystal – the MgCu_2 Laves structure – from a binary mixture of hard spheres and hard tetramers. By selectively burning or dissolving one of the species, either the tetramers or the spheres, the Laves phase can be converted into a diamond lattice or a pyrochlore structure to obtain a photonic crystal with a bandgap in the visible range. We hope that our results will stimulate further experimental and theoretical investigations. In future work, we will address the crystallization kinetics of the proposed self-assembly route, as well as the effect of colloidal epitaxy.

Acknowledgements

I thank T. Dasgupta for her work on the stacking diagram of the investigated mixture, and for the nice collaboration. Furthermore, I thank L. Filion and S. Dussi for fruitful discussions. H. Pattabhiraman, V. Prymidis, and S. Dussi are acknowledged for the critical reading of this manuscript. I gratefully thank G. Fiorucci for her artistic contribution to the figure of the stacking diagram presented in this chapter.

Phase behaviour of a binary mixture of colloidal spheres and icosahedral clusters

Nanoparticles and colloidal particles display a wealth of interesting crystal structures which are suitable for application in, e.g., thermoelectric materials and photovoltaics or in photonics and energy storage, depending on the particle size and material. One particular structure which can be obtained in binary mixtures of nanoparticles is the AB_{13} crystal, in which the small spheres are arranged in an icosahedral fashion. Such a structure can be viewed as being made of large hard spheres and hard icosahedral clusters potentially yielding a plastic colloidal crystal to be used in optoelectronic devices. In this chapter, we employ a binary mixture of hard colloidal spheres and hard icosahedral clusters to study the thermodynamic stability of the AB_{13} crystal. The choice of the particular building blocks is motivated by the recent advances in colloidal synthesis. Our bulk phase diagram shows a number of solid-solid phase coexistence regions, as well as a phase coexistence region between the fluid and the AB_{13} crystal, and between the fluid and a plastic crystal of pure icosahedra. The latter regions are expected to be accessible in sedimentation experiments on the suggested mixture, allowing studies of colloidal plastic crystal phases in real space and real time.

6.1 Introduction

The study of self-assembled structures formed by colloids or nanoparticles (NPs) has a two-fold purpose: first, the resulting crystals may have properties that make them interesting for applications, and second, it may be used to gain insights at a fundamental level into conventional condensed matter topics, such as phase ordering and kinetics [15–17, 259]. Colloids and NPs have provided numerous examples of ordered structures, many of which are isostructural to atomic crystals. For instance, single component systems have been found to form face-centered-cubic (FCC) crystals both in colloids [14] and NPs [260]. More complex arrangements are observed in binary systems, such as lattices isostructural to NaCl, AlB_2 , Cu_3Au , CaB_6 , and AB_{13} [259, 261–266]. Binary NP superlattices open the way to miniaturised transistors, better thermoelectric materials and photovoltaics [259]. Colloidal crystals, instead, can be used as photonic crystals to control visible light, with applications in optical fibres, switches, (bio-)sensing, security, and energy storage [18–29].

Motivated by previous results on binary NP mixtures, and by the increasing number of shapes that – due to advances in chemical synthesis – are available for colloidal self-assembly, we address in this chapter the formation and stability of an AB_{13} superlattice made of spheres and icosahedral clusters of spheres interacting as hard particles. The assumption of hard bodies is reasonable for NP under particular conditions of, e.g., temperature [259]. To understand why the AB_{13} superlattice is particularly interesting from the colloid science perspective, its structure should be considered in more detail. As shown in Fig. 6.3, the 13 small spheres of type B are arranged at the vertices of an icosahedron, including a sphere in the middle. The icosahedra and the large spheres of type A form two interpenetrating simple cubic (SC) structures. Because of the mild anisotropy inherent to the icosahedra, we can expect a crystal involving such a building block to transform into a plastic crystal. A plastic crystal, also known as rotator phase, is a structure with long-range positional order and short-range orientational order, suitable to fabricate materials with tunable optical properties [267]. The prospects of a stable plastic crystal phase in a binary mixture of hard icosahedral clusters and hard spheres motivated us to investigate the phase behaviour of this binary system.

Moreover, studying hard colloidal icosahedral clusters mixed with hard colloidal spheres allows us to test whether or not a colloidal analogue of the regular AB_{13} superlattice is stable in bulk. As we have seen in Ch. 5, this is true for the MgCu_2 Laves phase of tetrahedral clusters and spheres. Here, we wish to explore the same possibility using colloidal icosahedral clusters and colloidal spheres. As already pointed out in Ch. 5, colloidal clusters of spheres are relatively easy to synthesize [234, 235, 237, 239–243], making our investigation directly relevant to future experiments, provided the particles interact predominantly with excluded-volume interactions.

This chapter is organised as follows. We introduce the model and discuss the employed methods in Sec. 6.2. In Sec. 6.3 we present the results on the phase behaviour of the binary mixture of spheres and icosahedra. In Sec. 6.4 we sum up our findings, and outline future research directions.

6.2 Model and methods

6.2.1 Monte Carlo simulations

We investigate a binary mixture of N_S spheres and N_I icosahedra with composition $x = N_S/N$, where $N = N_S + N_I$. The spheres have diameter σ_L , while the beads in the icosahedral clusters have a diameter σ_B . The icosahedra are formed by 12 beads tangential to a central bead of the same size. We neglect fluctuations in the geometrical arrangement of the beads, as well as size polydispersity. The size ratio between a bead in an icosahedron and a sphere is labelled as $q = \sigma_B/\sigma_L$. Since the AB_{13} phase of an ordinary binary hard-sphere mixture achieves its highest packing fraction for $q \sim 0.58$, we employ this value in our work. All interactions are assumed to be hard-sphere-like, meaning that the objects do not interpenetrate. Thus, spheres cannot approach each other closer than σ_L , beads of different icosahedra cannot approach each other closer than σ_B , and spheres and icosahedral beads cannot approach closer than $\sigma_{LB} = (\sigma_L + \sigma_B)/2$. A model of the icosahedron showing the face, edge, and vertex orthogonal projections, as well as the size difference between the two investigated building blocks, is shown in Fig. 6.1.

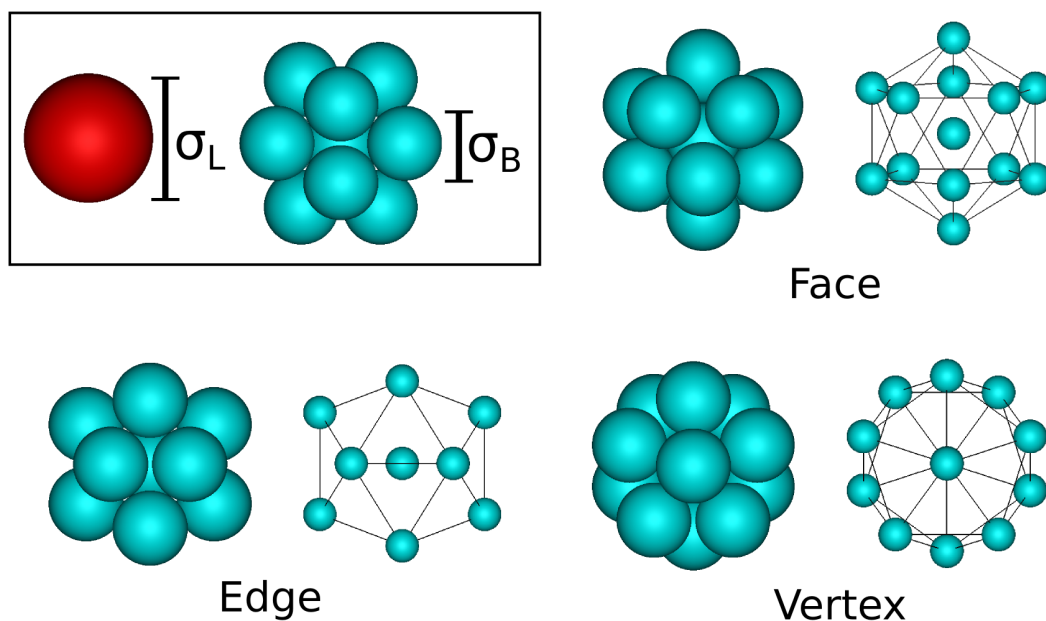


Figure 6.1: (inside the box) Building blocks of the investigated binary mixture: hard sphere of diameter σ_L in red, hard icosahedral cluster in blue, where each bead has a diameter σ_B . The size ratio between the spheres and the beads $q = \sigma_B/\sigma_L$ is fixed to 0.58. (outside the box) Main orthogonal projections of the icosahedron, in both space filling and ball and stick model: face on, vertex on, and edge on.

We study the phase behaviour of the binary mixture by Monte Carlo (MC) simulations in the isobaric-isothermal ensemble, where the number of particles of each species, the pressure and the temperature are fixed. Hence, the relevant thermodynamic quantities are N_S, N_I, P, T . The pressure P is measured in reduced units as $\beta P \sigma_L^3$ with $\beta = 1/k_B T$, k_B Boltzmann's constant, and T the system temperature. The dimensionless number density is $\rho \sigma_L^3 = N \sigma_L^3/V$, where

V represents the volume of the simulation box. The packing fraction is defined as $\eta = \gamma\rho\sigma_L^3$, with $\gamma = \pi[x + 13q^3(1-x)]/6$. We sample the configurational phase space with displacement moves for spheres and icosahedra, rotational moves for icosahedra, and volume moves for the simulation box. The acceptance rate for translational and rotational moves is 30%, while it is set to 20% for the volume moves. We define an MC step (MCS) as N attempted translations or rotations, and one volume move of the simulation box. The simulation runs consist of at least 5×10^6 MCS. To study non-cubic crystal structures, we also employ NPT simulations where the lattice vectors of the box are free to fluctuate, in order to remove any additional stress from the crystal phase [87, 88]. We analyse the simulation results by calculating the radial distribution functions (RDF) for each species $g_{\alpha,\alpha}(r)$, and the orientational scatter plot for the icosahedra. For each composition of large spheres x , the equation of state (EOS) is computed by means of compression and expansion runs. For the compression runs, the starting configuration is a disordered fluid of $N_S = xN$ spheres and $N_I = (1-x)N$ icosahedra. For the expansion runs, crystalline structures of selected composition provide the initial configuration, as explained in the following section.

6.2.2 Crystalline structures

We employ three different crystalline structures to provide the system initial configuration at composition $x = 0, 0.5$ and 1.

For $x = 0$, we have a single component system of icosahedra, whose close-packed configuration can be found by employing the Floppy Box Monte Carlo (FBMC) method [87, 88]. In the FBMC, we simulate only a few particles, in order to mimic a unit cell, and additionally we let the box shape fluctuate. By running several FBMC simulations, one can identify the candidate crystal structure to use as starting configuration for the simulations in the isobaric-isothermal ensemble. For the case of pure icosahedra, the FBMC method yields a triclinic Bravais lattice type with maximum packing fraction $\eta = 0.652$. This structure is hereafter labelled as TCI, and is shown in Fig. 6.2.

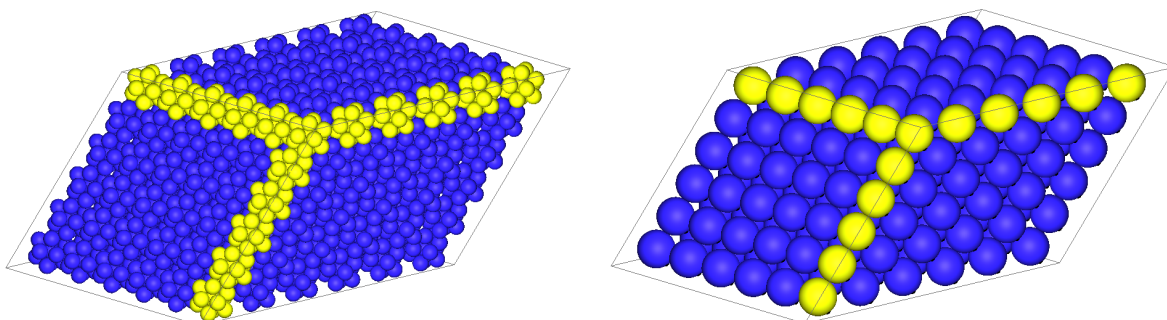


Figure 6.2: Illustration of the TCI crystal structure. Particles near the three main edges of the box are coloured in yellow to highlight the box shape. The purple colour refers to the orientation of the north pole of the icosahedra, and it is the same for all the particles in the crystal. (left) Representation showing the icosahedral clusters. (right) Representation showing spheres at the centre of mass of the clusters, having the same volume as the icosahedra.

For $x = 0.5$, we use a close packed configuration of the AB_{13} structure for a binary mixture of hard spheres at the chosen size ratio $q = 0.58$, however we substitute an icosahedron for every 13 small spheres. The resulting structure – shown in Fig. 6.3 – consists of two interpenetrating simple cubic lattices, one of the spheres, and one of the icosahedra. The orientation of the icosahedral clusters is estimated by a rigid transformation of the bead positions in the reference frame to the bead positions in the crystal. This procedure yields two different orientations, which are also shown by two different colours in the middle and right panel of Fig. 6.3.

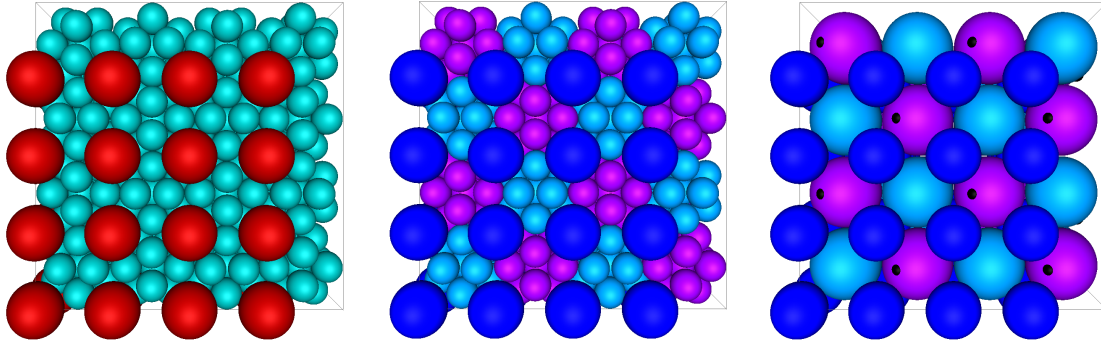


Figure 6.3: Illustration of the AB_{13} crystal structure. (left) Representation showing all the spheres as separate objects. The large spheres are coloured red and the small spheres are coloured cyan. (middle) Beads of the icosahedral clusters grouped together, as a whole object. (right) Representation showing the centre of mass and orientation of the building blocks. In the middle and right panels, the colour code refers to the orientation of the north pole of the particles with respect to the z -axis. The large spheres are coloured dark blue by convention. Additionally, in the right panel the north pole is also shown as a small black spot on the spheres representing the icosahedra.

For $x = 1.0$, we pick the FCC of large spheres, which is the thermodynamically stable crystal phase [250].

6.2.3 Free-energy calculations

We measure the EOS using compression and expansion runs in N_S, N_I, P, T simulations. To obtain analytical expressions for the S, we fit the simulation results to

$$\frac{\gamma\beta P}{\eta} = 1 + \sum_{i=1}^n a_i \eta^i \quad (6.1)$$

for the fluid phase, and

$$\frac{\gamma\beta P}{\eta^2} = \sum_{i=0}^m b_i \eta^i \quad (6.2)$$

for the plastic crystal and crystal phases. Here, the typical value of n is 12, while m ranges between 3 – 6. The fits eventually allow for the evaluation of the Gibbs free energy at a specific pressure and composition $g(P, x)$, provided one reference value $f(\eta_0, x)$ of the Helmholtz free energy is known, according to

$$g(P, x) = f(\eta_0, x) + \gamma \int_{\eta_0}^{\eta} d\eta' \frac{\beta P(\eta', x)}{\eta'^2} + \frac{\beta P}{\rho} \quad (6.3)$$

To calculate the Helmholtz free energy of the crystal phases at a reference density, we use the Einstein crystal method which tethers the particles to the lattice site by a spring of constant λ , as described in Ch. 5. However an additional integration step is needed in order to deal with the plastic crystal phases since the particles in these phases can still bump into each other by rotations even if their positions are fixed. To this end, we employ the method suggested in Ref. [268], which allows for a continuous transition from a non interacting system to a plastic crystal. We introduce soft-to-hard interaction potentials among all the particles in the system

$$\beta U_{\text{soft}}^{\text{II}}(\mathbf{x}^{N_I}; \gamma) = \sum_{i=1}^{N_I} \sum_{j>i}^{N_I} \sum_{\eta, \mu}^{13} \beta \varphi(|\mathbf{r}_{i\eta} - \mathbf{r}_{j\mu}|, \sigma_B; \gamma) \quad (6.4)$$

$$\beta U_{\text{soft}}^{\text{IS}}(\mathbf{x}^{N_I}, \mathbf{r}^{N_S}; \gamma) = \sum_{i=1}^{N_I} \sum_{j=1}^{N_S} \sum_{\eta}^{13} \beta \varphi(|\mathbf{r}_{i\eta} - \mathbf{r}_j|, \sigma_{LB}; \gamma) \quad (6.5)$$

$$\beta U_{\text{soft}}^{\text{SS}}(\mathbf{r}^{N_S}; \gamma) = \sum_{i=1}^{N_S} \sum_{j>i}^{N_S} \beta \varphi(|\mathbf{r}_i - \mathbf{r}_j|, \sigma_L; \gamma) \quad (6.6)$$

$$\beta U_{\text{soft}}^{\text{sys}}(\gamma) = \beta U_{\text{soft}}^{\text{II}} + \beta U_{\text{soft}}^{\text{IS}} + \beta U_{\text{soft}}^{\text{SS}} \quad (6.7)$$

with

$$\beta \varphi(r, \sigma, \gamma) = \begin{cases} \gamma (1 - A(r/\sigma)^2) & \text{if } r < \sigma \\ 0 & \text{otherwise} \end{cases} \quad (6.8)$$

where $\mathbf{x}^{N_I} = \{\mathbf{r}, \mathcal{O}\}^{N_I}$ denotes the positions and the orientations of the icosahedra, \mathbf{r}^{N_S} the positions of the large spheres, $\mathbf{r}_{i\eta}$ the position of bead η of icosahedron i , and γ is the integration parameter. We have set $A = 0.9$ in our calculations following Refs. [269, 270]. We start at a value of $\gamma_{\text{max}} = 200$ where the particles behave as hard objects. Then, we turn on the translational springs that tether the particles to the respective lattice sites by increasing λ from 0 to λ_{max} . Next, we decrease γ to zero so that the system becomes an ideal Einstein crystal. The free energy F of a plastic crystal phase is then given by

$$\beta F(N_i, N_s, V, T) = \beta F_{\text{Einst}}(N_i, N_s, V, T) - \int_0^{\lambda_{\text{max}}} d\lambda \left\langle \frac{\partial \beta F}{\partial \lambda} \right\rangle_{\gamma_{\text{max}}} + \int_0^{\gamma_{\text{max}}} d\gamma \left\langle \frac{\partial \beta F}{\partial \gamma} \right\rangle_{\lambda_{\text{max}}} \quad (6.9)$$

with $\langle \partial \beta F / \partial \gamma \rangle = \langle \beta U_{\text{soft}}^{\text{sys}}(\gamma) / \gamma \rangle$ and $\langle \partial \beta F / \partial \lambda \rangle = \left\langle \sum_{i=1}^N (\mathbf{r}_i - \mathbf{r}_{i,0})^2 / \sigma_L^2 \right\rangle$, where \mathbf{r}_i denotes the centre-of-mass position of particle i and $\mathbf{r}_{i,0}$ its respective ideal lattice position. Note that this last term does not distinguish between icosahedra and spheres, but only takes into account the positions of the centre of mass. The Helmholtz free energy of the noninteracting plastic Einstein crystal reads

$$\beta F_{\text{Einst}}(\lambda_{\text{max}}) = -\frac{3(N-1)}{2} \ln \left(\frac{\pi}{\lambda_{\text{max}}} \right) + N \ln \left(\frac{\Lambda_r^3 \Lambda_r}{\sigma_L^3} \right) + \log \left(\frac{\sigma_L^3}{VN^{1/2}} \right) \quad (6.10)$$

where $\Lambda_{t(r)}$ represents the translational (rotational) de Broglie wavelength.

6.3 Bulk phase behaviour

In this section, we present selected equations of state (EOS) and discuss our results for the bulk phase diagram of a binary mixture of hard spheres and hard icosahedra. In general, we find hysteresis loops in the equations of state as obtained from compression and expansion runs.

6.3.1 EOS of pure hard icosahedra, $x=0$

The EOS of a single component system of hard icosahedra is shown in Fig. 6.4, where open circles represent MC data and the solid lines are fits using Eq. 6.1 and 6.2.

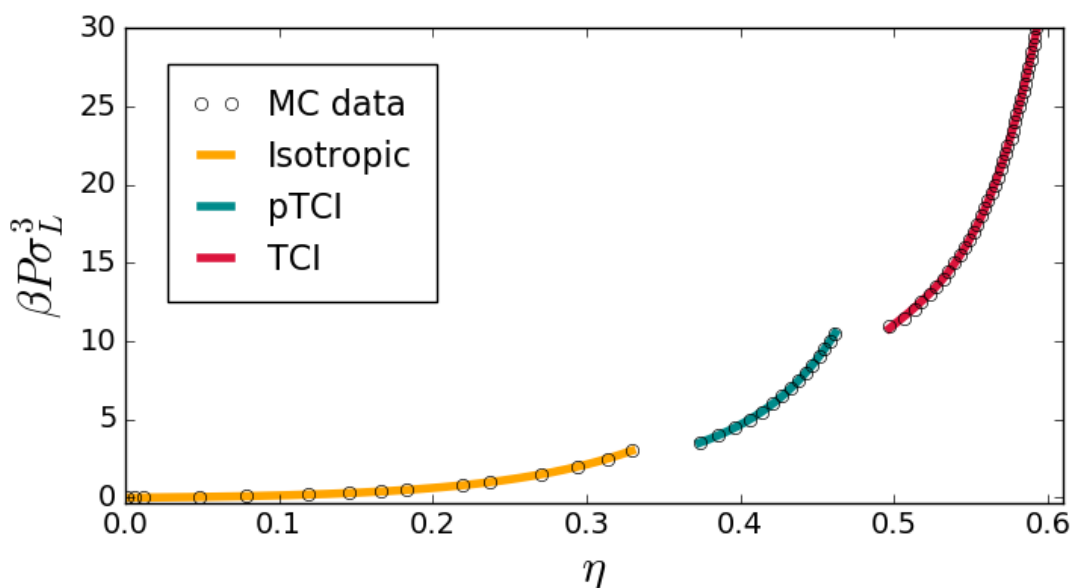


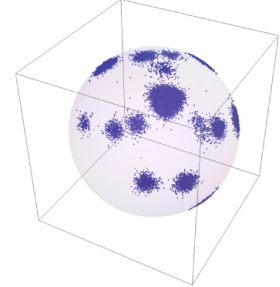
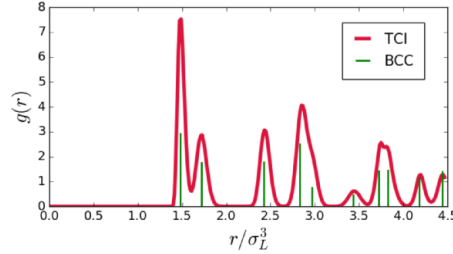
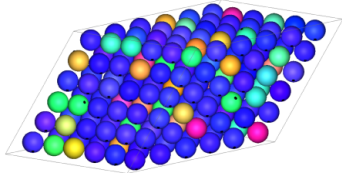
Figure 6.4: The reduced pressure $\beta P \sigma_L^3$ as a function of packing fraction η for a system of hard icosahedra, i.e., sphere composition $x = 0$. Two structural transitions can be identified: the crystal to plastic crystal at a reduced pressure of $\beta P \sigma_L^3 \sim 11.0$, and the plastic crystal to isotropic fluid at a reduced pressure of $\beta P \sigma_L^3 \sim 3.5$.

We observe two structural transitions signalled by discontinuities in the EOS. Going from high pressures towards low pressures, first the triclinic lattice TCI transforms into a plastic crystal (pTCI), then the plastic phase melts into an isotropic fluid (I). The box shape in the isotropic phase relaxes to a cuboid, meaning that there is no preferential direction in this phase.

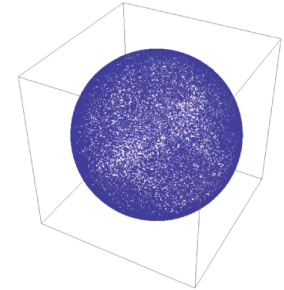
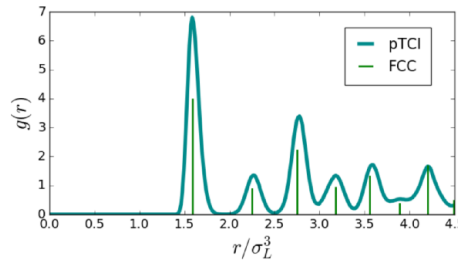
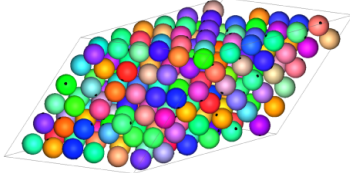
Typical configurations of the TCI, pTCI, and I phases are shown in Fig. 6.5 from top to bottom, respectively, and are complemented with the radial distribution function (RDF) using the centre-of-masses of the icosahedral clusters, and with the spherical scatter plot of the particle orientation. The RDF of the icosahedra is crystalline in the case of TCI and pTCI, but is fluid-like in the I phase. The structure of TCI is consistent with that of a body-centred-cubic (BCC) crystal, whereas the structure of pTCI is consistent with an FCC, as shown by the vertical lines corresponding to the major peaks of the BCC and FCC crystals. The TCI-pTCI transition is found to be first order from additional compression and expansion runs with a much finer pressure step ($\beta \Delta P \sigma_L^3 = 0.05$) than what was used in order to scan the entire EOS ($\beta \Delta P \sigma_L^3 =$

0.5). Regarding the orientational correlations, we observe an isotropic sphere coverage for the I and the pTCI phases, while clear spots are found for the crystal TCI phase. These measurements confirm that the plastic crystal phase has positional order, but lacks orientational order.

$$\beta P \sigma_L^3 = 12.0$$



$$\beta P \sigma_L^3 = 9.0$$



$$\beta P \sigma_L^3 = 2.0$$

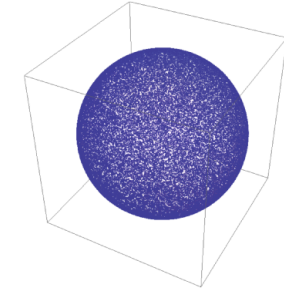
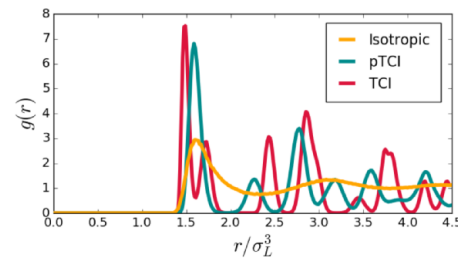
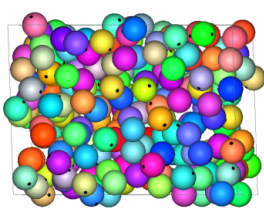


Figure 6.5: Analysis of the phases of hard icosahedra obtained at different pressures. The typical configurations display only the position of the centre of mass of the clusters, with a sphere having the same volume as the icosahedral clusters. The colour code refers to the orientation of the north pole of the icosahedra. (top) Crystal phase (TCI) at $\beta P \sigma_L^3 = 12.0$, with BCC-like peaks in the RDF as shown by the vertical lines that correspond to the peaks of an ideal BCC, and well defined orientational correlations. The configuration shows that all the icosahedra retain a similar orientation. (middle) Plastic crystal phase (pTCI) at $\beta P \sigma_L^3 = 9.5$, with FCC-like peaks in the RDF and low orientational order. The vertical lines denote the peaks of an ideal FCC lattice. The configuration and the orientational scatter plot show that in this phase the icosahedra are freely changing their orientations. (bottom) Isotropic phase (I) at $\beta P \sigma_L^3 = 2.0$, with low positional and orientational order. In this last case, the RDF is shown in comparison with the ordered phases.

6.3.2 EOS of the equimolar mixture of hard icosahedra and hard spheres, $x=0.5$

The EOS for the equimolar mixture of hard spheres and hard icosahedra is shown in Fig. 6.6, where open circles represent MC data and the solid lines are the fit results. Upon decreasing

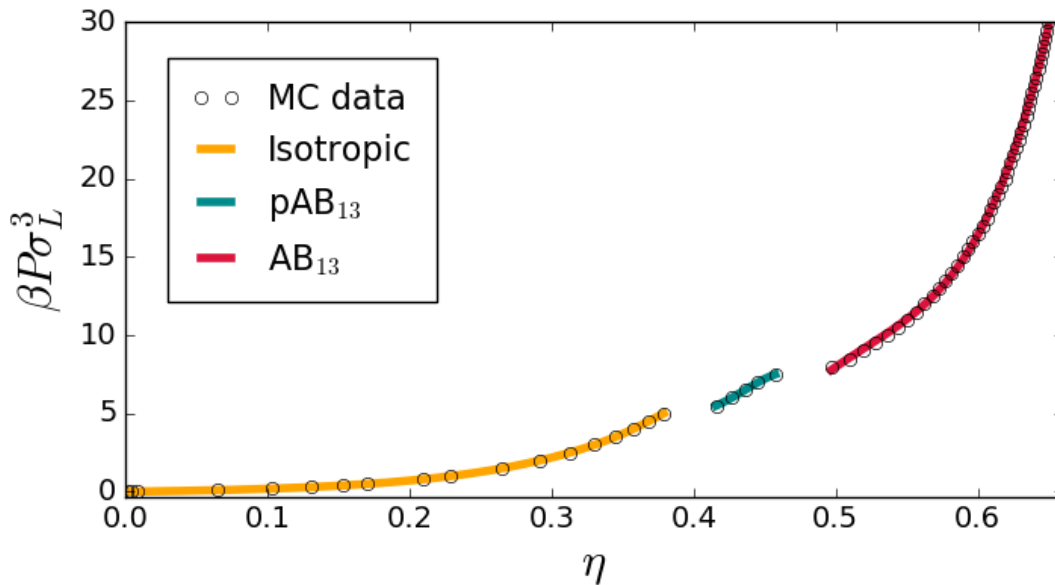


Figure 6.6: The reduced pressure $\beta P\sigma_L^3$ as a function of packing fraction for an equimolar mixture of hard spheres and hard icosahedra, i.e., sphere composition $x = 0.5$. Two structural transitions can be identified: the crystal to the plastic crystal (AB_{13} - pAB_{13}) at a reduced pressure of $\beta P\sigma_L^3 \sim 8.0$, and the plastic crystal to isotropic fluid (pAB_{13} -I) at a reduced pressure of $\beta P\sigma_L^3 \sim 5.5$.

the pressure we again find discontinuities in the EOS. The initial AB_{13} crystal transforms into a plastic crystal (pAB_{13}), which then melts into an isotropic phase (I). In Fig. 6.7 we present a structural analysis comparing typical configurations, RDFs, and orientational scatter plots, which reveals that – in contrast with the pTCI rotator phase of pure icosahedra – the pAB_{13} phase retains the same structure as that of the parent solid phase AB_{13} . Indeed, both RDFs are consistent with a SC structure, where the RDF is calculated only between icosahedral clusters. The orientational correlation plots display a similar behaviour as seen at $x = 0$, showing low orientational order in the isotropic and plastic crystal phase, but high orientational order in the crystal phase.

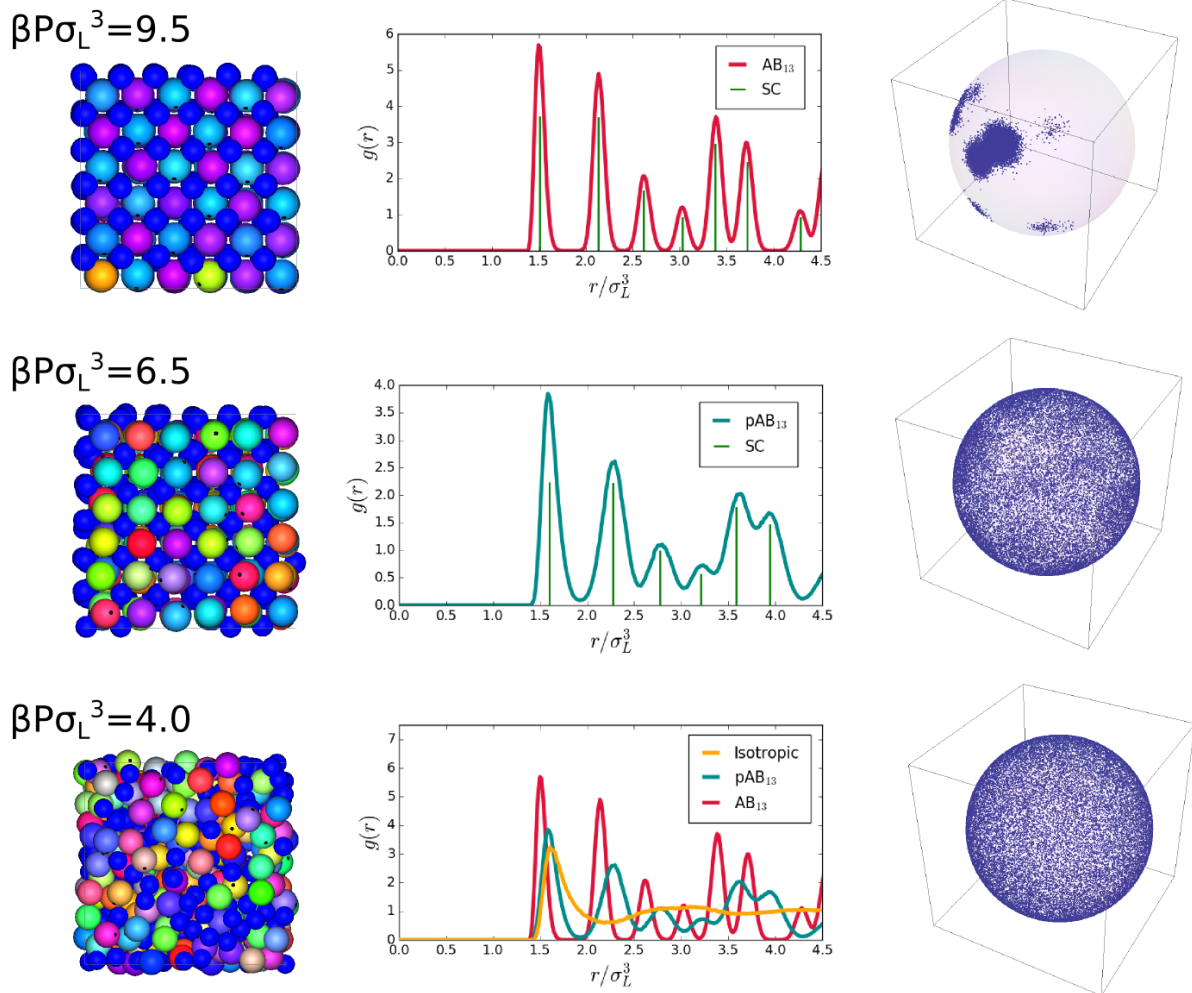


Figure 6.7: Analysis of the stable bulk phases of an equimolar mixture of hard spheres and hard icosahedra for varying pressures. In the typical configurations, we represent the icosahedra by spheres with the same volume as the icosahedral clusters. The colour code refers to the orientation of the north pole of the icosahedra, while the actual hard spheres are coloured in dark blue. (top) AB₁₃ crystal phase at $\beta P \sigma_L^3 = 9.5$, with SC-like peaks in the RDF as shown by the perfect match with the vertical lines corresponding to the major peaks of an ideal SC lattice, and well defined orientational correlations. The configuration shows that all the icosahedra retain a similar orientation. (middle) pAB₁₃ plastic crystal phase at $\beta P \sigma_L^3 = 6.5$, also with SC-like peaks in the RDF and low orientational order. In this case, while the positions are still well-defined, the orientations of the icosahedra are uncorrelated. (bottom) Isotropic phase at $\beta P \sigma_L^3 = 4.0$, with low positional and orientational order. In this last case, the RDF is shown in comparison with the ordered phases.

6.3.3 EOS of pure hard spheres, $x=1$

For the EOS of the single component system of hard spheres, we use well-known analytical results which relate the compressibility factor $\mathcal{Z} = \beta P / \rho$ to the system packing fraction η . For the fluid phase, we employ the Carnahan-Starling equation of state [271]

$$\mathcal{Z} = \frac{1 + \eta + \eta^2 - \eta^3}{(1 - \eta)^3} \quad (6.11)$$

while for the solid phase we make use of the empirical equation of state for the FCC crystal by Speedy [272]

$$\mathcal{Z} = \frac{3}{1 - y} - \frac{a(y - b)}{y - c} \quad (6.12)$$

where $y = \rho \sigma_L^3 / \sqrt{2}$ is the dimensionless density relative to close packing, and $a = 0.5921$, $b = 0.7072$, and $c = 0.601$ are fit parameters for the FCC crystal. The bulk coexistence pressure of the fluid-solid transition in hard spheres is known to be $\beta P \sigma_L^3 = 11.54$ [252].

6.3.4 Bulk phase diagram

We performed Gibbs free-energy calculations, according to the procedure outlined in Sec. 6.2.3, in order to draw the phase diagram of the system under investigation in the pressure $\beta P \sigma_L^3$ – composition of large sphere x representation. The resulting phase diagram is shown in Fig. 6.8.

For sufficiently high pressure, we find either a phase coexistence region between the TCI phase at $x = 0$ and the AB_{13} crystal phase at $x = 0.5$ at $\beta P \sigma_L^3 > 11.10$, or a phase coexistence region between the AB_{13} at $x = 0.5$ and the pure FCC phase at $x = 1$ for $\beta P \sigma_L^3 > 12.22$. For pressures below $\beta P \sigma_L^3 < 11.10$ and $x = 0$, the pTCI crystal becomes stable over the TCI, and opens up a region of phase coexistence with the AB_{13} crystal.

We now turn our attention to the different fluid-solid coexistence regions. For sphere composition $x < 0.67$ and pressures $\beta P \sigma_L^3 \in [4.71, 9.20]$, the fluid phase is in coexistence with the pTCI of hard icosahedra. For pressures below $\beta P \sigma_L^3 < 12.22$ and $x = 0.5$, we always find the AB_{13} crystal to be more stable than the plastic p AB_{13} . This gives rise to a pocket of phase coexistence between the AB_{13} solid and the fluid phase, which extends until $\beta P \sigma_L^3 = 9.20$. We find two triple points, namely the pTCI- AB_{13} -Fluid at pressure $\beta P \sigma_L^3 = 9.20$, and the AB_{13} -Fluid-FCC at pressure $\beta P \sigma_L^3 = 12.22$.

Especially the regions of coexistence between the isotropic and the (plastic-)crystalline phases are of interest for experiments. In fact, these regions should be observed in bulk self-assembly experiments, provided all the interactions between the building blocks can be mapped onto a hard potential.

6.4 Conclusions

We have investigated the phase behaviour of a binary mixture of colloidal hard spheres and hard icosahedral clusters. By using MC simulations in the isobaric-isothermal ensemble with

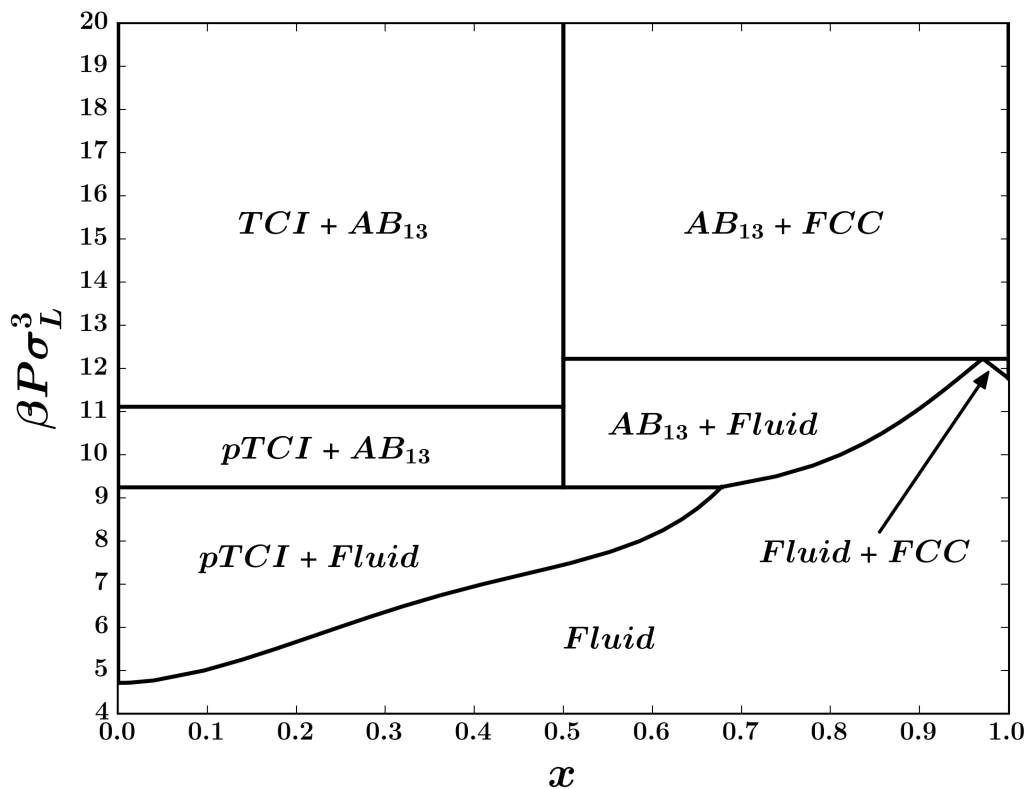


Figure 6.8: Phase diagram of a binary mixture of hard spheres and hard icosahedra in the pressure $\beta P \sigma_L^3$ –sphere composition x representation. Besides the different solid-solid phase coexistence regions, we also find coexistence between the fluid phase and the pTCI solid, and between the fluid phase and the AB_{13} phase. The plastic p AB_{13} phase is always metastable.

and without variable box shape, we mapped out the phase diagram of the mixture in the pressure $\beta P \sigma_L^3$ –sphere composition x representation.

For high pressures, we found solid-solid demixing transitions between the TCI of hard icosahedra and the AB_{13} crystal of spheres and icosahedra, as well as demixing between the AB_{13} and the FCC of hard spheres.

For intermediate pressures and composition $x < 0.5$, we found that the plastic crystal of hard icosahedra pTCI is in coexistence with the AB_{13} and the fluid phase. For composition $x > 0.5$ the fluid phase is in coexistence with the AB_{13} or the FCC or pure hard spheres.

The observed pockets of coexistence of the isotropic fluid phase with the solid phases, either plastic or fully crystalline, suggest that it is feasible to self-assemble such structures from spherical and icosahedral colloidal building blocks. Our findings show potential impact of such colloidal building blocks in, e.g., photonics. Moreover, our work sheds light on the role of orientational entropy in stabilising a richer variety of structures than it is possible with binary hard-sphere mixtures. We hope that our results will stimulate further experimental and theoretical investigations on these mixtures. Further research directions include studying the effect of gravity on the presented mixture and constructing a stacking diagram similarly to what was shown in Ch. 5, as well as investigating the kinetic pathways of crystal formation.

Acknowledgements

I would like to thank S. Dussi, and H. Pattabhiraman for fruitful discussions. N. Tasios is acknowledged for providing the close-packed configuration of icosahedral clusters via the FBMC method. S. Dussi is further acknowledged for independently confirming some of the EOS included in this chapter. H. Pattabhiraman, V. Prymidis, and S. Dussi are gratefully acknowledged for a critical reading of this chapter.

References

- [1] P. G. de Gennes, *Soft matter*. Rev. Mod. Phys., 64:645–648, 1992.
- [2] A. D. McNaught. *IUPAC compendium of chemical terminology*. Blackwell Science Inc. (Hoboken), 2nd edition, 1997.
- [3] T. Graham, *Liquid diffusion applied to analysis*. Phil. Trans. R. Soc. London, 151:183, 1861.
- [4] R. Brown, *A brief account of microscopical observations made in the months of June, July and August 1827 on the particles contained in the pollen of plants; and on the general existence of active molecules in organic and inorganic bodies*. Phil. Mag., 4:161, 1828.
- [5] A. Einstein, *Über die von der molekularkinetischen theorie der wärme geforderte bewegung von in ruhenden flüssigkeiten suspendierten teilchen*. Annalen der Physik, 322(8):549–560, 1905.
- [6] W. Sutherland, *A dynamical theory of diffusion for non-electrolytes and the molecular mass of albumin*. Phil. Mag., 9:781, 1905.
- [7] J. Barnes. *The Presocratic Philosophers*. London and New York: Routledge, 1982.
- [8] G. Reale. *A History of Ancient Philosophy I: From the Origins to Socrates*. SUNY, 1987.
- [9] G. Reale. *A History of Ancient Philosophy III: Systems of the Hellenistic Age*. SUNY, 1985.
- [10] J. E. Kirkwood. *Phase Transformations in Solids*. ed. R. Smoluchowski, J. E. Mayer and W.E. Weyl. Wiley, 1951.
- [11] M. N. Rosenbluth and A. W. Rosenbluth, *Further results on monte carlo equations of state*. The Journal of Chemical Physics, 22(5):881–884, 1954.
- [12] W. W. Wood and J. D. Jacobson, *Preliminary results from a recalculation of the monte carlo equation of state of hard spheres*. The Journal of Chemical Physics, 27(5):1207–1208, 1957.
- [13] B. J. Alder and T. E. Wainwright, *Phase transition for a hard sphere system*. The Journal of Chemical Physics, 27(5):1208–1209, 1957.
- [14] P. N. Pusey and W. van Megen, *Phase behaviour of concentrated suspensions of nearly hard colloidal spheres*. Nature, 320(6060):340–342, 1986.
- [15] V. J. Anderson and H. N. W. Lekkerkerker, *Insights into phase transition kinetics from colloid science*. Nature, 416(6883):811–815, 2002.
- [16] P. J. Lu and D. A. Weitz, *Colloidal particles: Crystals, glasses, and gels*. Annual Review of Condensed Matter Physics, 4(1):217–233, 2013.
- [17] B. Li, D. Zhou, and Y. Han, *Assembly and phase transitions of colloidal crystals*. Nature Reviews Materials, 1:15011, 2016.
- [18] A. Stein, B. E. Wilson, and S. G. Rudisill, *Design and functionality of colloidal-crystal-templated materials-chemical applications of inverse opals*. Chem. Soc. Rev., 42:2763–2803, 2013.
- [19] G. von Freymann, V. Kitaev, B. V. Lotsch, and G. A. Ozin, *Bottom-up assembly of photonic crystals*. Chem. Soc. Rev., 42:2528–2554, 2013.
- [20] H. Cong, B. Yu, J. Tang, Z. Li, and X. Liu, *Current status and future developments in preparation and application of colloidal crystals*. Chem. Soc. Rev., 42:7774–7800, 2013.
- [21] J. Xu and Z. Guo, *Biomimetic photonic materials with tunable structural colors*. Journal of Colloid and Interface Science, 406:1 – 17, 2013.

- [22] J. Zhang, Z. Sun, and B. Yang, *Self-assembly of photonic crystals from polymer colloids*. *Current Opinion in Colloid & Interface Science*, 14(2):103 – 114, 2009.
- [23] C. López, *Materials aspects of photonic crystals*. *Advanced Materials*, 15(20):1679–1704, 2003.
- [24] J. F. Galisteo-López, M. Ibisate, R. Sapienza, L. S. Froufe-Pérez, Á. Blanco, and C. López, *Self-assembled photonic structures*. *Advanced Materials*, 23(1):30–69, 2011.
- [25] J. Ge and Y. Yin, *Responsive photonic crystals*. *Angewandte Chemie International Edition*, 50(7):1492–1522, 2011.
- [26] S. Furumi, H. Fudouzi, and T. Sawada, *Self-organized colloidal crystals for photonics and laser applications*. *Laser & Photonics Reviews*, 4(2):205–220, 2010.
- [27] D. K. Cullen, Y. Xu, D. V. Reneer, K. D. Browne, J. W. Geddes, S. Yang, and D. H. Smith, *Color changing photonic crystals detect blast exposure*. *NeuroImage*, 54:S37 – S44, 2011.
- [28] H. S. Lee, T. S. Shim, H. Hwang, S.-M. Yang, and S.-H. Kim, *Colloidal photonic crystals toward structural color palettes for security materials*. *Chemistry of Materials*, 25(13):2684–2690, 2013.
- [29] I. B. Burgess, L. Mishchenko, B. D. Hatton, M. Kolle, M. Lončar, and J. Aizenberg, *Encoding complex wettability patterns in chemically functionalized 3D photonic crystals*. *Journal of the American Chemical Society*, 133(32):12430–12432, 2011.
- [30] J. V. Sanders, *Colour of precious opal*. *Nature*, 204(4964):1151–1153, 1964.
- [31] J. W. Galusha, L. R. Richey, J. S. Gardner, J. N. Cha, and M. H. Bartl, *Discovery of a diamond-based photonic crystal structure in beetle scales*. *Phys. Rev. E*, 77:050904, 2008.
- [32] S. Yoshioka and S. Kinoshita. *Effect of macroscopic structure in iridescent color of the peacock feathers*. In *Forma*, volume 17(2), pages 169–181. Scipress, 2002.
- [33] J. Zi, X. Yu, Y. Li, X. Hu, C. Xu, X. Wang, X. Liu, and R. Fu, *Coloration strategies in peacock feathers*. *Proceedings of the National Academy of Sciences*, 100(22):12576–12578, 2003.
- [34] A. R. Parker, *515 million years of structural colour*. *Journal of Optics A: Pure and Applied Optics*, 2(6):R15, 2000.
- [35] S. Wickham, L. Poladian, M. Large, and P. Vukusic. *Control of iridescence in natural photonic structures: the case of butterfly scales*. In M. Large, editor, *Optical Biomimetics*, Woodhead Publishing Series in Electronic and Optical Materials, pages 147 – 176e. Woodhead Publishing, 2012.
- [36] J. Zhang, E. Luijten, and S. Granick, *Toward design rules of directional janus colloidal assembly*. *Annual Review of Physical Chemistry*, 66(1):581–600, 2015.
- [37] S. C. Glotzer and M. J. Solomon, *Anisotropy of building blocks and their assembly into complex structures*. *Nature Materials*, 6:557, 2007.
- [38] J. Du and R. K. O’Reilly, *Anisotropic particles with patchy, multicompartment and janus architectures: preparation and application*. *Chem. Soc. Rev.*, 40:2402–2416, 2011.
- [39] K. J. Lee, J. Yoon, and J. Lahann, *Recent advances with anisotropic particles*. *Current Opinion in Colloid & Interface Science*, 16(3):195 – 202, 2011.
- [40] S. Sacanna, D. J. Pine, and G.-R. Yi, *Engineering shape: the novel geometries of colloidal self-assembly*. *Soft Matter*, 9:8096–8106, 2013.
- [41] V. R. Dugyala, S. V. Daware, and M. G. Basavaraj, *Shape anisotropic colloids: synthesis, packing behavior, evaporation driven assembly, and their application in emulsion stabilization*. *Soft Matter*, 9:6711–6725, 2013.

- [42] S. Sacanna and D. J. Pine, *Shape-anisotropic colloids: Building blocks for complex assemblies*. Current Opinion in Colloid & Interface Science, 16(2):96–105, 2011.
- [43] M. J. Solomon, *Directions for targeted self-assembly of anisotropic colloids from statistical thermodynamics*. Current Opinion in Colloid & Interface Science, 16(2):158 – 167, 2011.
- [44] A. Kuijk, A. van Blaaderen, and A. Imhof, *Synthesis of monodisperse, rodlike silica colloids with tunable aspect ratio*. J. Am. Chem. Soc., 133:2346, 2011.
- [45] A. Kuijk, D. V. Byelov, A. V. Petukhov, A. van Blaaderen, and A. Imhof, *Phase behavior of colloidal silica rods*. Faraday Discuss., 159:181–199, 2012.
- [46] M. Ozaki, S. Kratochvil, and E. Matijević, *Formation of monodispersed spindle-type hematite particles*. Journal of Colloid and Interface Science, 102(1):146 – 151, 1984.
- [47] F. M. van der Kooij, K. Kassapidou, and H. N. W. Lekkerkerker, *Liquid crystal phase transitions in suspensions of polydisperse plate-like particles*. Nature, 406(6798):868–871, 2000.
- [48] F. M. van der Kooij and H. N. W. Lekkerkerker, *Formation of nematic liquid crystals in suspensions of hard colloidal platelets*. The Journal of Physical Chemistry B, 102(40):7829–7832, 1998.
- [49] Y. Sun and Y. Xia, *Shape-controlled synthesis of gold and silver nanoparticles*. Science, 298(5601):2176–2179, 2002.
- [50] E. Greyson, J. Barton, and T. Odom, *Tetrahedral zinc blende tin sulfide nano- and microcrystals*. Small, 2(3):368–371, 2006.
- [51] J. Henzie, M. Grünwald, A. Widmer-Cooper, P. L. Geissler, and P. Yang, *Self-assembly of uniform polyhedral silver nanocrystals into densest packings and exotic superlattices*. Nat. Mater., 11(2):131–137, 2012.
- [52] L. Manna, D. J. Milliron, A. Meisel, E. C. Scher, and A. P. Alivisatos, *Controlled growth of tetrapod-branched inorganic nanocrystals*. Nat. Mater., 2(6):382–385, 2003.
- [53] G. Zhou, M. Lü, Z. Xiu, S. Wang, H. Zhang, Y. Zhou, and S. Wang, *Controlled synthesis of high-quality pbs star-shaped dendrites, multipods, truncated nanocubes, and nanocubes and their shape evolution process*. The Journal of Physical Chemistry B, 110(13):6543–6548, 2006.
- [54] N. Zhao and L. Qi, *Low-temperature synthesis of star-shaped pbs nanocrystals in aqueous solutions of mixed cationic/anionic surfactants*. Advanced Materials, 18(3):359–362, 2006.
- [55] L. Rossi, S. Sacanna, W. T. M. Irvine, P. M. Chaikin, D. J. Pine, and A. P. Philipse, *Cubic crystals from cubic colloids*. Soft Matter, 7:4139–4142, 2011.
- [56] N. Kern and D. Frenkel, *Fluid-fluid coexistence in colloidal systems with short-ranged strongly directional attraction*. The Journal of Chemical Physics, 118:9882–9889, 2003.
- [57] F. Romano and F. Sciortino, *Patterning symmetry in the rational design of colloidal crystals*. Nat. Commun., 3:975, 2012.
- [58] F. Romano, E. Sanz, and F. Sciortino, *Role of the range in the fluid-crystal coexistence for a patchy particle model*. The Journal of Physical Chemistry B, 113(46):15133–15136, 2009.
- [59] M. Maldovan and E. L. Thomas, *Diamond-structured photonic crystals*. Nat. Mater., 3(9):593–600, 2004.
- [60] E. C. M. Vermolen, J. H. J. Thijssen, A. Moroz, M. Megens, and A. van Blaaderen, *Comparing photonic band structure calculation methods for diamond and pyrochlore crystals*. Opt. Express, 17(9):6952–6961, 2009.

- [61] Y.-S. Cho, G.-R. Yi, S.-H. Kim, S.-J. Jeon, M. T. Elsesser, H. K. Yu, S.-M. Yang, and D. J. Pine, *Particles with coordinated patches or windows from oil-in-water emulsions*. *Chemistry of Materials*, 19(13):3183–3193, 2007.
- [62] A. B. Pawar, , and I. Kretzschmar, *Patchy particles by glancing angle deposition*. *Langmuir*, 24(2):355–358, 2008.
- [63] M. D. McConnell, M. J. Kraeutler, S. Yang, and R. J. Composto, *Patchy and multiregion janus particles with tunable optical properties*. *Nano Letters*, 10(2):603–609, 2010.
- [64] S. Jiang, Q. Chen, M. Tripathy, E. Luijten, K. S. Schweizer, and S. Granick, *Janus particle synthesis and assembly*. *Advanced Materials*, 22(10):1060–1071, 2010.
- [65] A. B. Pawar and I. Kretzschmar, *Fabrication, assembly, and application of patchy particles*. *Macromolecular Rapid Communications*, 31(2):150–168, 2010.
- [66] Q. Chen, S. C. Bae, and S. Granick, *Directed self-assembly of a colloidal kagome lattice*. *Nature*, 469:381–384, 2011.
- [67] Y. Wang, Y. Wang, D. R. Breed, V. N. Manoharan, L. Feng, A. D. Hollingsworth, M. Weck, and D. J. Pine, *Colloids with valence and specific directional bonding*. *Nature*, 491:51–55, 2012.
- [68] M. R. Jones and C. A. Mirkin, *Materials science: Self-assembly gets new direction*. *Nature*, 491(7422):42–43, 2012.
- [69] L. Feng, R. Dreyfus, R. Sha, N. C. Seeman, and P. M. Chaikin, *Dna patchy particles*. *Advanced Materials*, 25(20):2779–2783, 2013.
- [70] G.-R. Yi, D. J. Pine, and S. Sacanna, *Recent progress on patchy colloids and their self-assembly*. *Journal of Physics: Condensed Matter*, 25(19):193101, 2013.
- [71] Y. Wang, A. D. Hollingsworth, S. K. Yang, S. Patel, D. J. Pine, and M. Weck, *Patchy particle self-assembly via metal coordination*. *Journal of the American Chemical Society*, 135(38):14064–14067, 2013.
- [72] F. Oosawa and S. Asakura, *Surface tension of high-polymer solutions*. *The Journal of Chemical Physics*, 22(7):1255–1255, 1954.
- [73] S. Asakura and F. Oosawa, *Interaction between particles suspended in solutions of macromolecules*. *Journal of Polymer Science*, 33(126):183–192, 1958.
- [74] K. Zhao and T. G. Mason, *Directing colloidal self-assembly through roughness-controlled depletion attractions*. *Phys. Rev. Lett.*, 99:268301, 2007.
- [75] K. Zhao and T. G. Mason, *Suppressing and enhancing depletion attractions between surfaces roughened by asperities*. *Phys. Rev. Lett.*, 101:148301, 2008.
- [76] M. Kamp, M. Hermes, C. M. van Kats, D. J. Kraft, W. K. Kegel, M. Dijkstra, and A. van Blaaderen, *Selective depletion interactions in mixtures of rough and smooth silica spheres*. *Langmuir*, 32(5):1233–1240, 2016.
- [77] S. Badaire, C. Cottin-Bizonne, and A. D. Stroock, *Experimental investigation of selective colloidal interactions controlled by shape, surface roughness, and steric layers*. *Langmuir*, 24(20):11451–11463, 2008.
- [78] D. J. Kraft, R. Ni, F. Smallenburg, M. Hermes, K. Yoon, D. A. Weitz, A. van Blaaderen, J. Groenewold, M. Dijkstra, and W. K. Kegel, *Surface roughness directed self-assembly of patchy particles into colloidal micelles*. *Proceedings of the National Academy of Sciences*, 109(27):10787–10792, 2012.

- [79] J. R. Wolters, G. Avvisati, F. Hagemans, T. Vissers, D. J. Kraft, M. Dijkstra, and W. K. Kegel, *Self-assembly of "mickey mouse" shaped colloids into tube-like structures: experiments and simulations*. *Soft Matter*, 11:1067–1077, 2015.
- [80] M.-P. Valignat, O. Theodoly, J. C. Crocker, W. B. Russel, and P. M. Chaikin, *Reversible self-assembly and directed assembly of dna-linked micrometer-sized colloids*. *Proceedings of the National Academy of Sciences of the United States of America*, 102(12):4225–4229, 2005.
- [81] P. H. Rogers, E. Michel, C. A. Bauer, S. Vanderet, D. Hansen, B. K. Roberts, A. Calvez, J. B. Crews, K. O. Lau, A. Wood, D. J. Pine, and P. V. Schwartz, *Selective, controllable, and reversible aggregation of polystyrene latex microspheres via dna hybridization*. *Langmuir*, 21(12):5562–5569, 2005.
- [82] R. Dreyfus, M. E. Leunissen, R. Sha, A. Tkachenko, N. C. Seeman, D. J. Pine, and P. M. Chaikin, *Aggregation-disaggregation transition of dna-coated colloids: Experiments and theory*. *Phys. Rev. E*, 81:041404, 2010.
- [83] S. Angioletti-Uberti, B. M. Mognetti, and D. Frenkel, *Re-entrant melting as a design principle for dna-coated colloids*. *Nat. Mater.*, 11(6):518–522, 2012.
- [84] S. Angioletti-Uberti, P. Varilly, B. M. Mognetti, and D. Frenkel, *Mobile linkers on dna-coated colloids: Valency without patches*. *Phys. Rev. Lett.*, 113:128303, 2014.
- [85] N. Metropolis and S. Ulam, *The Monte Carlo method*. *J. Amer. Stat. Assoc.*, 44:335, 1949.
- [86] N. Metropolis, A. W. Rosenbluth, M. N. Rosenbluth, A. H. Teller, and E. Teller, *Equation of state calculations by fast computing machines*. *The Journal of Chemical Physics*, 21(6):1087–1092, 1953.
- [87] M. Parrinello and A. Rahman, *Crystal structure and pair potentials: A molecular-dynamics study*. *Phys. Rev. Lett.*, 45:1196–1199, 1980.
- [88] L. Filion, M. Marechal, B. van Oorschot, D. Pelt, F. Smalenburg, and M. Dijkstra, *Efficient method for predicting crystal structures at finite temperature: Variable box shape simulations*. *Phys. Rev. Lett.*, 103:188302, 2009.
- [89] M. P. Allen and D. J. Tildesley. *Computer simulation of liquids*. Oxford university press, 1989.
- [90] D. Frenkel and B. Smit. *Understanding Molecular Simulation: From Algorithms to Applications (Computational Science)*. Academic Press, 2 edition, 2001.
- [91] L. E. Reichl and I. Prigogine. *A modern course in statistical physics*, volume 71. University of Texas press Austin, 1980.
- [92] G. M. Whitesides and B. Grzybowski, *Self-assembly at all scales*. *Science*, 295(5564):2418–2421, 2002.
- [93] M. Lazzari, C. Rodríguez-Abreu, J. Rivas, and M. A. López-Quintela, *Self-assembly: a minimalist route to the fabrication of nanomaterials*. *Journal of nanoscience and nanotechnology*, 6(4):892–905, 2006.
- [94] A. van Blaaderen, *Materials science: Colloids get complex*. *Nature*, 439(7076):545–546, 2006.
- [95] A.-P. Hynninen, J. H. J. Thijssen, E. C. M. Vermolen, M. Dijkstra, and A. van Blaaderen, *Self-assembly route for photonic crystals with a bandgap in the visible region*. *Nat. Mater.*, 6(3):202–205, 2007.
- [96] E. Dickinson, *Use of nanoparticles and microparticles in the formation and stabilization of food emulsions*. *Trends in Food Science & Technology*, 24(1):4 – 12, 2012.

- [97] E. Dickinson and M. E. Leser, editors. *Food Colloids*. Special Publications. The Royal Society of Chemistry, 2007.
- [98] S. Mitragotri and J. Lahann, *Physical approaches to biomaterial design*. Nat. Mater., 8(1):15–23, 2009.
- [99] K.-H. Roh, D. C. Martin, and J. Lahann, *Biphasic janus particles with nanoscale anisotropy*. Nat. Mater., 4(10):759–763, 2005.
- [100] R. Roux, C. Ladavière, A. Montembault, and T. Delair, *Particle assemblies: Toward new tools for regenerative medicine*. Materials Science and Engineering: C, 33(3):997 – 1007, 2013.
- [101] E. Bianchi, R. Blaak, and C. N. Likos, *Patchy colloids: state of the art and perspectives*. Phys. Chem. Chem. Phys., 13:6397–6410, 2011.
- [102] F. Sciortino, A. Giacometti, and G. Pastore, *Phase diagram of janus particles*. Phys. Rev. Lett., 103:237801, 2009.
- [103] L. Hong, A. Cacciuto, E. Luijten, and S. Granick, *Clusters of amphiphilic colloidal spheres*. Langmuir, 24(3):621–625, 2008.
- [104] G. Munaó, Z. Preisler, T. Vissers, F. Smallenburg, and F. Sciortino, *Cluster formation in one-patch colloids: low coverage results*. Soft Matter, 9:2652–2661, 2013.
- [105] T. Vissers, Z. Preisler, F. Smallenburg, M. Dijkstra, and F. Sciortino, *Predicting crystals of janus colloids*. The Journal of Chemical Physics, 138(16):164505, 2013.
- [106] F. Sciortino, E. Bianchi, J. F. Douglas, and P. Tartaglia, *Self-assembly of patchy particles into polymer chains: A parameter-free comparison between wertheim theory and monte carlo simulation*. The Journal of Chemical Physics, 126(19):194903, 2007.
- [107] G. Munaó, D. Costa, F. Sciortino, and C. Caccamo, *Simulation and theory of a model for tetrahedral colloidal particles*. The Journal of Chemical Physics, 134(19):194502, 2011.
- [108] F. Romano, E. Sanz, P. Tartaglia, and F. Sciortino, *Phase diagram of trivalent and pentavalent patchy particles*. Journal of Physics: Condensed Matter, 24(6):064113, 2012.
- [109] Z. Preisler, T. Vissers, F. Smallenburg, G. Munaó, and F. Sciortino, *Phase diagram of one-patch colloids forming tubes and lamellae*. The Journal of Physical Chemistry B, 117(32):9540–9547, 2013.
- [110] Z. Preisler, T. Vissers, G. Munaó, F. Smallenburg, and F. Sciortino, *Equilibrium phases of one-patch colloids with short-range attractions*. Soft Matter, 10:5121–5128, 2014.
- [111] C. Quilliet, C. Zoldesi, C. Riera, A. van Blaaderen, and A. Imhof, *Anisotropic colloids through non-trivial buckling*. The European Physical Journal E, 27(1):13–20, 2008.
- [112] L. Hong, A. Cacciuto, E. Luijten, and S. Granick, *Clusters of charged janus spheres*. Nano Letters, 6(11):2510–2514, 2006.
- [113] A. A. Shah, B. Schultz, K. L. Kohlstedt, S. C. Glotzer, and M. J. Solomon, *Synthesis, assembly, and image analysis of spheroidal patchy particles*. Langmuir, 29(15):4688–4696, 2013.
- [114] Q. Chen, E. Diesel, J. K. Whitmer, S. C. Bae, E. Luijten, and S. Granick, *Triblock colloids for directed self-assembly*. Journal of the American Chemical Society, 133(20):7725–7727, 2011.
- [115] S. Whitelam and S. A. F. Bon, *Self-assembly of amphiphilic peanut-shaped nanoparticles*. The Journal of Chemical Physics, 132(7):074901, 2010.
- [116] G. Munaó, D. Costa, A. Giacometti, C. Caccamo, and F. Sciortino, *Structure and phase behavior of colloidal dumbbells with tunable attractive interactions*. Phys. Chem. Chem. Phys., 15:20590–20599, 2013.

- [117] G. Munaó, P. O'Toole, T. S. Hudson, D. Costa, C. Caccamo, A. Giacometti, and F. Sciortino, *Phase separation and self-assembly of colloidal dimers with tunable attractive strength: from symmetrical square-wells to janus dumbbells*. *Soft Matter*, 10:5269–5279, 2014.
- [118] J. Israelachvili. *Intermolecular and surface forces*. Academic Press, 1992.
- [119] C. Müller-Goymann, *Physicochemical characterization of colloidal drug delivery systems such as reverse micelles, vesicles, liquid crystals and nanoparticles for topical administration*. *European Journal of Pharmaceutics and Biopharmaceutics*, 58(2):343 – 356, 2004.
- [120] G. Cevc, *Lipid vesicles and other colloids as drug carriers on the skin*. *Advanced Drug Delivery Reviews*, 56(5):675 – 711, 2004.
- [121] T. Vohra, I. Kaur, A. Gupta, P. Kumar, and R. Murthy, *Nanosized controlled drug delivery device: Lipid nanoparticle*. *International Journal of Pharmaceutical Sciences Review and Research*, 14(2):148–157, 2012.
- [122] T. Zheng, L.-D. Sun, J.-C. Zhou, W. Feng, C. Zhang, and C.-H. Yan, *Construction of naref4-based binary and bilayer nanocrystal assemblies*. *Chemical Communications*, 49(51):5799–5801, 2013.
- [123] W. L. Miller and A. Cacciuto, *Hierarchical self-assembly of asymmetric amphiphatic spherical colloidal particles*. *Phys. Rev. E*, 80:021404, 2009.
- [124] F. Del Río, E. Ávalos, R. Espíndola, L. F. Rull, G. Jackson, and S. Lago, *Vapour-liquid equilibrium of the square-well fluid of variable range via a hybrid simulation approach*. *Molecular Physics*, 100(15):2531–2546, 2002.
- [125] Q. Meng, Y. Kou, X. Ma, Y. Liang, L. Guo, C. Ni, and K. Liu, *Tunable self-assembled peptide amphiphile nanostructures*. *Langmuir*, 28(11):5017–5022, 2012.
- [126] J. Yang, *Viscoelastic wormlike micelles and their applications*. *Current Opinion in Colloid & Interface Science*, 7:276 – 281, 2002.
- [127] J. Peteiro-Cartelle, M. Rodríguez-Pedreira, F. Zhang, P. Rivera Gil, L. L. del Mercato, and W. J. Parak, *One example on how colloidal nano- and microparticles could contribute to medicine*. *Nanomedicine*, 4:967, 2009.
- [128] S. Sacanna, M. Korpics, K. Rodriguez, L. Colón-Meléndez, S.-H. Kim, D. J. Pine, and G.-R. Yi, *Shaping colloids for self-assembly*. *Nat. Commun.*, 4:1688, 2013.
- [129] G.-R. Yi, D. J. Pine, and S. Sacanna, *Recent progress on patchy colloids and their self-assembly*. *Journal of Physics: Condensed Matter*, 25(19):193101, 2013.
- [130] J. N. Israelachvili, D. J. Mitchell, and B. W. Ninham, *Theory of self-assembly of hydrocarbon amphiphiles into micelles and bilayers*. *Journal of the Chemical Society, Faraday Transactions 2*, 72:1525, 1976.
- [131] V. Percec, W.-D. Cho, G. Ungar, and D. J. P. Yearley, *From Molecular Flat Tapers, Discs, and Cones to Supramolecular Cylinders and Spheres using Fréchet-Type Monodendrons Modified on their Periphery*. *Angewandte Chemie International Edition*, 39(9):1597–1602, 2000.
- [132] L. Hong, A. Cacciuto, E. Luijten, and S. Granick, *Clusters of amphiphilic colloidal spheres*. *Langmuir*, 24(3):621–5, 2008.
- [133] S. Jiang, Q. Chen, M. Tripathy, E. Luijten, K. S. Schweizer, and S. Granick, *Janus particle synthesis and assembly*. *Advanced materials*, 22(10):1060–71, 2010.
- [134] Y. Iwashita and Y. Kimura, *Stable cluster phase of janus particles in two dimensions*. *Soft Matter*, 9(45):10694–10698, 2013.

- [135] Q. Chen, J. Yan, J. Zhang, S. C. Bae, and S. Granick, *Janus and multiblock colloidal particles*. *Langmuir*, 28(38):13555–61, 2012.
- [136] Q. Chen, S. C. Bae, and S. Granick, *Directed self-assembly of a colloidal kagome lattice*. *Nature*, 469(7330):381–384, 2011.
- [137] Y. Wang, Y. Wang, D. R. Breed, V. N. Manoharan, L. Feng, A. D. Hollingsworth, M. Weck, and D. J. Pine, *Colloids with valence and specific directional bonding*. *Nature*, 490(7422):51–55, 2012.
- [138] H. R. Sheu, M. S. El-Aasser, and J. W. Vanderhoff, *Phase separation in polystyrene latex interpenetrating polymer networks*. *Journal of Polymer Science Part A: Polymer Chemistry*, 28(3):629–651, 1990.
- [139] E. B. Mock, H. De Bruyn, B. S. Hawkett, R. G. Gilbert, and C. F. Zukoski, *Synthesis of anisotropic nanoparticles by seeded emulsion polymerization*. *Langmuir*, 22(9):4037–43, 2006.
- [140] J.-W. Kim, R. J. Larsen, and D. A. Weitz, *Synthesis of Nonspherical Colloidal Particles with Anisotropic Properties*. *Journal of the American Chemical Society*, 128(44):14374–14377, 2006.
- [141] J.-G. Park, J. D. Forster, and E. R. Dufresne, *High-yield synthesis of monodisperse dumbbell-shaped polymer nanoparticles*. *Journal of the American Chemical Society*, 132(17):5960–1, 2010.
- [142] D. Nagao, K. Goto, H. Ishii, and M. Konno, *Preparation of asymmetrically nanoparticle-supported, monodisperse composite dumbbells by protruding a smooth polymer bulge from rugged spheres*. *Langmuir*, 27(21):13302–7, 2011.
- [143] J.-W. Kim, D. Lee, H. C. Shum, and D. A. Weitz, *Colloid Surfactants for Emulsion Stabilization*. *Advanced Materials*, 20(17):3239–3243, 2008.
- [144] B. G. P. van Ravensteijn, M. Kamp, A. van Blaaderen, and W. K. Kegel, *General Route toward Chemically Anisotropic Colloids*. *Chemistry of Materials*, 25(21):4348–4353, 2013.
- [145] T. Chen, Z. Zhang, and S. C. Glotzer, *A precise packing sequence for self-assembled convex structures*. *Proceedings of the National Academy of Sciences of the United States of America*, 104(3):717–22, 2007.
- [146] T. Chen, Z. Zhang, and S. C. Glotzer, *Simulation studies of the self-assembly of cone-shaped particles*. *Langmuir*, 23(12):6598–605, 2007.
- [147] G. Munaò, D. Costa, A. Giacometti, C. Caccamo, and F. Sciortino, *Structure and phase behavior of colloidal dumbbells with tunable attractive interactions*. *Physical Chemistry Chemical Physics*, 15(47):20590–20599, 2013.
- [148] G. Munaò, P. O’Toole, T. S. Hudson, D. Costa, C. Caccamo, A. Giacometti, and F. Sciortino, *Phase separation and self-assembly of colloidal dimers with tunable attractive strength: from symmetrical square-wells to janus dumbbells*. *Soft Matter*, 2014.
- [149] F. Sciortino, A. Giacometti, and G. Pastore, *Phase Diagram of Janus Particles*. *Physical Review Letters*, 103(23):1–4, 2009.
- [150] F. Sciortino, A. Giacometti, and G. Pastore, *A numerical study of one-patch colloidal particles: from square-well to Janus*. *Physical Chemistry Chemical Physics*, 12(38):11869–77, 2010.
- [151] T. Vissers, Z. Preisler, F. Smalenburg, M. Dijkstra, and F. Sciortino, *Predicting crystals of janus colloids*. *The Journal of Chemical Physics*, 138(16):164505, 2013.
- [152] G. Munaò, Z. Preisler, T. Vissers, F. Smalenburg, and F. Sciortino, *Cluster formation in one-patch colloids: low coverage results*. *Soft Matter*, 9:2652–2661, 2013.

- [153] Z. Preisler, T. Vissers, F. Smallenburg, G. Munaò, and F. Sciortino, *Phase diagram of one-patch colloids forming tubes and lamellae*. The Journal of Physical Chemistry. B, 117(32):9540–7, 2013.
- [154] T. Vissers, F. Smallenburg, G. Munaò, Z. Preisler, and F. Sciortino, *Cooperative polymerization of one-patch colloids*. The Journal of Chemical Physics, 140(14):144902, 2014.
- [155] D. J. Kraft, R. Ni, F. Smallenburg, M. Hermes, K. Yoon, D. A. Weitz, A. van Blaaderen, J. Groenewold, M. Dijkstra, and W. K. Kegel, *Surface roughness directed self-assembly of patchy particles into colloidal micelles*. Proceedings of the National Academy of Sciences of the United States of America, 109(27):10787–92, 2012.
- [156] J. Liu and E. Luijten, *Rejection-free geometric cluster algorithm for complex fluids*. Phys. Rev. Lett., 92:035504, 2004.
- [157] J. Liu and E. Luijten, *Generalized geometric cluster algorithm for fluid simulation*. Phys. Rev. E, 71:066701, 2005.
- [158] J. D. Bernal, *The bakerian lecture, 1962. the structure of liquids*. Proceedings of the Royal Society of London. Series A, Mathematical and Physical Sciences, pages 299–322, 1964.
- [159] A. H. Boerdijk. Philips Res. Rep., 7, 1952.
- [160] H. S. M. Coxeter. *Regular Complex Polytopes*. University Press, Cambridge, 1974.
- [161] A. I. Campbell, V. J. Anderson, J. S. van Duijneveldt, and P. Bartlett, *Dynamical arrest in attractive colloids: The effect of long-range repulsion*. Physical review letters, 94(20):208301, 2005.
- [162] F. Sciortino, P. Tartaglia, and E. Zaccarelli, *One-dimensional cluster growth and branching gels in colloidal systems with short-range depletion attraction and screened electrostatic repulsion*. The Journal of Physical Chemistry B, 109(46):21942–21953, 2005.
- [163] Q. Chen, J. K. Whitmer, S. Jiang, S. C. Bae, E. Luijten, and S. Granick, *Supracolloidal reaction kinetics of janus spheres*. Science, 331(6014):199–202, 2011.
- [164] S. N. Fejer, D. Chakrabarti, H. Kusumaatmaja, and D. J. Wales, *Design principles for bernal spirals and helices with tunable pitch*. Nanoscale, 2014.
- [165] J. W. Morgan, D. Chakrabarti, N. Dorsaz, and D. J. Wales, *Designing a bernal spiral from patchy colloids*. ACS nano, 7(2):1246–1256, 2013.
- [166] E. J. W. Verwey and J. T. G. Overbeek. *Theory of the Stability of Lyophobic Colloids*. Elsevier, New York, 1948.
- [167] M. F. Hsu, E. R. Dufresne, and D. A. Weitz, *Charge stabilization in nonpolar solvents*. Langmuir, 21(11):4881–7, 2005.
- [168] S. Asakura and F. Oosawa, *Interaction between particles suspended in solutions of macromolecules*. Journal of Polymer Science, 33(126):183–192, 1958.
- [169] A. Vrij, *Polymers at interfaces and the interactions in colloidal dispersions*. Pure Appl. Chem, 48:471–483, 1976.
- [170] H. N. W. Lekkerkerker, W. C.-K. Poon, P. N. Pusey, A. Stroobants, and P. B. Warren, *Phase Behaviour of Colloid + Polymer Mixtures*. Europhysics Letters (EPL), 20(6):559–564, 1992.
- [171] M. G. Noro and D. Frenkel, *Extended corresponding-states behavior for particles with variable range attractions*. The Journal of Chemical Physics, 113(8):2941–2944, 2000.
- [172] G. Foffi and F. Sciortino, *On the possibility of extending the Noro-Frenkel generalized law of correspondent states to nonisotropic patchy interactions*. The Journal of Physical Chemistry B, 111(33):9702–9705, 2007.

- [173] H. A. Kramers, *Brownian motion in a field of force and the diffusion model of chemical reactions*. *Physica*, 7(4):284–304, 1940.
- [174] Q. Chen, J. K. Whitmer, S. Jiang, S. C. Bae, E. Luijten, and S. Granick, *Supracolloidal reaction kinetics of Janus spheres*. *Science*, 331(6014):199–202, 2011.
- [175] M. L. Curri, R. Comparelli, M. Striccoli, and A. Agostiano, *Emerging methods for fabricating functional structures by patterning and assembling engineered nanocrystals*. *Phys. Chem. Chem. Phys.*, 12:11197–11207, 2010.
- [176] D. J. Lunn, J. R. Finnegan, and I. Manners, *Self-assembly of "patchy" nanoparticles: a versatile approach to functional hierarchical materials*. *Chem. Sci.*, 6:3663–3673, 2015.
- [177] P. F. Damasceno, M. Engel, and S. C. Glotzer, *Predictive self-assembly of polyhedra into complex structures*. *Science*, 337(6093):453–457, 2012.
- [178] S. Sacanna, M. Korpics, K. Rodriguez, L. Colón-Meléndez, S.-H. Kim, D. J. Pine, and G.-R. Yi, *Shaping colloids for self-assembly*. *Nat. Commun.*, 4:1688, 2013.
- [179] F. Romano, E. Sanz, and F. Sciortino, *Phase diagram of a tetrahedral patchy particle model for different interaction ranges*. *The Journal of Chemical Physics*, 132(18):184501, 2010.
- [180] X. Mao, Q. Chen, and S. Granick, *Entropy favours open colloidal lattices*. *Nat. Mater.*, 12(3):217–222, 2013.
- [181] F. Lu, K. G. Yager, Y. Zhang, H. Xin, and O. Gang, *Superlattices assembled through shape-induced directional binding*. *Nat. Commun.*, 6:6912, 2015.
- [182] S. Badaire, C. Cottin-Bizonne, J. W. Woody, A. Yang, and A. D. Stroock, *Shape selectivity in the assembly of lithographically designed colloidal particles*. *Journal of the American Chemical Society*, 129(1):40–41, 2007.
- [183] S. Badaire, C. Cottin-Bizonne, and A. D. Stroock, *Experimental investigation of selective colloidal interactions controlled by shape, surface roughness, and steric layers*. *Langmuir*, 24(20):11451–11463, 2008.
- [184] D. J. Kraft, J. Groenewold, and W. K. Kegel, *Colloidal molecules with well-controlled bond angles*. *Soft Matter*, 5:3823–3826, 2009.
- [185] D. J. Kraft, J. Hilhorst, M. A. P. Heinen, M. J. Hoogenraad, B. Luigjes, and W. K. Kegel, *Patchy polymer colloids with tunable anisotropy dimensions*. *The Journal of Physical Chemistry B*, 115(22):7175–7181, 2011.
- [186] P. Virnau and M. Müller, *Calculation of free energy through successive umbrella sampling*. *The Journal of Chemical Physics*, 120(23):10925–10930, 2004.
- [187] A. M. Ferrenberg and R. H. Swendsen, *New monte carlo technique for studying phase transitions*. *Phys. Rev. Lett.*, 61:2635–2638, 1988.
- [188] A. M. Ferrenberg and R. H. Swendsen, *Optimized monte carlo data analysis*. *Phys. Rev. Lett.*, 63:1195–1198, 1989.
- [189] A. Z. Panagiotopoulos, V. Wong, and M. A. Floriano, *Phase equilibria of lattice polymers from histogram reweighting monte carlo simulations*. *Macromolecules*, 31(3):912–918, 1998.
- [190] A. Z. Panagiotopoulos, *Monte carlo methods for phase equilibria of fluids*. *Journal of Physics: Condensed Matter*, 12(3):R25, 2000.
- [191] K. A. Maerzke, L. Gai, P. T. Cummings, and C. McCabe, *Simulating phase equilibria using wang-landau-transition matrix monte carlo*. *Journal of Physics: Conference Series*, 487(1):012002, 2014.

- [192] R. L. C. Vink, J. Horbach, and K. Binder, *Critical phenomena in colloid-polymer mixtures: Interfacial tension, order parameter, susceptibility, and coexistence diameter*. Phys. Rev. E, 71:011401, 2005.
- [193] L. Vega, E. de Miguel, L. F. Rull, G. Jackson, and I. A. McLure, *Phase equilibria and critical behavior of square-well fluids of variable width by gibbs ensemble monte carlo simulation*. The Journal of Chemical Physics, 96(3):2296–2305, 1992.
- [194] D. L. Pagan and J. D. Gunton, *Phase behavior of short-range square-well model*. The Journal of Chemical Physics, 122(18):184515, 2005.
- [195] N. B. Wilding and A. D. Bruce, *Density fluctuations and field mixing in the critical fluid*. Journal of Physics: Condensed Matter, 4(12):3087, 1992.
- [196] A. D. Bruce and N. B. Wilding, *Scaling fields and universality of the liquid-gas critical point*. Phys. Rev. Lett., 68:193–196, 1992.
- [197] N. B. Wilding, *Critical-point and coexistence-curve properties of the Lennard-Jones fluid: A finite-size scaling study*. Physical Review E, 52(1):602–611, 1995.
- [198] N. B. Wilding, *Simulation studies of fluid critical behaviour*. Journal of Physics: Condensed Matter, 9(3):585, 1997.
- [199] R. Kubo and H. Ichimura. *Statistical Mechanics: An Advanced Course with Problems and Solutions*. North-Holland, 1990.
- [200] J. Hansen and I. McDonald. *Theory of Simple Liquids*. Elsevier Science, 2006.
- [201] A. Yethiraj and C. K. Hall, *Square-well diatomics: Bulk equation of state, density profiles near walls, virial coefficients and coexistence properties*. Molecular Physics, 72(3):619–641, 1991.
- [202] G. Munaó, P. O’Toole, T. S. Hudson, D. Costa, C. Caccamo, F. Sciortino, and A. Giacometti, *Cluster formation and phase separation in heteronuclear janus dumbbells*. Journal of Physics: Condensed Matter, 27(23):234101, 2015.
- [203] H. L. Vörtler, K. Schäfer, and W. R. Smith, *Simulation of chemical potentials and phase equilibria in two- and three-dimensional square-well fluids: Finite size effects*. The Journal of Physical Chemistry B, 112(15):4656–4661, 2008.
- [204] R. Evans, U. M. B. Marconi, and P. Tarazona, *Fluids in narrow pores: Adsorption, capillary condensation, and critical points*. The Journal of Chemical Physics, 84(4):2376–2399, 1986.
- [205] M. Schmidt, A. Fortini, and M. Dijkstra, *Capillary condensation of colloid-polymer mixtures confined between parallel plates*. Journal of Physics: Condensed Matter, 15(48):S3411, 2003.
- [206] M. Schmidt, A. Fortini, and M. Dijkstra, *Capillary evaporation in colloid-polymer mixtures selectively confined to a planar slit*. Journal of Physics: Condensed Matter, 16(38):S4159, 2004.
- [207] A. Fortini, P. G. Bolhuis, and M. Dijkstra, *Effect of excluded volume interactions on the interfacial properties of colloid-polymer mixtures*. The Journal of Chemical Physics, 128(2):024904, 2008.
- [208] K. Binder, J. Horbach, R. Vink, and A. De Virgiliis, *Confinement effects on phase behavior of soft matter systems*. Soft Matter, 4:1555–1568, 2008.
- [209] E. Bianchi, J. Largo, P. Tartaglia, E. Zaccarelli, and F. Sciortino, *Phase diagram of patchy colloids: Towards empty liquids*. Phys. Rev. Lett., 97:168301, 2006.
- [210] E. Bianchi, P. Tartaglia, E. La Nave, and F. Sciortino, *Fully solvable equilibrium self-assembly process: Fine-tuning the clusters size and the connectivity in patchy particle systems*. The Journal of Physical Chemistry B, 111(40):11765–11769, 2007.

- [211] F. Sciortino, A. Giacometti, and G. Pastore, *A numerical study of one-patch colloidal particles: from square-well to janus*. *Phys. Chem. Chem. Phys.*, 12:11869–11877, 2010.
- [212] P. Tartaglia and F. Sciortino, *Association of limited valence patchy particles in two dimensions*. *Journal of Physics: Condensed Matter*, 22(10):104108, 2010.
- [213] G. Foffi and F. Sciortino, *On the possibility of extending the Noro-Frenkel generalized law of correspondent states to nonisotropic patchy interactions*. *The Journal of Physical Chemistry B*, 111(33):9702–9705, 2007.
- [214] G. Ganzenmüller, G. Patey, and P. J. Camp, *Vapour-liquid phase transition of dipolar particles*. *Molecular Physics*, 107(4-6):403–413, 2009.
- [215] L. Rovigatti, J. Russo, and F. Sciortino, *No evidence of gas-liquid coexistence in dipolar hard spheres*. *Phys. Rev. Lett.*, 107:237801, 2011.
- [216] S. Dussi, L. Rovigatti, and F. Sciortino, *On the gas-liquid phase separation and the self-assembly of charged soft dumbbells*. *Molecular Physics*, 111(22-23):3608–3617, 2013.
- [217] H. W. Hatch, J. Mittal, and V. K. Shen, *Computational study of trimer self-assembly and fluid phase behavior*. *The Journal of Chemical Physics*, 142(16):164901, 2015.
- [218] V. P. Bykov, *Spontaneous emission from a medium with a band spectrum*. *Soviet Journal of Quantum Electronics*, 4(7):861, 1975.
- [219] E. Yablonovitch, *Inhibited spontaneous emission in solid-state physics and electronics*. *Phys. Rev. Lett.*, 58:2059–2062, 1987.
- [220] E. Yablonovitch, T. J. Gmitter, and K. M. Leung, *Photonic band structure: The face-centered-cubic case employing nonspherical atoms*. *Phys. Rev. Lett.*, 67:2295–2298, 1991.
- [221] E. Yablonovitch, *Photonic band-gap structures*. *J. Opt. Soc. Am. B*, 10(2):283–295, 1993.
- [222] K. M. Ho, C. T. Chan, and C. M. Soukoulis, *Existence of a photonic gap in periodic dielectric structures*. *Phys. Rev. Lett.*, 65:3152–3155, 1990.
- [223] K. Ho, C. Chan, C. Soukoulis, R. Biswas, and M. Sigalas, *Photonic band gaps in three dimensions: New layer-by-layer periodic structures*. *Solid State Communications*, 89(5):413 – 416, 1994.
- [224] H. Sözüer and J. P. Dowling, *Photonic band calculations for woodpile structures*. *Journal of Modern Optics*, 41(2):231–239, 1994.
- [225] H. S. Sözüer and J. W. Haus, *Photonic bands: simple-cubic lattice*. *J. Opt. Soc. Am. B*, 10(2):296–302, 1993.
- [226] H. S. Sözüer, J. W. Haus, and R. Inguva, *Photonic bands: Convergence problems with the plane-wave method*. *Phys. Rev. B*, 45:13962–13972, 1992.
- [227] S. G. Johnson and J. D. Joannopoulos, *Three-dimensionally periodic dielectric layered structure with omnidirectional photonic band gap*. *Applied Physics Letters*, 77(22):3490–3492, 2000.
- [228] S.-Y. Lin, J. Fleming, D. Hetherington, B. Smith, R. Biswas, K. Ho, M. Sigalas, W. Zubrzycki, S. Kurtz, and J. Bur, *A three-dimensional photonic crystal operating at infrared wavelengths*. *Nature*, 394(6690):251–253, 1998.
- [229] J. G. Fleming and S.-Y. Lin, *Three-dimensional photonic crystal with a stop band from 1.35 to 1.95 μ m*. *Opt. Lett.*, 24(1):49–51, 1999.
- [230] J. E. G. J. Wijnhoven and W. L. Vos, *Preparation of photonic crystals made of air spheres in titania*. *Science*, 281(5378):802–804, 1998.

- [231] R. C. Schroden, M. Al-Daous, C. F. Blanford, and A. Stein, *Optical properties of inverse opal photonic crystals*. Chemistry of Materials, 14(8):3305–3315, 2002.
- [232] Y. A. Vlasov, X.-Z. Bo, J. C. Sturm, and D. J. Norris, *On-chip natural assembly of silicon photonic bandgap crystals*. Nature, 414(6861):289–293, 2001.
- [233] M. Qi, E. Lidorikis, P. T. Rakich, S. G. Johnson, J. D. Joannopoulos, E. P. Ippen, and H. I. Smith, *A three-dimensional optical photonic crystal with designed point defects*. Nature, 429(6991):538–542, 2004.
- [234] V. N. Manoharan, M. T. Elseser, and D. J. Pine, *Dense packing and symmetry in small clusters of microspheres*. Science, 301(5632):483–487, 2003.
- [235] C. Young-Sang, Y. Gi-Ra, K. Shin-Hyun, D. J. Pine, and Y. Seung-Man, *Colloidal clusters of microspheres from water-in-oil emulsions*. Chemistry of Materials, 17(20):5006–5013, 2005.
- [236] C. Liddell and C. Summers, *Monodispersed zns dimers, trimers, and tetramers for lower symmetry photonic crystal lattices*. Advanced Materials, 15(20):1715–1719, 2003.
- [237] S.-M. Yang, S.-H. Kim, J.-M. Lim, and G.-R. Yi, *Synthesis and assembly of structured colloidal particles*. J. Mater. Chem., 18:2177–2190, 2008.
- [238] Y. Lu, Y. Yin, and Y. Xia, *Three-dimensional photonic crystals with non-spherical colloids as building blocks*. Advanced Materials, 13(6):415–420, 2001.
- [239] J.-T. Wang, J. Wang, and J.-J. Han, *Fabrication of advanced particles and particle-based materials assisted by droplet-based microfluidics*. Small, 7(13):1728–1754, 2011.
- [240] Y. Yin and Y. Xia, *Self-assembly of monodispersed spherical colloids into complex aggregates with well-defined sizes, shapes, and structures*. Advanced Materials, 13(4):267–271, 2001.
- [241] Y. Xia, Y. Yin, Y. Lu, and J. McLellan, *Template-assisted self-assembly of spherical colloids into complex and controllable structures*. Advanced Functional Materials, 13(12):907–918, 2003.
- [242] L.-Y. Chu, A. Utada, R. Shah, J.-W. Kim, and D. Weitz, *Controllable monodisperse multiple emulsions*. Angewandte Chemie International Edition, 46(47):8970–8974, 2007.
- [243] E. Duguet, A. Desert, A. Perro, and S. Ravaine, *Design and elaboration of colloidal molecules: an overview*. Chem. Soc. Rev., 40:941–960, 2011.
- [244] T. T. Ngo, C. M. Liddell, M. Ghebrebrhan, and J. D. Joannopoulos, *Tetrastack: Colloidal diamond-inspired structure with omnidirectional photonic band gap for low refractive index contrast*. Applied Physics Letters, 88(24):241920, 2006.
- [245] A.-P. Hynninen, J. H. Thijssen, E. C. Vermolen, M. Dijkstra, and A. Van Blaaderen, *Self-assembly route for photonic crystals with a bandgap in the visible region*. Nature Materials, 6(3):202–205, 2007.
- [246] A.-P. Hynninen, L. Filion, and M. Dijkstra, *Stability of LS and LS₂ crystal structures in binary mixtures of hard and charged spheres*. The Journal of Chemical Physics, 131(6):064902, 2009.
- [247] J. H. Zhu, C. T. Liu, L. M. Pike, and P. K. Liaw, *A thermodynamic interpretation of the size-ratio limits for laves phase formation*. Metallurgical and Materials Transactions A, 30(5):1449–1452, 1999.
- [248] A. R. Edwards, *The lattice dimensions of the AB₂ laves phases*. Metallurgical Transactions, 3(6):1365–1372, 1972.
- [249] M. Kowalik, K. Tretiakov, and K. Wojciechowski, *On relative stability of selected hard tetramer solids*. Computational Methods in Science and Technology, 16(2):141–146, 2010.

- [250] D. Frenkel and A. J. C. Ladd, *New monte carlo method to compute the free energy of arbitrary solids. application to the fcc and hcp phases of hard spheres*. The Journal of Chemical Physics, 81(7):3188–3193, 1984.
- [251] M. Marechal and M. Dijkstra, *Stability of orientationally disordered crystal structures of colloidal hard dumbbells*. Phys. Rev. E, 77:061405, 2008.
- [252] C. Vega, E. Sanz, J. L. F. Abascal, and E. G. Noya, *Determination of phase diagrams via computer simulation: methodology and applications to water, electrolytes and proteins*. Journal of Physics: Condensed Matter, 20(15):153101, 2008.
- [253] D. de las Heras and M. Schmidt, *Sedimentation stacking diagram of binary colloidal mixtures and bulk phases in the plane of chemical potentials*. Journal of Physics: Condensed Matter, 27(19):194115, 2015.
- [254] J. C. Williams, *The segregation of particulate materials. a review*. Powder technology, 15(2):245–251, 1976.
- [255] A. Rosato, K. J. Strandburg, F. Prinz, and R. H. Swendsen, *Why the brazil nuts are on top: Size segregation of particulate matter by shaking*. Phys. Rev. Lett., 58:1038–1040, Mar 1987.
- [256] A. Esztermann and H. Löwen, *Colloidal brazil-nut effect in sediments of binary charged suspensions*. Europhys. Lett., 68(1):120, 2004.
- [257] M. N. van der Linden. *Long-range repulsive charged colloids in and out of equilibrium*. PhD thesis, Utrecht University, April 2013.
- [258] D. de las Heras, N. Doshi, T. Cosgrove, J. Phipps, D. I. Gittins, J. S. van Duijneveldt, and M. Schmidt, *Floating nematic phase in colloidal platelet-sphere mixtures*. Scientific Reports, 2:789, 2012.
- [259] W. H. Evers, B. D. Nijs, L. Filion, S. Castillo, M. Dijkstra, and D. Vanmaekelbergh, *Entropy-driven formation of binary semiconductor-nanocrystal superlattices*. Nano Letters, 10(10):4235–4241, 2010.
- [260] C. B. Murray, C. R. Kagan, and M. G. Bawendi, *Self-organization of cdse nanocrystallites into three-dimensional quantum dot superlattices*. Science, 270(5240):1335–1338, 1995.
- [261] A. D. Dinsmore, J. C. Crocker, and A. G. Yodh, *Self-assembly of colloidal crystals*. Current Opinion in Colloid & Interface Science, 3(1):5 – 11, 1998.
- [262] S. Yoshimura and S. Hachisu. *Order formation in binary mixtures of monodisperse latices*, pages 59–70. Steinkopff, Darmstadt, 1983.
- [263] J. J. Urban, D. V. Talapin, E. V. Shevchenko, C. R. Kagan, and C. B. Murray, *Synergism in binary nanocrystal superlattices leads to enhanced p-type conductivity in self-assembled PbTe/Ag₂Te thin films*. Nat. Mater., 6(2):115–121, 2007.
- [264] E. V. Shevchenko, D. V. Talapin, N. A. Kotov, S. O’Brien, and C. B. Murray, *Structural diversity in binary nanoparticle superlattices*. Nature, 439(7072):55–59, 2006.
- [265] A. L. Rogach, *Binary superlattices of nanoparticles: Self-assembly leads to "Metamaterials"*. Angewandte Chemie International Edition, 43(2):148–149, 2004.
- [266] J. R. Heath, *Materials science: Synergy in a superlattice*. Nature, 445(7127):492–493, 2007.
- [267] B. Liu, T. H. Besseling, M. Hermes, A. F. Demirörs, A. Imhof, and A. van Blaaderen, *Switching plastic crystals of colloidal rods with electric fields*. Nature Communications, 5:3092, 2014.
- [268] A. Fortini, M. Dijkstra, M. Schmidt, and P. P. F. Wessels, *Wall-fluid and liquid-gas interfaces of model colloid-polymer mixtures by simulation and theory*. Phys. Rev. E, 71:051403, 2005.

-
- [269] M. Marechal and M. Dijkstra, *Phase behavior and structure of colloidal bowl-shaped particles: Simulations*. Phys. Rev. E, 82:031405, 2010.
- [270] A. P. Gantapara, J. de Graaf, R. van Roij, and M. Dijkstra, *Phase diagram and structural diversity of a family of truncated cubes: Degenerate close-packed structures and vacancy-rich states*. Phys. Rev. Lett., 111:015501, 2013.
- [271] N. F. Carnahan and K. E. Starling, *Equation of state for nonattracting rigid spheres*. The Journal of Chemical Physics, 51(2):635–636, 1969.
- [272] R. J. Speedy, *Pressure and entropy of hard-sphere crystals*. Journal of Physics: Condensed Matter, 10(20):4387, 1998.

Summary

This thesis work deals with the phase behaviour of colloidal particles in suspension. The typical size of a colloidal particle ranges from nanometers to micrometers (about five hundred times smaller than the thickness of a human hair). Such tiny particles display Brownian motion due to collisions with the solvent molecules, and this enables them to explore all possible system configurations and to choose the structure which is most convenient in the thermodynamic sense – a process which is referred to as *self-assembly*. Colloidal particles can form gas, liquid and crystal phases just as atoms can, but on much longer length and time scales. This allows for insights at the single particle level on the stability of these phases and the transitions between them, i.e. on the system *phase behaviour*. Moreover, due to the intrinsic size of the colloidal particles, the assembled structures interact with light in the visible region of the spectrum, giving rise to applications in a plethora of fields such as optical devices, energy storage, information encryption, and bioengineering.

The self-assembly of specific structures can be targeted by varying the shape of the particles, and the particle-particle interaction. If we think of the colloidal particles as primary building blocks, then the self-assembly of different structures can be seen as playing with LEGO at a microscopic level. For instance, hard spheres (colloidal billiard balls) self-assemble into a face-centered-cubic (FCC) crystal for high enough density, while hard rods display liquid-crystalline phases with different degrees of order. Of course, we do not know beforehand which shape and pair-interaction will result in the desired structure, hence we need to study the different cases by means of a predicting tool. The tool of choice for our investigation is computer simulations, and the chapters of this thesis present particular examples of colloids with different shape and interparticle potential, and the structures that can be self-assembled from them.

In part 1 of this thesis, we deal with particles with attractive spots at prescribed locations, also known as "patchy" particles. This kind of particles can be advantageous to target open crystalline structures, or to induce the formation of aggregates of finite size. In **chapter 2**, we study the self-assembly of dumbbell-shaped particles with one attractive bead. We show that, upon varying the geometry of the dumbbell, clusters of different shape and size can be formed. Specifically, we observe the spontaneous formation of spherical and cylindrical micelles, vesicles, and bilayers in a regime of low packing fraction. The particles assemble themselves from the gaseous phase, and rearrange until they form clusters of defined shape. Especially vesicles and bilayers are of interest here, as they could be used as model systems to investigate, at the colloidal scale, processes like drug encapsulation/delivery or the behaviour of biological membranes. In **chapter 3**, we study the self-assembly of triangular trimers, with two repulsive and one attractive bead – also known as "Mickey Mouse" (MM) particles due to their peculiar shape. We find that these particles display a gas, a cluster and a tube phase upon decreasing the temperature of the system. The tubes are stabilised against further aggregation by the repulsive beads of the trimers, which point radially outwards of the tube. We compare the results obtained by our simple simulation model to the experiments performed by J. Wolters under Prof. W. Kegel at Utrecht University [79], and find good agreement in the displayed phase behaviour. In **chapter 4**, we ask ourselves how the self-assembly scenario of the MM particles depicted in chapter 3 is related to the well-known phenomenon of gas-liquid phase separation of attractive

spheres. We address this question by connecting the spheres to the MM particles via a series of intermediate models where we first grow outer beads on the spheres and then reduce the interaction range to the one studied in chapter 3. We find that the binodal line and its critical point shifts to lower temperatures upon growing the outer beads, which reduces the particles' valence, and that shrinking the interaction range triggers the formation of the previously observed tube-like structures.

In part 2 of this thesis, we deal with binary mixtures of hard particles, whose phase behaviour is completely entropy driven and depends on the applied pressure and the chosen composition. These mixtures can be employed to fabricate specific binary colloidal crystals in the high density/high pressure regime. In **chapter 5**, we study the bulk phase behaviour of a mixture of hard spheres and hard tetrahedral clusters of beads (tetramers). We show via free-energy calculations that a particularly useful binary crystal structure, the MgCu_2 Laves phase, can be assembled from the fluid mixture. This structure is very useful as it can be turned into a diamond crystal, which is a nanomaterial displaying a complete photonic bandgap in the visible region, and that can serve as wave guide with unmatched properties. We predict the formation of this crystal in a particular region of the phase diagram, hence giving directions towards its experimental realisation. Furthermore, we also address the sedimentation behaviour of the mixture, by theoretically calculating all the possible stacking sequences that can be observed when performing a sedimentation experiment, where the mixture is allowed to slowly sediment in a vial. In **chapter 6**, we investigate the stability of an AB_{13} crystal, as well as the presence of plastic crystalline phases, in a mixture of hard spheres and hard icosahedral clusters. The AB_{13} crystal phase is found in mixtures of spherical nanoparticles, but can be also packed with a mixture of icosahedral clusters and spheres. However, when linking beads together in an icosahedron, plastic crystalline phases may emerge, due to the orientational freedom of the icosahedra. A plastic crystal is a structure with long range positional order and short range orientational order. We study the phase diagram of a mixture of hard spheres and hard icosahedral clusters of spheres, and find that a plastic crystalline phase of icosahedra is in phase coexistence with the fluid mixture, as well as with the AB_{13} crystal. The AB_{13} crystal is also, in turn, in coexistence with the fluid mixture in a different region of the phase diagram. This study gives directions to guide the experimental investigation, at the colloidal level, of the formation mechanism of the plastic crystalline phase, and its stability with respect to the binary AB_{13} crystal phase.

This thesis represents yet another step into understanding how complex shape and interaction influence the self-assembly of colloidal particles, and how nanomaterials with novel properties can be fabricated from them.

Samenvatting

Dit proefschrift behandelt het fasegedrag van colloïdale deeltjes in suspensie. De typische grootte van een colloïdaal deeltje bevindt zich tussen de nano- en micrometers (ongeveer 500 keer kleiner dan de dikte van een menselijke haar). Zulke kleine deeltjes ondergaan Brownse beweging door de botsingen met de moleculen van de vloeistof. Deze beweging maakt dat de deeltjes alle systeemconfiguraties vinden en dat ze uitkomen op de beste configuratie in thermodynamische zin – een proces dat bekend staat als *zelforganisatie*. Colloïdale deeltjes kunnen gas-, vloeistof- en kristalfases vormen, net als atomen, maar dan op veel grotere lengte- en tijdschaal. Dit biedt inzicht in de stabiliteit van deze fasen en de overgangen tussen deze fasen (d.w.z. het *fasegedrag* van het systeem) op het niveau van een enkel deeltje. Bovendien maakt de intrinsieke grootte van de deeltjes dat de zelfgeorganiseerde structuren interacteren met zichtbaar licht. Hierdoor zijn tal van toepassingen mogelijk in verschillende gebieden, zoals optische apparaten, energieopslag, informatieversleuteling, biotechniek.

De zelforganisatie van specifieke structuren kunnen worden gestuurd door de vorm van de deeltjes en de interactie tussen de deeltjes te variëren. Als we de deeltjes beschouwen als primaire bouwstenen, dan kan de zelforganisatie van de verschillende structuren worden gezien als spelen met LEGO op een microscopische schaal. Bijvoorbeeld, harde bollen (colloïdale biljartballen) zelf organiseren zich in kubisch vlakgecentreerde kristallen bij een voldoende hoge dichtheid, terwijl harde staven vloeibare kristallijne fasen met verschillende maten van orde ondergaan. Natuurlijk weten wij niet van tevoren welke vorm en deeltjesinteracties zal leiden tot de gewenste structuur, daarom moeten wij de verschillende gevallen bestuderen door middel van een voorspellingshulpmiddel. Het middel bij uitstek voor ons onderzoek is computersimulaties, en de hoofdstukken in deze thesis beschrijven specifieke voorbeelden van colloïden met verschillende vormen en interacties, en de structuren waarin deze zelforganiseren.

In deel 1 van deze thesis, behandelen we deeltjes met voorgeschreven attractieve vlekken, ook wel bekend als “patchy” deeltjes. Deze deeltjes zijn een goede kandidaat voor het vormen van open kristallijne structuren, of het vormen van aggregaten met een eindige grootte. In **hoofdstuk 2**, bestuderen wij de zelforganisatie van haltervormige deeltjes met één attractief bol. We laten zien dat wanneer de geometrie van de haltervormige deeltjes wordt veranderd, aggregaten met verschillende vormen en groottes kunnen worden gevormd. In het bijzonder observeren wij de spontane vorming van sferische en cilindrische micellen, vesikels en dubbellen bij lage dichtheid. De deeltjes organiseren zichzelf vanuit de gasfase, en herschikken zich tot zij een aggregaat vormen met een bepaalde vorm. Vooral vesikels en dubbellen zijn relevant, aangezien deze als modelsystemen op colloïdale schaal kunnen dienen voor onderzoek naar processen als geneesmiddelinkapseling/-aflevering of het gedrag van biologische membranen. In **hoofdstuk 3**, bestuderen we de zelforganisatie van driehoekige trimeren met twee repulsieve en een attractieve bol – ook wel bekend als “Mickey Mouse” (MM) deeltjes, vanwege hun eigenaardige vorm. Wij vinden dat deze deeltjes een gas-, aggregaat- en buisfase vormen bij afnemende temperatuur van het systeem. Verdere aggregatie na de buisfase wordt voorkomen door de repulsieve kralen van de trimeren, die in radiale richting naar buiten wijzen. Wij vergelijken de uit ons simpel model verkregen resultaten met de experimenten uitgevoerd door J. Wolters onder supervisie van Prof. W. Kegel aan de Universiteit Utrecht [79], en vinden

goede overeenkomst in het gevonden fasegedrag. In **hoofdstuk 4**, vragen wij ons af hoe de zelforganisatie van de MM-deeltjes in hoofdstuk 3 zich verhoudt tot het welbekende fenomeen van de gas-vloeistof fasescheiding van attractieve bollen. Wij stellen deze vraag door de bollen aan de MM-deeltjes te koppelen via een serie van tussenliggende modellen, waar we eerst bollen groeien aan de buitenzijdes en vervolgens het bereik van de interacties verminderen tot die van de interactie in hoofdstuk 3. Wij vinden dat de binodaal en het bijbehorende kritische punt naar lagere temperaturen verschuift bij het vergroten van de buitenste bollen, hetgeen de valentie van de deeltjes verkleint, en dat het verkleinen van het bereik van de interacties de formatie van de eerder waargenomen buisachtige structuren veroorzaakt.

In deel 2 van dit proefschrift behandelen we binaire mengsels van harde deeltjes, waarvan het fasegedrag volledig bepaald wordt door de entropie. Het fasegedrag hangt af van de uitgeoefende druk en de gekozen compositie. Deze mengsels kunnen worden gebruikt om specifieke binaire colloïdale kristallen te maken in het hoge dichtheid/hoge druk regime. In **hoofdstuk 5**, bestuderen we het bulk fasegedrag van een mengsel van harde bollen en harde tetraëdrische clusters van bollen (tetrameren). Wij tonen aan door middel van vrije-energieberekeningen, dat een bijzonder bruikbaar binair kristalstructuur, de $MgCu_2$ Laves fase, kan worden gevormd uit het vloeistofmengsel. Deze structuur is erg van belang, aangezien het in een diamantstructuur veranderd kan worden, hetgeen een nanomateriaal is met een complete verboden zone in het zichtbare regime en kan dienen als een golfgeleider met ongeëvenaarde eigenschappen. Wij voorspellen de vorming van dit kristal in een bepaalde regio van het fasediagram, waarmee wij de weg wijzen voor de experimentele realisatie van deze structuur. Voorts behandelen we ook het bezinkgedrag van het mengsel door middel van berekeningen van alle mogelijke stapelsequenties die kunnen worden waargenomen wanneer een sedimentatieexperiment wordt uitgevoerd, waarbij een mengsel langzaam bezinkt in een buisje. In **hoofdstuk 6**, onderzoeken we zowel de stabiliteit van een AB_{13} kristal, als de aanwezigheid van plastische kristalfasen, in een mengsel van icoesaëdrische clusters en harde bollen. Wanneer de bollen aan elkaar gekoppeld worden in een icoesaëder, kan een plastisch-kristalfase ontstaan, vanwege de vrijheid in oriëntatie van de icoesaëder. Een plastisch kristal is een structuur met positionele orde over lange afstand en een oriëntationele orde over korte afstand. Wij onderzoeken het fasediagram van een mengsel van harde bollen en harde icoesaëdrische clusters van bollen, en vinden dat een plastisch-kristalfase van icoesaëder bestaat, naast zowel een vloeistoffase als een AB_{13} kristal. Het AB_{13} kristal, op zijn beurt, bestaat ook naast de vloeistoffase in een andere regio in het fasediagram. Dit onderzoek geeft aanwijzingen voor verdere experimentele onderzoek op colloïdaal niveau naar het vormingsmechanisme van de plastisch-kristalfase en de stabiliteit ervan in vergelijking tot de binaire AB_{13} kristalfase.

Ons onderzoek vormt een stap naar een groter begrip van de invloed van complexe vormen en interacties in de zelforganisatie van colloïdale deeltjes, wat kan leiden tot het produceren van nanomaterialen met nieuwe eigenschappen.

Acknowledgements

The journey towards my PhD started long ago, beginning in Munich, Bavaria and ending here in Utrecht. Overall, it was to me more of a life experience than I could ever have imagined, perhaps the most important journey I have made so far. This doesn't mean that it was always fun, or always pleasant, but it does mean that whatever I learned from it is going to accompany me in the future. Surely, the best part is that I wasn't alone during this journey: I got lucky and shared the road with many people who brought colours onto an otherwise black and white sketch, and who made that sketch a painting.

First and foremost I want to thank my supervisor Marjolein Dijkstra. You helped me prove to myself that I could, in fact, do research, by offering me a second chance at graduation. This really means a lot to me, probably more than I can express. Besides your knowledge and your guidance, I thank you for leaving me the necessary freedom in my scientific research, but also for always having a backup plan in case things didn't turn out well. Thank you for also caring about the atmosphere in the group, which makes for a very nice work environment.

Furthermore, I would like to thank the staff of our Soft Condensed Matter group: Alfons van Blaaderen, Arnout Imhof, René van Roij, Laura Filion, Marijn van Huis, Krassimir Velikov and Patrick Baesjou. Thank you for all the valuable comments and suggestions you gave me during these years, which enormously improved both my research and my results. Thank you Alfons, even for asking simple but perhaps overlooked questions. I also want to thank Laura for the long time spent with me discussing about the free-energy calculations. Many thanks to René for his comments, which helped to broaden the scope of the research. The technical staff of our group, Marion, Thea, Peter, Chris, Judith, and Relinde, is also thanked for all the help with the logistics.

I gratefully thank Joost Wolters, Joanne Verweij, and Prof. Willem Kegel from the Physical Chemistry group of the van't Hoff Laboratory at Utrecht University for the fruitful collaborations on the Mickey Mouse particles, on the encapsulation of microspheres by dumbbells, and for stimulating discussions. I want to thank Teun Vissers for his help with setting up the simulation codes for both the project on the patchy dumbbells and the one on the MM particles, as well as for the fun pub nights when he visited me in Utrecht.

Next, it is time to start calling out single people to thank. I begin this long list with my current office mates, Harini Pattabhiraman and Nick Tasios. Of course, everybody thinks they have the coolest office, while the three of us actually did. Thank you for always keeping the finest of the attitudes and a nice atmosphere. Dear Nick, thank you for the times you helped me coding, and for those horrible looking t-shirts which eventually (and finally!) gave the way to proper shirts. Thanks also for showing me that, no matter how efficient I made my code, you could always make one 23.8x faster. Dear Harini, thank you for your caring personality and your enormous patience that allowed you to put up with my stupid jokes for almost 4 years. I also enjoyed collaborating with you on small as well as big projects. Thank you also for being so organised and for making me be on time at most of the meetings. Moreover, thank you for keeping the plants in our office (almost) alive, and for not snapping at me not. My previous

office mates, Kristina Milinković and Marjolein van der Linden are also acknowledged for introducing me to the group when I first joined.

I sincerely thank all of the current and former colleagues of the SCM group I have crossed paths with, for being available to one another and for making the atmosphere in group really nice. Whether we had a scientific discussion or a non scientific one, our shared goal was always to learn and have fun together. For this, thank you very much to Henriëtte, Jessi, Wessel, Nina, Pepijn, Rik, Rama, Fabian, Douglas, Vassilis, Bart, Marlous, Johan, Jissy, Thijs, Tian-Song, Bas, Bo, Rao, Murphy, Somil, Berend, Ravi, Frankje, Anna, Ernest, Vats, Da, Siddharth, Giulia, Tonnishtha, Chris, Wiebke, Marjolein, Kristina, Simone (Dussi), Bas, Sina, Naveed, Bing, Xiaobin, Ajoy, Carmine, Massimiliano, Robin, Stijn, Anjan, John, Zdenek, Federico, Yang, Sela, Simone (Belli), Thomas, Andreas, Bram, Mathijs, Jeffrey, Giuseppe, Tara.

Thank you all for the moments we shared together such as, the DO! Days, the Han-sur-Lesse schools, the Debye Schools, the Varenna summer school, the Physics@FOM Veldhoven events, the scientific training courses, and all of the conferences we attended in different parts of the world. Thanks also for the more informal moments like the group outings, the evenings at the pub, the beers with peers evenings, the social get together events, and the sport days. A special thanks goes to John, Simone, Chris, Giulia, and Wessel who, at different times, made their houses available for formal and informal dinners. Thanks to all people I bothered with my stupid pranks, who afterwards still greeted me in the corridors. Thanks to Chris for polishing the back matter of this thesis, and to Ernest, Jessi, and Wessel for translating my English summary into Dutch.

A minor part of my time here in Utrecht was dedicated to teach other people the foosball basics and some tricks, and to lead an expedition to buy a new table for the group. I can proudly say that both projects have been successfully accomplished and that there will be a legacy to the current foosball crew. However, a special thanks goes to the A-league (Zio Simone, Ernest[o], Wessel, myself), and its bench (Nicola, Vasilakis) for providing a next-level challenge. Thanks Vassilis for leaving the table infuriated after losing a match, it always cracked me up. Thanks to Naveed for being the only one keeping up with my trash talk during the game, to (tiny) Toni for only shooting the ball off target, to Wiebke for not giving up on a single ball, and to Giulia who is simply the queen of the table. The other people (aka noobs) are also acknowledged for making me experience what it means to crawl under the table.

Because the SCM is a rather big group, it is easy to find oneself involved in smaller sub-groups of people who share common interests. I would like to thank the group “Gossip girls” who provided me with plenty of information about the latest facts within the SCM group (of course I can’t say who is part of this gang). The squash crew, Wiebke, Chris, Simone, Pepijn, is also acknowledged. I thank Annalisa and the rest of the salsa people for giving me the energy to start a new cycle. Writing a PhD thesis is clearly no piece of cake, and I found that the pain caused by it can be relieved by sharing the stress of this particular period with somebody else who’s doing the same thing and is in a similar state of mind. Therefore, thanks to Henriëtte for being my first thesis buddy and to Wiebke for being my second one: team thesis 1 & 2, the mission is accomplished. Dear Somil-Somil, thank you for trying to burn down the whole institute while warming up your croissant with our microwave, it was just unforgettable. Dear Toni, thank you for the amount of unfunny jokes you cracked during these years, for unconsciously writing on the wall instead of the whiteboard, and for that legendary facebook post

named “what girls look for in a guy”. Dear Giulia, thank you first of all for being so direct. I remember that during your first week you told to my face in one sitting that I was fat, bald, and short! It didn’t really sound like the beginning of a friendship. However, since then we have built a lot of trust and affection between us, for which I thank you. Dear ladies of OL016, thank you also for the long walks in the botanical garden, which helped me clear my mind during my difficult times.

I am also grateful for the time I spent in Munich, because I was lucky enough to find there amazing people and true friends. Jonny and Bhaskar, thank you for welcoming me at Sigrid’s house, for your patience with my broken English, and for all the fun we had together – whether it was just playing basketball at the institute, or going sledging in the mountains. Alessia, thank you very much for becoming an essential part of this group of friends. I also want to thank all the people with whom I shared the X6 building, the X6ers: Tobi, Jin, Philip, Thomas, Pintu, Tiangfang, Dong, Leila, thank you all for the nice atmosphere, the game nights, the barbecues and the hours tasting hotpots at the Chinese restaurant. Leila, you are a wonderful person and I really admire you. Thank you for all the encouragement you gave me in my difficult times and for the part of road that we shared. Surely, this thesis would not have been possible without your support.

Of course, I could never forget to mention my best friend and paranymp Marianna. Having you here during my graduation day really means a lot to me. Thank you for always being there for me and also for your kind words about me in your own PhD thesis. Thanks to Maddalena, Martina and Marina for always welcoming me back in Naples, and for sharing the latest news about themselves and others, thank you M.M.M.M.!

A big thank you to my childhood friends, Federico, Raffaele, Marco, Giuseppe. Thank you for the fun we had so far and the one we’ll have, for all the game nights, for the countless hours spent swearing while playing DotA. Thank you because you know when to ask and when not to ask things, and because you’re a second family to me.

So it comes to the real family, to my mother Rosa, to my sister and paranymp Livia and to my brother-in-law Nicola. Thank you for all the love and support you gave me during these years. Thank you because we were close even if far apart. Finally, thank you for the warm welcomes even when things were not going smoothly for you. Vi voglio bene! The rest of my family is simply too big to be acknowledged on a per person basis. Let me just say that I thank all of them for the continuous support, grazie mille del vostro affetto!

Dear Giulia, getting to know you over the last year and a half was a journey within a journey. It brought me lots of harsh jokes and happy moments, most of all it delighted me throughout. I love the way you are strong and direct, but at the same time generous and sweet, always with a positive attitude. It felt just natural when our tender friendship suddenly evolved into a relationship which we are shaping everyday more and more. It may be too soon, but I can’t help thinking about the future with you, because I (get) completely lost when I look into your eyes – “... e si chest nunn’e’ ammore, ma nuje che campamme a ffa’...”. Dear Giulia, thank you very much for the time we spent together, and for the time which is ahead of us.

List of Publications

This thesis is based on the following publications:

- G. Avvisati, T. Vissers, and M. Dijkstra, *Self-assembly of patchy colloidal dumbbells*, The Journal of Chemical Physics **142**, 084905 (2015) (Chapter 2).
- J. R. Wolters, G. Avvisati, F. Hagemans, T. Vissers, D. J. Kraft, M. Dijkstra, and W. K. Kegel, *Self-assembly of "Mickey Mouse" shaped colloids into tube-like structures: experiments and simulations*, Soft Matter **11**, 1067 (2015) (Chapter 3).
- G. Avvisati and M. Dijkstra, *Phase separation and self-assembly in a fluid of Mickey Mouse particles*, Soft Matter **11**, 8432 (2015) (Chapter 4).
- G. Avvisati, T. Dasgupta, and M. Dijkstra, *Fabrication of colloidal Laves phases via hard tetramers and hard spheres: bulk phase diagram and sedimentation behaviour*, manuscript submitted (Chapter 5).
- G. Avvisati and M. Dijkstra, *Phase behaviour of a binary mixture of colloidal hard spheres and hard icosahedral clusters*, manuscript in preparation (Chapter 6).

Other publications by the author:

- J. R. Wolters, J. E. Verweij, G. Avvisati, M. Dijkstra, and W. K. Kegel, *Depletion induced encapsulation by dumbbell-shaped patchy colloids stabilize microspheres against aggregation*, manuscript submitted.
- H. Pattabhiraman, G. Avvisati and M. Dijkstra, *Stable pyrochlore and hexagonal columnar phases formed in a three-dimensional core-corona system*, manuscript in preparation.

Oral and Poster Presentations

The contents of this thesis was presented at the following:

- ISMC 2013, Rome (IT)
- Physics@FOM 2014, Veldhoven (NL)
- 9th Liquid Matter Conference 2014, Lisbon (PT)
- SCM 15th Anniversary Symposium, 2014, Utrecht (NL)
- Physics@FOM 2015, Veldhoven (NL)
- 18th Dutch Soft Matter Meeting, 2015, Eindhoven (NL)
- Physics@FOM 2016, Veldhoven (NL)
- ECIS 2106, Rome (IT)
- Physics@FOM 2017, Veldhoven (NL)

